PASSIVE SYNTHETIC APERTURE RADAR IMAGING OF GROUND MOVING TARGETS

By

Steven Wacks

A Thesis Submitted to the Graduate

Faculty of Rensselaer Polytechnic Institute

in Partial Fulfillment of the

Requirements for the Degree of

DOCTOR OF PHILOSOPHY

Major Subject: ELECTRICAL ENGINEERING

Approved by the
Examining Committee:

Birsen Yazici, Thesis Adviser

Kim Boyer, Member

Kenneth Vastola, Member

David Isaacson, Member

Rensselaer Polytechnic Institute
Troy, New York

April 2014
(For Graduation May 2014)

CONTENTS

LIST OF TABLES

LIST OF FIGURES

ABSTRACT

Synthetic aperture radar (SAR) is an imaging technique that uses antenna motion and spatial diversity to coherently combine received waveforms and form images of a scene of interest. This thesis focuses on the SAR problem of passive imaging of moving targets. A passive radar imaging system uses small, mobile receivers that do not radiate any energy. The received signals are obtained from the scattered waves due to illuminating sources of opportunity such as commercial television, radio, and cell phone towers. A system of passive receivers results in significant cost and manufacturing advantages. Additionally, since the passive radar systems do not radiate any energy, they offer stealth benefits.

The first part of this thesis considers the passive synthetic aperture moving target imaging problem using relatively wideband RF sources of opportunity such as DVB-T and WiMax signals. No knowledge of the transmitter locations or waveforms is assumed, so a correlation-based technique is used to backproject the data based on time difference of arrival between pairs of receivers. Velocity estimation is performed by forming images based on a range of hypothesized velocities, and analyzing the degree of focus of each image. We show that images with the correct hypothesized velocities will yield focused reconstructions of the corresponding moving target. In addition, a detailed performance analysis is developed for this method.

The second part of this thesis addresses the case of ultra-narrowband transmitters of opportunity. These signals of opportunity are common, but they do not possess high enough bandwidth to provide the range information to use with conventional SAR methods. Instead, an approach called Doppler-SAR is used, where high resolution position images are formed by using the high Doppler resolution information in the ultra-narrowband waveforms. We first develop an analogous method to the case of unknown transmitter parameters by using correlation to backproject the frequency difference of arrival between pairs of received signals. Next, a novel technique to combine the Doppler imaging approach with the displaced phase center antenna approach is developed. Two channels are used to receive signals from a scene, and their Doppler shifts are compared to remove stationary clutter. Finally, the along-track interferometry clutter suppression method is also combined with Doppler SAR, and the theoretical results of the Doppler case are compared to the well known wideband case.

CHAPTER 1
Introduction

1.1 Motivation

Synthetic aperture radar (SAR) is a type of radar that attempts to form images of the Earth's surface by coherently combining the reflected radio waves at different antenna locations. This technology has many important applications in both civil and defense areas. For example, SAR imaging can be used to monitor the status of dams and levees from space-borne satellites, or airborne antennas can be flown over a scene of interest to form an image of an important location in hostile territory. Since SAR uses radio waves and not optics, these tasks can be performed at places and times where ordinary optical imaging could not, such as at night or in inclement weather.

Passive radar systems do not use their own active transmitters, but instead, they rely on external sources of opportunity present in the surrounding environment. The received signals are obtained from the scattered waves transmitted by either cooperative or non-cooperative illuminating sources of opportunity. Imaging methods that use cooperative sources of opportunity generally use the transmitter antenna position and/or waveform, while methods that use non-cooperative sources have no access to this information. Passive radar is becoming a valuable tool, as many environments have become richer in the available transmissions, such as commercial television, radio, and cell phone towers.

Passive radar has two important benefits over its active counterpart. First, a system of passive receivers results in significant cost and manufacturing advantages. There is no requirement for expensive transmitters and small mobile receivers can be made at a much cheaper cost. Additionally, since the passive radar systems do not introduce any new signals to the environment, they have the stealth advantage and are able to stay active for a longer duration.

Synthetic aperture radar imaging is typically designed for stationary scenes; however, it has many useful properties that are advantageous for moving target imaging. In many applications such as defense and surveillance, most of the targets of interest are moving, and this motion causes smearing artifacts in the reconstructed images. By developing moving target imaging methods for SAR, we can obtain the benefits of traditional SAR while reconstructing focused and accurately positioned moving targets. SAR systems relax the requirement of long antenna and narrow beamwidth by combining measurements over a large, synthetic aperture. Therefore, a large antenna footprint is characteristic of typical SAR systems. This benefits moving target detection and tracking because of the ability to monitor larger areas of the scene for longer periods of time.

1.2 Challenges

Synthetic aperture radar imaging of ground moving targets is a difficult problem on its own, even in the active case where the transmitter parameters can be controlled. In reconstructed images, moving targets often appear smeared and incorrectly located. Special methods must be employed to both focus and correctly position a moving target, which is still an unsolved problem in synthetic aperture radar. Furthermore, the stationary clutter in which the moving target is embedded presents additional challenges. The moving target signal is often relatively weak and embedded in the strong, stationary clutter response of the ground, trees, and man-made structures. Also, since the antennas are moving with respect to the ground, the stationary clutter has a Doppler shift in addition to the moving target.

When considering the scenario of passive synthetic aperture radar, additional challenges are introduced. First, signals of opportunity available from cell phone communications, television, and radio broadcasting towers do not possess the ideal properties ordinarily used for radar. Ultra-narrowband waveforms are often used, which do not have a large enough bandwidth to provide the range resolution necessary for conventional algorithms in SAR. In addition, when non-cooperative transmitters are used, the transmitter location and waveform are unknown. These unknown parameters present significant challenges to conventional SAR methods that do not take these into account.

1.3 Goals

The goal of this thesis is to develop methods to determine both the position and velocity of scatterers in a moving scene using multiple airborne receivers and existing sources of opportunity.

Existing SAR algorithms assume all scatterers in the scene of interest are stationary, and when moving targets are present, artifacts are introduced. First, the moving scatterers appear smeared and unfocused, often times masking their ability to be detected. Second, incorrect velocity estimation, which occurs when a moving target is assumed to be stationary, causes positioning errors. Therefore, the moving targets in the reconstructed images are located offset from their true position. Image reconstruction and velocity estimation algorithms that take this motion into account can provide focused and more accurate SAR images. Furthermore, we wish to understand the nature of these smearing artifacts and positioning errors in order to both explain the artifacts as well as provide a groundwork for more advanced imaging methods in the future.

In addition to developing methods specific to moving target imaging, our goal is to use and understand imaging modalities that take advantage of sources of opportunity, both cooperative and non-cooperative. Our image reconstruction and velocity estimation methods will be able to process the data from multiple moving receivers and exploit their spatial diversity in order to estimate the desired parameters without the knowledge of transmitter locations or transmitted waveforms. Since many waveforms of opportunity are ultra-narrowband, specific methods will need to take these into account in order to form high resolution images when wideband waveforms are not present in the environment.

Finally, moving targets are often embedded in strong, stationary clutter, which can mask the moving target response. Clutter suppression is an important technique which removes or mitigates the response from stationary ground clutter in order to detect moving targets or to better estimate their velocities. Therefore, clutter suppression is an important problem that must be addressed to properly discuss moving target imaging.

1.4 Contributions

Our methods for passive SAR imaging involve developing filtered backprojection type techniques in order to reconstuct the images. These methods have the advantage of being implemented simply and efficiently in practice. In addition, we derive a novel forward model starting with first principles, allowing us to understand and choose accurate approximations to derive the models.

In the first part of this thesis, we consider the problem of passive synthetic aperture imaging of ground moving targets using relatively wideband RF sources of opportunity. Examples of these transmissions are the digital video broadcasting - terrestrial (DVB-T) and WiMax signals. We assume non-cooperative sources of opportunity, meaning the transmitter location and waveform are unknown. For this problem, we take a correlation-based approach in order to backproject the data based on the time difference of arrival between each pair of mobile receivers. We derive a filtered backprojection operator for a given hypothesized velocity such that when this velocity equals the true velocity of a target, it is reconstructed at the correct location and strength. A stack of images is formed over a range of hypothesized velocities, and entropy is used as a measure of focus for each image. Velocity estimation and image reconstruction for each target are performed by taking the images that correspond to the lowest entropy.

Next, we perform a detailed performance analysis for our imaging method. The resolution of position and velocity is addressed by analyzing the bandwidth available in the data in the corresponding position and velocity spaces. We identify various important factors related to signal parameters and imaging geometry that contribute toward the position and velocity resolution. The second task in this performance analysis is analyzing the position error resulting from an incorrectly hypothesized velocity. We derive analytic formulas that relate the error in position in two orthogonal directions as a function of the error in hypothesized velocity. We show that a small change in velocity error induces only a small change in position error.

The second part of this thesis presents methods for imaging moving targets with ultra-narrowband sources of opportunity. The long waveform duration and narrow bandwidth of these signals correspond to an extremely poor range resolution, so these illuminators are unsuitable for the methods developed in the first part. Instead, we use the Doppler resolution in the received signal in order to backproject onto iso-Doppler contours in order to form high resolution images. For the problem of non-cooperative sources of opportunity, we again take a correlation-based approach, but we backproject the temporal frequency difference of arrival between pairs of receivers.

In addition to the method of Doppler synthetic aperture hitchhiker imaging, we also discuss two different methods for clutter suppression in the context of Doppler SAR. We use multiple receivers configured in space and time so that we can suppress stationary clutter and obtain high resolution position and velocity information. The displaced phase center antenna (DPCA) and along-track interferometry (ATI) techniques are well-known techniques in radar to use different sets of data acquired from the same imaging geometry at different times in order to extract the dynamic nature of the scene. We derive the relationship between the two data sets for Doppler SAR and analyze how they can be useful in the context of Doppler SAR imaging of ground moving targets.

1.5 Outline of Thesis

Chapter 2 of this thesis provides a literature survey of important fields that are closely related to passive synthetic aperture radar imaging of moving targets. It starts from moving target imaging with active SAR and then describes various types of passive radar that are related to SAR/GMTI. Chapters 3 and 4 describe our first imaging method that deals with relatively wideband sources of opportunity. Chapter 3 describes the forward model, inversion method, and simulations to demonstrate the results, while chapter 4 presents a detailed performance analysis of key aspects of the method. Chapters 5 and 6 address the second type of waveforms of opportunity: ultra-narrowband waveforms. Chapter 5 introduces the method of using iso-Doppler contours with the hitchhiker modality of synthetic aperture radar. We present a filtered-backprojection method analogous to the one presented in Chapter 3 that backprojects correlated data onto iso-Doppler contours with a hypothesized velocity. Chapter 6 introduces the application of the two-channel clutter suppression techniques displace phase center antenna and along-track interferometry in order to improve moving target detection. Finally, Chapter 7 concludes the thesis.

CHAPTER 2

Literature Survey on Passive SAR Imaging of Moving Targets

Passive synthetic aperture radar imaging of ground moving targets is a relatively unexplored field. However, various closely related fields to passive SAR have been investigated extensively. For example, active SAR imaging of ground moving targets, called SAR/GMTI, has shown some promising results. Additionally, many studies have been done on basic passive radar sytems showing that this technology can be quite useful. Research in passive radar is generally in either the area of detection and tracking or imaging of airborne targets, both using stationary receivers.

2.1 SAR Imaging of Ground Moving Targets (SAR/GMTI)

SAR imaging of ground moving targets, called SAR/GMTI, is well-researched for the active case, when the transmitters are under the control of the radar designer. Originally SAR was designed for imaging a stationary scene, and as a result, moving targets appear smeared in the reconstructed images. The images show prominent streaks, reducing the image quality, and the moving targets cannot be easily detected. SAR/GMTI attempts to detect moving targets and simultaneously form focused images.

In GMTI radar with stationary receivers, clutter can normally be filtered out of the received signal by removing the zero-Doppler components. With moving receivers, advanced processing techniques must be used to handle the spread clutter Doppler. Displaced phase center antenna (DPCA) and space-time adaptive processing (STAP) are two techniques that have been proposed to handle this issue [1], [2].

Combining SAR with GMTI provides many important practical advantages. The two-dimensional SAR image complements the GMTI problem by providing a visual context for the moving target. The image formation process can also be used to detect moving targets in the scene of interest. Conversely, GMTI complements

SAR as well. Detecting and estimating the motion parameters of moving targets can be used to analyze and improve SAR images containing these targets.

SAR/GMTI work varies in terms of the amount of information about the moving scene they assume. These papers generally either require prior information about the moving targets before image formation, or they perform image reconstruction without information about the motion parameters.

Papers that do not require prior information about the motion parameters emphasize the moving target detection over the image formation. The first step is often to employ some kind of clutter suppression. Along track interferometry (ATI) [3] is another technique used for this, in addition to DPCA and STAP. ATI operates by multiplying one received signal by the complex conjugate of the other instead of subtracting the two. The received data is also often transformed in various ways to suppress clutter. [4] describes an approach where time-frequency analysis is used to detect the moving target.

Another technique used in SAR/GMTI that falls into this category is to form images using hypothesized motion parameters and subsequently perform detection and estimation from this stack or sequence of images. In [5], a stack of images is created by hypothesizing a range of velocities for the target. The target can then be detected in this stack since it will be focused in one of the correct velocity images. Alternatively, a measure of focus of the image has been used to determine the accuracy of a hypothesized velocity [6], [7]. With accurately estimated motion parameters, the reconstructed images should be maximally focused, and the contrast should be at its maximum. These papers propose various techniques to iterate and alter the image and parameters until the reconstructed image is sufficiently focused.

The second group of SAR/GMTI papers that often use prior information about the target motion parameters generally emphasize the image formation process over target detection. When this prior information is unavailable, which is often the case, the parameters must be estimated. [8] estimates the motion parameters with maximum likelihood before attempting image formation. In [9], the velocity estimation is achieved by tracking position displacement from single-look SAR images. Various other parameter estimation techniques have also been used, for example in [10] and

[11].

Image formation has also been shown to be viable with techniques that do not require parameter estimation. For example, in [12] a keystone transform is used to correct for the linear range migration while a two-dimensional quadratic phase correction focuses the target in the cross-range direction. Another example is seen in [13], where a two-dimensional matched filtering is constructed with respect to the target and correlated with the image to produced a focused moving target image. Although the target's along track velocity must be known, a presumed value can be used followed by autofocus techniques. Finally, in [14], a SAR image of a moving scene is formed, and subsequently refocused after identifying the moving target's response in the SAR image domain.

2.2 Passive Radar Fundamentals

The idea of passive radar is not new, and its concepts have been explored for many decades. Passive radar grew out of bistatic radar, which started being developed in the 1930s. Bistatic radar, which simply uses a separate transmitter and receiver, was dominant early on because of its simplicity, but the invention of the duplexer allowed the more accurate monostatic version to become popular. Still, bistatic radar has important advantages, many of which are carried over to passive radar.

Despite the absence of knowledge of transmitter locations, passive radar, if used correctly, can provide an extremely capable system. In [15], a potential performance analysis of a simple, stationary passive radar system (also called passive coherent location) is constructed. The work derives a passive form of the bistatic radar equation and investigates the properties of common transmitters. Many of these properties are beneficial for exploitation in passive radar. For example, broadcasting stations have a high transmission power to compensate for low quality receivers with poor noise figures. Furthermore, broadcasting towers tailor the antenna directivity to avoid wasting too much power above the horizon. The paper then investigates in more detail three common types of non-cooperative transmitters: FM radio, cell phone stations, and digital audio broadcasting (DAB).

[16] follows the work done in [15] and investigates waveform properties commonly found in passive radar. The ambiguity functions of various transmission waveforms are computed in order to determine the efficacy of passive coherent location. The resolution in range and Doppler is explored as well as the ambiguities that arise from the multistatic and bistatic antenna geometries. The paper also concludes that most transmission waveforms suitable for passive radar are narrowband and consequently result in good Doppler resolution but poor range resolution.

[17] is another paper that looks at common ambiguity functions found in passive radar and their feasibility. The paper discusses how the signal quality in analog modulation schemes such as FM radio can depend heavily on the content and can degrade at times. One example of this is the degradation in signal quality during pauses in speech. Digital modulation schemes are usually more consistent over time and provide more favorable transmissions.

[18] is one other article investigating passive radar transmission performance. This paper goes into more detail about the properties of various possibilities for passive radar signals, how digital modulation schemes have preferable properties to analog modulation, and how the geometry of transmitters and receivers affects the ambiguity functions of the signals present.

2.3 Passive Detection and Tracking of Airborne Targets

The earliest and most common research done on passive radar systems involves the detection and tracking of airborne targets using stationary, ground-based receivers [19]-[28]. These papers help justify the feasibility of such systems by analyzing the existing sources of opportunity such as television transmissions as well as analog and digital radio. In addition, many of the research shows promising results with simulations of real data or system prototypes generating real aircraft detections.

[19] is one the earliest works to investigate the detection of airborne targets using a passive radar system. The paper investigates performance using the available UHF television signals in the London area. Although, the investigated system did not show stellar performance, the paper proposed significant advantages of a passive

system using only a rudimentary approach. [20] follows this work a decade later and uses a television transmitter and a single receiver to detect and track airborne targets. The proposed system uses the Doppler shift and direction of arrival (DOA) of the received CW television echoes to detect targets and subsequently form and maintain tracks of their positions. Track initialization and maintenance algorithms include a genetic algorithm, the Levenberg-Marquardt algorithm, and an extended Kalman filter. The system is of lower accuracy than a corresponding monostatic implementation, but it has the advantages of simplicity and cost. Finally, this detection and tracking method can be extended to work with any system with a dedicated CW transmitter.

The tracking problem is analyzed further in [21]. Specifically, this article presents an approach to airborne target tracking using FM radio based passive radar. Two filters are presented for tracking: an extended Kalman filter and a particle filter. By incorporating the radar cross section (RCS) in the vector of measurements, the particle filter is able to simultaneously classify while tracking the target. Since the RCS at lower frequencies tends to vary slower with respect to incidence angle, the FM-band waveforms allow the particle filtering approach to be robust for target recognition. This low frequency benefit for examining the RCS of targets is also explored in [23]. This article analyzes the possibility of adding automatic target recognition (ATR) components to passive radar systems. The paper shows some mixed results, but it concludes that the system can be viable when the signal-to-noise ratio is greater than one.

[22] is another paper (similar to [20]) that describes a passive radar detection and tracking system. However, this paper uses FM radio as its transmitter of opportunity instead of television signals. Another addition of this system is that it uses wideband processing to take advantage of range information in the signal instead of just Doppler shift and DOA. The estimates of range, Doppler, and bearing are then fed into a conventional Kalman filter to do the tracking and finally into a nonlinear estimator to estimate the target's location, speed, and heading. The paper succeeded in being able to cancel clutter and direct signal reception from the radio station as well as cross-correlate the data to detect targets in real-time.

[24] shows another implementation for an aircraft detection system, investigating the usage of DAB signals as well as Digital Radio Mondiale (DRM) signals. It's expected that the DRM signals yield poor range information because of their significantly reduced bandwidth as compared to the DAB signals. The system first eliminates the direct path signal, correlates the received signal with the cleaned transmission signal, and then thresholds to reveal any detections. Aircraft from a nearby airport were observed; however, direct transmission from the source could not be completely removed due to Doppler smearing.

Another paper worth noting in relation to passive radar systems is [25]. This paper illustrates in detail a novel multistage algorithm for disturbance removal in a passive bistatic radar system. The algorithm achieves excellent disturbance removal, and it also allows for strong target echo cancellation such that weaker targets can be detected. The algorithm was run on real data, and in addition, a suboptimal but less complex computationally was presented.

In [26], the standard multichannel techniques of DPCA and STAP are applied to a passive airborne system to in order to detect ground moving targets. Although it does not perform SAR imaging, it shows promising results for airborne passive radar in conjunction with ground moving targets.

2.4 Passive Imaging with Stationary Receivers

The next major category of research relevant to passive SAR moving target imaging is deals with the passive imaging of targets using stationary receivers. Often, these systems are intended to image airborne targets to function as an inverse synthetic aperture (ISAR), but ground scenes can be imaged as well. As described in [29], image formation has merit for automatic target recognition when the target is not already in the recognition system's library. Additionally, it can be very useful to present these images to human observers for analysis. These passive imaging systems with stationary receivers evolve and complement the detection and tracking systems nicely by either directly substituting or providing images to aid overseas monitoring.

In [30], the airborne target imaging problem was studied by simulating TV station data. The television transmissions were used as sources of opportunity for a passive receiver system to perform the imaging. The study performed the image formation by direct Fourier reconstruction (DFR), which involves interpolating the sampled Fourier data on a grid and performing a 2D IFFT. To verify the theory, the algorithm was performed on data generated from the Fast Illinois Solver Code (FISC). In order to make the simulations computationally tractable, only one frequency was simulated. Therefore, this paper shows a rough lower bound on the results from this type of imaging configuration. It is expected that useful images could be formed from reflected television signals from multiple stations.

[31] analyzes a passive imaging algorithm for a similar situation as [30], where reflected television signals are used as illuminators of opportunity. However, while [30] used DFR to reconstruct the images, this paper substitutes usage of the Smoothed Pseudo Wigner-Ville Distribution (SPWVD) in place of the FFT in the cross-range direction. The paper shows that this approach avoids degradations that are caused by the Fourier transform. Finally, results are presented from simulations of realistic data generated by FISC, showing improved images created by the SPWVD algorithm.

[32] presents another approach to image formation of airborne targets with passive receivers. This paper once again presents a series of simulations based on data generated by FISC. The CLEAN deconvolution algorithm is commonly used in radio astronomy to perform image reconstruction. Since radio astronomy has a remarkable resemblance to passive radar imaging in that they both must correlate received signals and reconstruct from a sparse Fourier representation, the CLEAN algorithm was applied to the passive radar imaging scenario. Although some of the resulting images are improved, overall the CLEAN algorithm (at least by itself) does not seem to provide any benefit over DFR. One important reason for this is that passive radar requires lower frequency waveforms. These lower frequencies do not fit into the CLEAN algorithm's assumption of distinct point scatterers. Additionally, the CLEAN algorithm was designed to work with real data, but the data involved in passive radar imaging is complex.

[33] and [34] both try to further improve on passive radar imaging by applying

a region-enhanced image formation technique to the passive imaging scenario. The passive nature of the imaging problem causes the Fourier domain data to be sparse, and hence direct Fourier reconstruction yields significant artifacts in the resulting image. This region-enhanced image formation approach attempts to mitigate these artifacts by emphasizing region-based features over point-based features. The study uses simulated data from FISC and presents very promising results for the region-enhanced image reconstruction technique.

Another example of airborne target imaging with passive receivers is shown in [35]. The algorithm is based on using multiple transmitter receiver pairs as subapertures to synthesize a wide aperture for imaging without the requirement for large rotation or interpolation. Normally, the rotation an object undergoes about a receiver is very small, which limits the imaging capability of an algorithm such as DFR. This algorithm avoids that limitation and does show some promising simulation results, but also requires many sources of opportunity surrounding the target.

Passive imaging with sparse distributed apertures has been investigated in [36] and [37]. These paper assume a sparse distribution of stationary, passive receivers in order to exploit transmitters of opportunity and image a scene of interest. These works take a statistical approach and form both position and velocity space images by maximizing a test statistic signal-to-noise ratio.

2.5 Passive SAR Imaging

To the best of our knowledge, no work has been published to address the problem of passive SAR imaging of ground moving targets using non-cooperative sources of opportunity. However, there has been work done in the field of passive SAR imaging of stationary scenes or airborne targets, similar to the previous category of research.

[38] presents a passive SAR system using geostationary satellites attempting to image very large areas of the ground. The system assumes one receiving satellite and one DAB transmitting satellite. Cross-correlation of the received signal with a replica of the transmitted signal gives the range compressed form of the signal and is

used for slant range focusing. Focusing in the azimuth direction is accomplished by phase shifting parts of the signal to compensate for beam steering factor and then integrate in the cross-range direction. The system uses extremely long integration times of about a half of a day, so any targets that are moving are not imaged at all. Although this system is not applicable for GMTI, it does provide some insight into the challenges of passive SAR.

In [39] a passive bistatic radar experiment is conducted using an airborne receiver and attempting to detect airborne targets. As with many passive systems, the algorithm employed direct path signal suppression to separate the return from the target from the transmitting antenna followed by a constant false alarm rate detection scheme.

[40] presents a passive SAR system for a ground-based scene of interest. The transmitters of opportunity are space-based global navigation satellite systems such as GPS transmitters. These systems are constructed in such a way to provide every point on the other direct sight to multiple transmitters, which allows for spatially diverse radiation for passive radar. The paper uses a basic signal processing scheme and demonstrates promisingly that results are analogous to a reduced-aperture monostatic system.

In [41]-[43], passive SAR imaging methods are developed for receivers located on aircraft flying over a scene of interest. [41] presents a system called synthetic aperture hitchhiker imaging (SAH) with an arbitrary number of transmitters and receivers and arbitrary flight trajectories. Each pair of received signals is windowed, scaled, and cross-correlated, which gives a resulting operator with the transmitter terms in the phase eliminated. The image is formed by filtered backprojection of each of these correlations onto the scene radiance and finally summed together. [42] and [43] show an analogous approach using Doppler-based measurements instead of range or time measurements. This method, called Dopper synthetic aperture hitchhiker (DSAH) imaging, makes the assumption of ultra-narrowband waveforms as the transmitters' signals. These hitchhiker systems don't directly deal with moving target imaging, but they provide a relevant set of work on which passive SAR/GMTI studies can be based.

CHAPTER 3

Passive Synthetic Aperture Hitchhiker Imaging of Ground Moving Targets - Image Formation and Velocity Estimation

3.1 Introduction

3.1.1 Motivation

A hitchhiker is a passive radar receiver that uses sources of opportunity instead of a dedicated transmitter [15], [16], [30], [32], [33], [41]-[43]. The rapid growth of radio, cell phone, and television transmission towers provides ample opportunities for these hitchhikers to perform radar tasks. Additionally, the absence of active signal propagation from the system provides key advantages such as cost, simplicity of implementation, and stealth.

Synthetic aperture radar (SAR) image formation methods are typically designed for imaging stationary scenes, and reconstructing scenes with moving targets is a challenging task. These moving targets appear smeared and unfocused in reconstructed images. Many methods have been presented in the literature that attempt to address the problem of SAR imaging of ground moving targets (SAR/GMTI) [3]-[5], [8]-[13], [44]. Synthetic aperture hitchhiker imaging of ground moving targets (SAH/GMTI) involves high resolution position and velocity estimation of a scene using transmitters of opportunity and multiple moving receivers. The transmitters of opportunity can be cooperative where the location of transmitters and transmitted waveforms are known or non-cooperative where no such information is available.

In this chapter, we develop a novel forward model and a corresponding image formation method to reconstruct both the scene reflectivity and the two-dimensional velocity of multiple moving targets using non-cooperative sources of opportunity. Our method extends the passive imaging of stationary scene that was presented in

---

This chapter is to appear in: S. Wacks and B. Yazici, "Passive synthetic aperture hitchhiker imaging of ground moving targets - part 1: Image formation and velocity estimation," *IEEE Trans. Image Process.*.

[41].

3.1.2 Related Work

To the best of our knowledge, no work has been published to address the problem of passive synthetic aperture radar imaging of ground moving targets using non-cooperative sources of opportunity. However, literature on passive SAR imaging of stationary scenes using non-cooperative sources of opportunity can be found in [41]-[43]. In [41], an image reconstruction method is developed using filtered backprojection (FBP) on data correlated between the receivers to image a stationary scene. Similarly, [42] and [43] present methods of passive SAR imaging of a stationary scene, but using ultra-narrowband waveforms of opportunity.

Several recent studies reported on passive imaging of moving and stationary scenes using cooperative sources of opportunity [26]-[28]. These methods rely on collecting the direct path signal from a transmitter of opportunity and using this signal in conventional bistatic radar imaging mode. In [39], a passive bistatic radar experiment is conducted using an airborne receiver attempting to detect airborne targets. The algorithm employed direct path signal suppression followed by a constant false alarm rate detection scheme.

In addition to passive SAR imaging of a stationary scene, there has been work published on passive radar imaging of moving targets with stationary receivers using both cooperative and non-cooperative sources of opportunity [15], [16], [19], [20], [22], [24], [30], [32], [33], [37], [45]. For example, [37] uses a sparse array of stationary receivers to take advantage of transmitting sources of opportunity to image moving targets. [15], [16], [40], [46]-[54] investigate the properties of passive radar and look at the potential performance one can obtain from such a system. [30], [32], and [33] all show image reconstruction methods for passive imaging of airborne targets with stationary receivers. [30] uses the simplest algorithm, direct Fourier reconstruction, to establish a lower bound and show the viability of passive imaging. [32] and [33] improve on the performance of the direct Fourier reconstruction by applying CLEAN deconvolution and region-enhanced image formation techniques, respectively.

On the other hand, SAR/GMTI with active transmitters has an extensive research base. Additionally, some systems may be called passive in a cooperative case, when the transmitter position and waveform is known. Papers that have studied this problem generally either focus on detecting the moving targets either independently or for use with other image formation techniques, or they focus on the image formation process itself. For example, [3] and [4] focus on the target detection. [3] performs the detection in multichannel SAR using displaced phase center antenna (DPCA) and along-track interferometry (ATI) techniques, which suppress clutter by either subtracting signals from two channels or multiplying the complex conjugates, respectively. [4] performs the detection by using time-frequency analysis to estimate Doppler information for the moving target. In addition to DPCA and ATI, space-time adaptive processing is an important, well-known technique primarily used for clutter suppression, and is described in [2], [55], and [56]. Examples of works that focus on image formation are [12] and [13]. [12] performs a keystone transform to correct for the linear migration, and [13] performs a two-dimensional matched filtering operation to produce a focused image of the moving target.

Another technique used in SAR/GMTI is to form images using hypothesized motion parameters and subsequently perform detection and estimation from this stack or sequence of images. In [5], a stack of images is created by hypothesizing a range of velocities for the target. The target can then be detected in this stack since it will be focused in one of the correct velocity images. Alternatively, a measure of focus of the image has been used to determine the accuracy of a hypothesized parameter [6], [7], [57]-[62]. With accurately estimated motion parameters, the reconstructed images should be maximally focused, and the contrast should be at its maximum. These papers propose various techniques to iterate and alter the image and parameters until the reconstructed image is sufficiently focused.

3.1.3 Overview and Advantages of Our Work

This chapter presents a method of imaging ground moving targets using a network of airborne receivers and non-cooperative transmitters of opportunity. A novel forward model is formed by correlating the received signal between pairs of receivers. This forward model can be viewed as a generalized Radon transform where the weighted/filtered function of interest is projected onto warped passive iso-range contours that are determined by target velocities and imaging geometry. We develop a corresponding filtered backprojection (FBP) type approximate inverse and form a stack of position images, each one corresponding to a fixed velocity for a range of hypothesized velocities. We show that when the hypothesized velocity is equal to the true velocity of a target, the backprojection operator puts the target at the correct position in the reconstructed image. We design the filter so that the target is at the correct strength whenever the hypothesized velocity is equal to the true velocity of the target. Next, we use entropy as a measure of focus to determine the accuracy of the hypothesized velocity and to estimate the correct target velocities. We present numerical simulations to demonstrate the performance of the method in imaging multiple moving targets at different velocities. Although our method does not consider clutter explicitly, the simulation study shows that the image formation and entropy based velocity estimation are robust at moderate signal-to-noise and signal-to-clutter ratios.

In addition to the advantages provided by a passive system using non-cooperative transmitters of opportunity, our method provides several advantages over other SAR moving target imaging methods. The FBP method for image reconstruction uses a two-dimensional vector for the hypothesized velocity. Therefore, the method has the ability to reconstruct both components of the velocity of moving targets instead of only a single component. Another advantage of our method is that there is no assumption of a single target; instead, multiple moving targets moving at different velocities can be reconstructed. Additionally, stationary components of the scene are not filtered, so both stationary and moving targets may be reconstructed simultaneously. Our work does not require prior information about the motion parameters of moving targets. The images and focus measure together provide the detection and estimation capability of moving targets and their motion parameters. The method can be numerically implemented efficiently with roughly the computational complexity of fast-backprojection algorithms [63]. Finally, the forward model and inversion method make no assumptions about receiver flight trajectories or the ground topography; therefore, our method applies to arbitrary imaging geometries.

In the next chapter, we present a performance analysis of the inversion and velocity estimation methods developed in this chapter. In particular, we present the position and velocity analysis of our method and develop a theory to analyze and predict smearing artifacts in position images due to erroneous velocity estimation. These analysis is important for understanding the capability and limitations of our method as well as designing a system that yields the best performance possible.

3.1.4 Organization of the Chapter

The organization of the remainder of the chapter is as follows: In Section 3.2 we introduce the models for a moving target and the signal scattered from a moving scene. Then, in Section 3.3, we develop the forward model for passive SAR/GMTI. In Section 3.4, we develop the FBP-type image formation method for reconstruction of position images entropy-based velocity estimation method. Section 3.5 details the step-by-step procedure of the algorithm and analyzes its computational complexity. In Section 3.6, we present numerical simulations to illustrate the theoretical results and to demonstrate the robustness of our method in noise and clutter. Section 3.7 concludes the chapter.

3.2 Moving Target and Received Signal Models

Throughout the chapter, we will use bold non-italic fonts to denote vectors in 3D, bold italic fonts to denote 2D vectors, and non-bold italic fonts to denote scalar quantities, i.e., $\mathbf{x} = [x_1,\ x_2,\ x_3] \in \mathbb{R}^3$, $\boldsymbol{x} = [x_1,\ x_2] \in \mathbb{R}^2$, $x_i \in \mathbb{R}$, $i = 1, 2, 3$. We will use calligraphic letters, such as $\mathcal{F}$ and $\mathcal{K}$ to denote operators.

We let $\mathbf{x}$ be a location on the ground where $\mathbf{x} = [\boldsymbol{x}, \psi(\boldsymbol{x})] \in \mathbb{R}^3$, $\boldsymbol{x} \in \mathbb{R}^2$, and $\psi : \mathbb{R}^2 \to \mathbb{R}$ is a known smooth function for the ground topography. Since the scattering takes place in a thin region near the surface and does not penetrate deep into the ground, the reflectivity function $V(\mathbf{x})$ is of the form

$$V(\mathbf{x}) = \rho(\boldsymbol{x})\delta(x_3 - \psi(\boldsymbol{x})), \tag{3.1}$$

with $\rho(\boldsymbol{x})$ representing the 2D surface reflectivity of a point on the ground.

3.2.1 Model for the Moving Target

We now model the scatterers as moving targets and their position $\mathbf{z}$ as a function of time. We denote $s \in \mathbb{R}$ as the *slow-time*, which indexes each "data processing window." Additionally, we make the start-stop approximation for both the moving targets and receiving antennas. The start-stop approximation on the receiving antennas assumes that the range variation during a pulse reception is negligible compared to the range variation between each pulse. Similarly, the start-stop approximation on the moving targets assumes that the range variation due to the movement of the targets is negligible during a pulse reception as compared to the range variation between each pulse. Without loss of generality, we let $\mathbf{x}$ be the position of the targets at the beginning of time ($s = 0$), i.e, the beginning of the synthetic aperture. Using the assumption of constant velocity for each moving target throughout the synthetic aperture, we represent the trajectory of a scatterer by

$$\mathbf{z}(s) = \mathbf{x} + \mathbf{v}_{\mathbf{x}} s, \tag{3.2}$$

where $\mathbf{v}_{\mathbf{x}}$ is the velocity of a particular point scatterer located at point $\mathbf{x}$ when $s = 0$. Note that the linear target motion model may limit the length of each receiver aperture or coherent processing interval (CPI). However, as described in Section 3.4.1, the use of multiple receiver apertures may compensate for the effect of a short CPI. Since the targets are all located on the ground, and we have a known function of the ground topography, the velocity of the scatters $\mathbf{v}_{\mathbf{x}}$ has the form

$$\mathbf{v}_{\mathbf{x}} = [\boldsymbol{v}_{\boldsymbol{x}}, \nabla_{\boldsymbol{x}} \psi(\boldsymbol{x}) \cdot \boldsymbol{v}_{\boldsymbol{x}}], \tag{3.3}$$

where $\nabla_{\boldsymbol{x}} \psi(\boldsymbol{x}) = [\partial_{x_1} \psi(\boldsymbol{x}) \;\; \partial_{x_2} \psi(\boldsymbol{x})]$ is the gradient of the ground topography.

3.2.2 Model for the Received Signal From Moving Targets

We assume that there are N receivers, each traversing a trajectory $\boldsymbol{\gamma}_i(s)$, $i = 1, ..., N$ over a scene of interest. The model derived in [64] for a moving scene describes the signal received at the ith receiver from a single, stationary transmitter located at $\mathbf{y}$ as follows:

$$\begin{aligned} f_i(s,t) = \int & e^{-i\omega[t-(|\mathbf{x}-\boldsymbol{\gamma}_i(s)|+|\mathbf{x}-\mathbf{y}|)/c_0-((\widehat{\mathbf{x}-\boldsymbol{\gamma}_i(s)})+(\widehat{\mathbf{x}-\mathbf{y}}))\cdot\mathbf{v}_{\mathbf{x}}s/c_0]} \\ & \rho(\boldsymbol{x})A_i(\omega,s,\boldsymbol{x},\boldsymbol{v})\,d\omega d\boldsymbol{x}, \end{aligned} \tag{3.4}$$

where c_0 is the speed of light, $A_i(\omega,s,\boldsymbol{x},\boldsymbol{v})$ is a slow varying amplitude term in ω given by

$$A_i(\omega,s,\boldsymbol{x},\boldsymbol{v}) = \frac{J_{R_i}(\omega,\boldsymbol{x},s)J_T(\omega,\boldsymbol{x})}{(4\pi)^2|\mathbf{x}+\mathbf{v}_{\mathbf{x}}s-\boldsymbol{\gamma}_i(s)||\mathbf{x}+\mathbf{v}_{\mathbf{x}}s-\mathbf{y}|}, \tag{3.5}$$

and includes the transmitter and receiver antenna beam patterns, J_T and J_{R_i} and the geometric attenuation factors in the denominator. Note that while J_{R_i}, $i=1,...,N$ are known, J_T, which depends primarily on the transmitted waveform, may not be known.

3.3 Forward Model

This section derives a forward model for passive synthetic aperture imaging of ground moving targets using the moving target and received signal models presented in the previous section. The forward model is based on the cross correlation of the received signal obtained at each synthetic aperture sampling interval for each pair of receiving antennas. The radiance (position) image formation and velocity estimation will be based on the inversion of the forward model described in this section.

3.3.1 Cross-Receiver Correlation

Using (3.4) as our model for the signal received by each antenna, the cross-correlation of each pair of signals for each data processing window is

$$f_{ij}(s,\tau) = \int f_i(s,t)f_j^*(s,t-\tau)\,dt,\ \ i,j=1,...,N,\ i\neq j, \tag{3.6}$$

where f^* denotes the complex conjugate of f, $t\in[0,T]$ is the fast-time variable for some T representing the length of the data processing window.

We can now express the correlation of pairs of received signals at corresponding receiver antenna positions as

$$\begin{aligned} f_{ij}(s,\tau) = \int & e^{-i\omega[t-(|\mathbf{x}-\boldsymbol{\gamma}_i(s)|+|\mathbf{x}-\mathbf{y}|)/c_0-((\widehat{\mathbf{x}-\boldsymbol{\gamma}_i(s)})\cdot\mathbf{v}_{\mathbf{x}}+(\widehat{\mathbf{x}-\mathbf{y}})\cdot\mathbf{v}_{\mathbf{x}})s/c_0]} \\ & \times e^{i\omega[t-\tau-(|\tilde{\mathbf{x}}-\boldsymbol{\gamma}_j(s)|+|\tilde{\mathbf{x}}-\mathbf{y}|)/c_0-((\widehat{\tilde{\mathbf{x}}-\boldsymbol{\gamma}_j(s)})\cdot\mathbf{v}_{\tilde{\mathbf{x}}}+(\widehat{\tilde{\mathbf{x}}-\mathbf{y}})\cdot\mathbf{v}_{\tilde{\mathbf{x}}})s/c_0]} \\ & \times A_{R_{ij}}(\omega,s,\boldsymbol{x},\tilde{\boldsymbol{x}},\boldsymbol{v}_x,\boldsymbol{v}_{\tilde{x}}) \\ & \times \rho(\boldsymbol{x})\rho^*(\tilde{\boldsymbol{x}})\frac{J_T(\omega,\boldsymbol{x})J_T^*(\omega,\tilde{\boldsymbol{x}})}{(4\pi)^2|\mathbf{x}+\mathbf{v}_{\mathbf{x}}s-\mathbf{y}||\tilde{\mathbf{x}}+\mathbf{v}_{\tilde{\mathbf{x}}}s-\mathbf{y}|}\,d\omega d\boldsymbol{x}d\tilde{\boldsymbol{x}}dt \end{aligned} \tag{3.7}$$

where

$$A_{R_{ij}}(\omega,s,\boldsymbol{x},\tilde{\boldsymbol{x}},\boldsymbol{v}_x,\boldsymbol{v}_{\tilde{x}}) = \frac{J_{R_i}(\omega,\boldsymbol{x},s)J_{R_j}^*(\omega,\tilde{\boldsymbol{x}},s)}{(4\pi)^2|\mathbf{x}+\mathbf{v}_{\mathbf{x}}s-\boldsymbol{\gamma}_i(s)||\tilde{\mathbf{x}}+\mathbf{v}_{\tilde{\mathbf{x}}}s-\boldsymbol{\gamma}_j(s)|}. \tag{3.8}$$

Note that $A_{R_{ij}}$ includes only the known terms.

Since the reflectivity ρ and the transmitter terms are unknown we take a statistical approach and take the expected value of the correlated signal in (3.7). Additionally, we assume that the scene reflectivity and transmitter terms are statistically independent, and therefore,

$$E[\rho(\boldsymbol{x})\rho^*(\tilde{\boldsymbol{x}})J_T(\omega,\boldsymbol{x})J_T^*(\omega,\tilde{\boldsymbol{x}})] = E[\rho(\boldsymbol{x})\rho^*(\tilde{\boldsymbol{x}})]E[J_T(\omega,\boldsymbol{x})J_T^*(\omega,\tilde{\boldsymbol{x}})]. \tag{3.9}$$

Furthermore, we make the incoherent field approximation [65] and write

$$E[\rho(\boldsymbol{x})\rho^*(\tilde{\boldsymbol{x}})] = R_\rho(\boldsymbol{x})\delta(\boldsymbol{x}-\tilde{\boldsymbol{x}}) \tag{3.10}$$

where R_ρ and R_T are the scene radiance and transmitter irradiance, respectively. Note that the incoherent field approximation is valid as long as $E[\rho(\boldsymbol{x})\rho^*(\tilde{\boldsymbol{x}})]$ has a correlation length within half of a wavelength of the carrier frequency of the transmitter of opportunity (see page 526 of [65]). Under the incoherent field approximation, we write $E[J_T(\omega,\boldsymbol{x}){J_T}^*(\omega,\boldsymbol{x})] = R_T(\omega,\boldsymbol{x})$ where R_T denotes transmitter irradiance.

We now define the *phase-space radiance function* as

$$\begin{aligned} r(\boldsymbol{x},\boldsymbol{v}) &= R_\rho(\boldsymbol{x})\delta(\boldsymbol{v}-\boldsymbol{v}_{\mathbf{x}}) \\ &\approx R_\rho(\boldsymbol{x})\varphi(\boldsymbol{v},\boldsymbol{v}_{\mathbf{x}}), \end{aligned} \tag{3.11}$$

where $\varphi(\boldsymbol{v},\boldsymbol{v}_x)$ is a smooth, differentiable function of $\boldsymbol{v}$ that approximates the Dirac delta function in the limit, such as a Gaussian or sinc function.

3.3.2 Forward Model for SAH/GMTI

Using (3.9)-(3.10), the expected value of the correlated received signal can be modeled as

$$\begin{aligned} d_{ij}(s,\tau) &= E[f_{ij}(s,\tau)] := \mathcal{F}[r](s,\tau) \\ &= \int e^{-i\omega[\tau - R_{ij}(\mathbf{x},s)/c_0 - B_{ij}(\mathbf{x},\mathbf{v},s)/c_0]} A_{ij}(\omega,s,\boldsymbol{x},\boldsymbol{v}) r(\boldsymbol{x},\boldsymbol{v})\, d\boldsymbol{v} d\boldsymbol{x} d\omega \end{aligned} \tag{3.12}$$

where

$$A_{ij}(\omega,s,\boldsymbol{x},\boldsymbol{v}) = A_{R_{ij}}(\omega,s,\boldsymbol{x},\boldsymbol{v}) \frac{R_T(\omega,\boldsymbol{x})}{(4\pi)^2|\mathbf{x}+\mathbf{v}_{\mathbf{x}}s-\mathbf{y}|^2} \tag{3.13}$$

$$R_{ij}(\mathbf{x},s) = |\mathbf{x}-\boldsymbol{\gamma}_i(s)| - |\mathbf{x}-\boldsymbol{\gamma}_j(s)| \tag{3.14}$$

$$B_{ij}(\mathbf{x},\mathbf{v},s) = [(\widehat{\mathbf{x}-\boldsymbol{\gamma}_i(s)}) - (\widehat{\mathbf{x}-\boldsymbol{\gamma}_j(s)})] \cdot \mathbf{v}s, \tag{3.15}$$

where $\widehat{\mathbf{x}}$ is the unit vector in the direction of $\mathbf{x}$. We define

$$\mathbf{L}_{ij}(\mathbf{x},s) = [(\widehat{\mathbf{x}-\boldsymbol{\gamma}_i(s)}) - (\widehat{\mathbf{x}-\boldsymbol{\gamma}_j(s)})] \tag{3.16}$$

as the *hitchhiker look direction*. In this model, R_{ij} is the *hitchhiker range* introduced in [41], and B_{ij} can be viewed as the displacement in the hitchhiker look direction due to the movement of the target at $\mathbf{x}$.

We assume that there is some m_A such that A satisfies

$$\sup_{(\omega,s,\boldsymbol{x})\in\mathcal{U}} |\partial_\omega^\alpha \partial_s^\beta \partial_{x_1}^{\rho_1} \partial_{x_2}^{\rho_2} A(\omega,s,\boldsymbol{x})| \leq C_A(1+\omega^2)^{(m_A-|\alpha|)/2} \tag{3.17}$$

where $\mathcal{U}$ is any compact subset of $\mathbb{R}\times\mathbb{R}\times\mathbb{R}^2$ and C_A depends on $\mathcal{U}$, α, β, ρ_1, and

ρ_2. Under (3.17), the forward operator $\mathcal{F}$ is defined as a Fourier Integral Operator (FIO) [66, 67]. The phase term of $\mathcal{F}$ is given by

$$\phi_{ij}(\omega, \mathbf{x}, \mathbf{v}, \tau, s) = \omega[\tau - R_{ij}(\mathbf{x}, s)/c_0 - B_{ij}(\mathbf{x}, \mathbf{v}, s)/c_0] \tag{3.18}$$

and its amplitude term is A_{ij} as defined in (3.13).

We now pose the passive synthetic aperture imaging of moving targets as the inversion of the forward map $\mathcal{F}$.

3.3.3 Critical Points of the Forward Model

An FIO can be viewed as a generalized Radon transform that projects the weighted or filtered version of an input function onto some smooth manifolds such as circles, ellipsoids etc. The weighting or filtering is defined by the amplitude term and the smooth manifolds are defined by the phase function of the FIO. If the amplitude function is identically equal to 1, then the FIO simply projects the input function onto the manifolds defined by its phase term. To understand the underlying geometry, the nature of the data d_{ij} that will be used for inversion, and to develop an inverse map for $\mathcal{F}$, we study the geometry of these curved manifolds.

The main contributions to d_{ij} come from the projection of the phase-space radiance function onto the curved manifolds which are given by the critical set $\{(\boldsymbol{x}, \boldsymbol{v}) \in \mathbb{R}^2 \times \mathbb{R}^2 : \partial_\omega \phi = 0, (\boldsymbol{x}, \boldsymbol{v}) \in \operatorname{supp}(A_{ij})\}$ of the phase ϕ [66, 67]. We denote these four-dimensional surfaces defined in position and velocity spaces by

$$H_{ij}(s, \tau) = \{(\boldsymbol{x}, \boldsymbol{v}) \in \mathbb{R}^2 \times \mathbb{R}^2 : R_{ij}(\mathbf{x}, s) + B_{ij}(\mathbf{x}, \mathbf{v}, s) = \tau c_0\} \tag{3.19}$$

and refer to them as *hitchhiker moving target iso-range surfaces.* In order to visualize this four-dimensional manifold we consider the following two cross sections for constant velocity and constant position:

$$H_{ij,\boldsymbol{v}_0}(s, \tau) = \{\boldsymbol{x} \in \mathbb{R}^2 : R_{ij}(\mathbf{x}, s) + B_{ij}(\mathbf{x}, \mathbf{v}_0, s) = \tau c_0, (\boldsymbol{x}, \boldsymbol{v}_0) \in \operatorname{supp}(A_{ij})\} \tag{3.20}$$

$$H_{ij,\boldsymbol{x}_0}(s, \tau) = \{\boldsymbol{v} \in \mathbb{R}^2 : R_{ij}(\mathbf{x}_0, s) + B_{ij}(\mathbf{x}_0, \mathbf{v}, s) = \tau c_0, (\boldsymbol{x}_0, \boldsymbol{v}) \in \operatorname{supp}(A_{ij})\}. \tag{3.21}$$

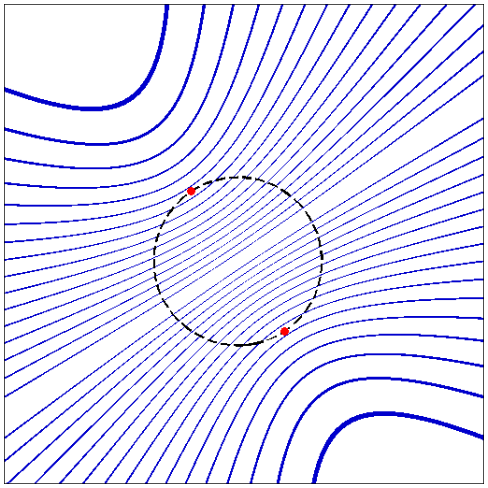

Figure 3.1: Position-space iso-range contours for a stationary target. In this case the contours in 4D space are hyperboloids, and when intersected with a flat topography form the hyperbolas shown here.

We refer to $H_{ij,\boldsymbol{v}_0}$ as the *position-space hitchhiker iso-range curve* and $H_{ij,\boldsymbol{x}_0}$ as the *velocity-space hitchhiker iso-range curve*. Figures 3.1, 3.2, and 3.3 show examples of these contours for a flat topography ($\psi(\boldsymbol{x}) = 0$). Figure 3.1 shows position-space curves with an assumption of zero velocity for the moving target. The manifolds in 4D space are hyperboloids with the two receivers as foci, and they form hyperbolas when intersected with the ground. A non-zero velocity warps these contours, as shown in Figure 3.2. Figure 3.3 shows examples of velocity-space contours. These curves are simply straight lines since the phase is linear in $\mathbf{v}$.

3.4 Image Formation

The goal for reconstruction is to form an image that is simultaneously focused in both position and velocity spaces. A logical choice would be to backproject the data onto the four-dimensional hitchhiker moving target iso-range surfaces described in the previous section. However, since the data in hand is only two-dimensional, we may not be able to reconstruct the image so that the underlying point spread function (PSF) is approximately a Dirac delta function in both the position and velocity spaces.

To reconstruct a position (radiance) image of the scene, we assume a fixed, hy-

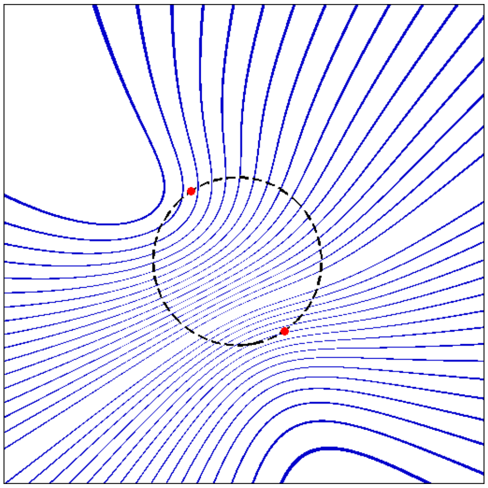

Figure 3.2: Position-space iso-range contours for a moving target with velocity (50,100) on a flat topography and two receivers cross-correlating their data. With zero velocity, these curves would be hyperbolas, but the moving target warps these contours.

pothesized velocity $\boldsymbol{v}_h$ for the scene and then backproject onto the two-dimensional position-space iso-range cross section for $\boldsymbol{v}_h$. We refer to this position image as the $\boldsymbol{v}_h$-radiance image. We show in the point spread function analysis section that whenever $\boldsymbol{v}_h$ is equal to the true velocity $\boldsymbol{v}_{\mathbf{x}}$ of the scatterer at $\mathbf{x}$, backprojecting onto the position-space iso-range cross section places the reconstructed scatterer at the correct location. We next design the filter so that the PSF of the imaging operator is approximately a Dirac delta function. We perform this process for a range of hypothesized velocities, yielding a stack of these $\boldsymbol{v}_h$-radiance images. By measuring the entropy of each image, we can determine the degree of smearing of the scatterers, and simultaneously the accuracy of the hypothesized velocities. We search the stack of images for the one with the lowest entropy along with their corresponding velocity estimates for each target.

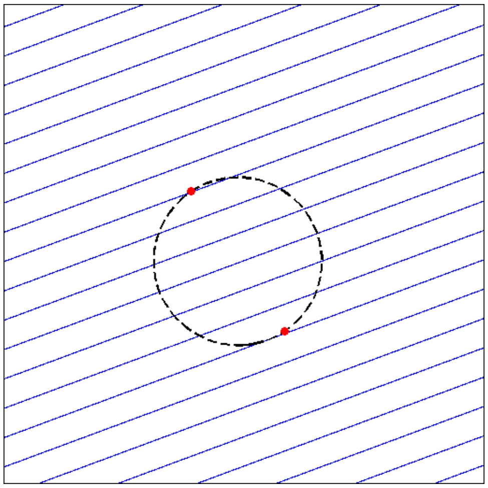

Figure 3.3: Velocity-space iso-range contours for a moving target with velocity (50,100). These contours form lines since the phase has a simple linear relationship in the velocity.

3.4.1 Filtered Backprojection Operator

For a given velocity $\mathbf{v}_h$ and a given pair of receivers, we define the filtered backprojection operator as

$$\begin{aligned}\mathcal{K}[d_{ij}](\boldsymbol{x}') &= \hat{r}_{ij}^{\boldsymbol{v}_h}(\boldsymbol{x}') \\ &= \int e^{i\omega[\tau - R_{ij}(\mathbf{x}',s)/c_0 - B_{ij}(\mathbf{x}',\mathbf{v}_h,s)/c_0]} d_{ij}(s,\tau) Q_{ij}^{\boldsymbol{v}_h}(\omega,s,\boldsymbol{x}')\, d\omega ds d\tau,\end{aligned} \tag{3.22}$$

where $Q_{ij}^{\boldsymbol{v}_h}(\omega,s,\boldsymbol{x}')$ is the filter to be determined later.

Under the assumption that $Q_{ij}^{\boldsymbol{v}_h}$ satisfies a similar condition to (3.17), $\mathcal{K}$ becomes an FIO. Note that $\mathbf{v}_h$ is simply a fixed parameter, not an argument of $\mathcal{K}$.

Our reconstructed image is the sum of all pairs of images $\hat{r}_{ij}^{\boldsymbol{v}_h}$:

$$\hat{r}^{\boldsymbol{v}_h}(\boldsymbol{x}') = \sum_{i,j} \hat{r}_{ij}^{\boldsymbol{v}_h}(\boldsymbol{x}') \quad i \neq j,\ i,j = 1,...,N, \tag{3.23}$$

Note that the assumption of linear target motion can be violated for sufficiently long apertures or CPI. However, use of multiple pairs of receivers can extend the effective aperture length without extending the CPI, compensating for potential loss of resolution due to short CPI.

3.4.2 Point Spread Function of the Imaging Operator

By substituting (3.12) into (3.23) and performing the $d\tau$ integration by setting $\omega = \omega'$, we obtain

$$\begin{aligned}\hat{r}^{\boldsymbol{v}_h}(\boldsymbol{x}') = \sum_{i,j} \int & e^{i\omega[R_{ij}(\mathbf{x}',s)/c_0 + B_{ij}(\mathbf{x}',\mathbf{v}_h,s)/c_0 - R_{ij}(\mathbf{x},s)/c_0 - B_{ij}(\mathbf{x},\mathbf{v},s)/c_0]} \\ & \times A_{ij}(\omega, s, \boldsymbol{x}, \boldsymbol{v}) Q_{ij}^{\boldsymbol{v}_h}(\omega, s, \boldsymbol{x}') r(\boldsymbol{x}, \boldsymbol{v})\, d\boldsymbol{x} d\boldsymbol{v} d\omega ds \\ = {} & \mathcal{K}\mathcal{F}[r](\boldsymbol{x}').\end{aligned} \tag{3.24}$$

Our image fidelity operator is in the form

$$\hat{r}^{\boldsymbol{v}_h}(\boldsymbol{x}') = \sum_{i,j} \int L_{ij}^{(\boldsymbol{v},\boldsymbol{v}_h)}(\boldsymbol{x}, \boldsymbol{x}') r(\boldsymbol{x}, \boldsymbol{v})\, d\boldsymbol{x} d\boldsymbol{v} \tag{3.25}$$

$$\begin{aligned}L_{ij}^{(\boldsymbol{v},\boldsymbol{v}_h)}(\boldsymbol{x}, \boldsymbol{x}') = \int & e^{i\omega[R_{ij}(\mathbf{x}',s)/c_0 + B_{ij}(\mathbf{x}',\mathbf{v}_h,s)/c_0 - R_{ij}(\mathbf{x},s)/c_0 - B_{ij}(\mathbf{x},\mathbf{v},s)/c_0]} \\ & \times A_{ij}(\omega, s, \boldsymbol{x}, \boldsymbol{v}) Q_{ij}^{\boldsymbol{v}_h}(\omega, s, \boldsymbol{x}')\, d\omega ds,\end{aligned} \tag{3.26}$$

where $L_{ij}^{(\boldsymbol{v},\boldsymbol{v}_h)}(\boldsymbol{x}, \boldsymbol{x}')$ is the point spread function of the imaging operator.

3.4.3 Analysis of the Point Spread Function

We analyze the PSF of the imaging operator $\mathcal{K}$ to understand the geometric fidelity of the reconstructed $\boldsymbol{v}_h$-radiance images. In particular, we want to determine if a visible edge or a point scatterer in the scene is located at the right position and orientation in the image. To address this question, we use microlocal analysis.

Let

$$\Phi_{ij}^{(\boldsymbol{v},\boldsymbol{v}_h)}(\omega, s, \mathbf{x}', \mathbf{x}) = \omega[R_{ij}(\mathbf{x}', s)/c_0 + B_{ij}(\mathbf{x}', \mathbf{v}_h, s)/c_0 - R_{ij}(\mathbf{x}, s)/c_0 - B_{ij}(\mathbf{x}, \mathbf{v}, s)/c_0] \tag{3.27}$$

denote the phase of the image fidelity operator $\mathcal{K}\mathcal{F}$. By the Hörmader-Sato theorem [66, 67], we conclude that the imaging operator $\mathcal{K}$ reconstructs the visible edges (scatters) located at $\mathbf{x}$ with velocity $\mathbf{v}$ to location $\mathbf{x}'$ with velocity $\boldsymbol{v}_h$ in the image satisfying the following conditions:

$$\partial_\omega \Phi_{ij}^{(\boldsymbol{v},\boldsymbol{v}_h)}(\omega, s, \mathbf{x}', \mathbf{x}) = 0 \tag{3.28}$$

$$\partial_s \Phi_{ij}^{(\boldsymbol{v},\boldsymbol{v}_h)}(\omega, s, \mathbf{x}', \mathbf{x}) = 0. \tag{3.29}$$

Alternatively, at image location $\mathbf{x}'$, $\mathcal{K}$ reconstructs the visible edges of the scene at locations $\mathbf{x}$ that satisfy the conditions in (3.28) and (3.29). These conditions yield the surfaces

$$R_{ij}(\mathbf{x}', s) + B_{ij}(\mathbf{x}', \mathbf{v}_h, s) = R_{ij}(\mathbf{x}, s) + B_{ij}(\mathbf{x}, \mathbf{v}, s) \tag{3.30}$$

$$\dot{R}_{ij}(\mathbf{x}', s) + \dot{B}_{ij}(\mathbf{x}', \mathbf{v}_h, s) = \dot{R}_{ij}(\mathbf{x}, s) + \dot{B}_{ij}(\mathbf{x}, \mathbf{v}, s), \tag{3.31}$$

where $\mathbf{x} = [\boldsymbol{x}, \psi(\boldsymbol{x})]$, $\mathbf{v} = [\boldsymbol{v}, \nabla_{\boldsymbol{x}}\psi(\boldsymbol{x}) \cdot \boldsymbol{v}]$, $[\boldsymbol{x}, \boldsymbol{v}, \boldsymbol{x}', \boldsymbol{v}_h] \in \operatorname{supp}\big(A_{ij} Q_{ij}^{\boldsymbol{v}_h}\big)$; and $\dot{R}_{ij}$ and $\dot{B}_{ij}$ are the derivatives with respect to s of R_{ij} and B_{ij}, respectively.

For a fixed $\mathbf{x}'$ and $\mathbf{v}_h$, (3.30) describes hitchhiker iso-range contours for moving targets. These contours satisfy the equation

$$R_{ij}(\mathbf{x}, s) + B_{ij}(\mathbf{x}, \mathbf{v}, s) = C_R \tag{3.32}$$

$$|\mathbf{x} - \boldsymbol{\gamma}_i(s)| - |\mathbf{x} - \boldsymbol{\gamma}_j(s)| + [(\widehat{\mathbf{x} - \boldsymbol{\gamma}_i(s)}) - (\widehat{\mathbf{x} - \boldsymbol{\gamma}_j(s)})] \cdot \mathbf{v}s = C_R, \quad (\boldsymbol{x}, \boldsymbol{v}) \in \operatorname{supp}\big(A_{ij}\big), \tag{3.33}$$

where C_R is a constant.

Similarly, for a fixed $\mathbf{x}'$ and $\mathbf{v}_h$, (3.31) describes a set in $(\mathbf{x}, \mathbf{v})$ satisfying

$$\partial_s R_{ij}(\mathbf{x}, s) + \partial_s B_{ij}(\mathbf{x}, \mathbf{v}, s) = C_D \tag{3.34}$$

$$\begin{aligned}&(\widehat{\mathbf{x} - \boldsymbol{\gamma}_i(s)}) \cdot (\mathbf{v} - \dot{\boldsymbol{\gamma}}_i(s)) - (\widehat{\mathbf{x} - \boldsymbol{\gamma}_j(s)}) \cdot (\mathbf{v} - \dot{\boldsymbol{\gamma}}_j(s)) \\ &\qquad - \frac{\dot{\boldsymbol{\gamma}}_i(s)s}{|\mathbf{x} - \boldsymbol{\gamma}_i(s)|} \cdot \mathbf{v}_i^{\perp} + \frac{\dot{\boldsymbol{\gamma}}_j(s)s}{|\mathbf{x} - \boldsymbol{\gamma}_j(s)|} \cdot \mathbf{v}_j^{\perp} = C_D, \quad (\boldsymbol{x}, \boldsymbol{v}) \in \operatorname{supp}\big(A_{ij}\big),\end{aligned} \tag{3.35}$$

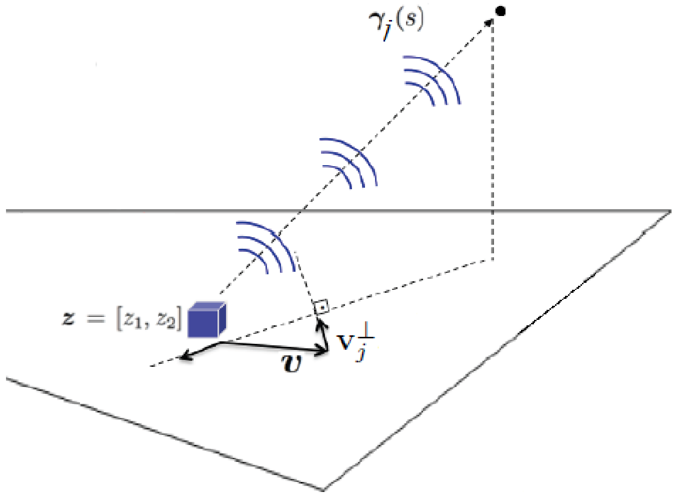

Figure 3.4: Geometry of the $\mathbf{v}_j^{\perp}$ vector, which is the target's velocity projected onto the direction perpendicular to the antenna look direction.

where C_D is a constant and

$$\mathbf{v}_i^{\perp} = \mathbf{v} - (\widehat{\mathbf{x} - \boldsymbol{\gamma}_i(s)})[(\widehat{\mathbf{x} - \boldsymbol{\gamma}_i(s)}) \cdot \mathbf{v}] \tag{3.36}$$

$$\mathbf{v}_j^{\perp} = \mathbf{v} - (\widehat{\mathbf{x} - \boldsymbol{\gamma}_j(s)})[(\widehat{\mathbf{x} - \boldsymbol{\gamma}_j(s)}) \cdot \mathbf{v}]. \tag{3.37}$$

The $\mathbf{v}_i^{\perp}$ and $\mathbf{v}_j^{\perp}$ vectors are the three-dimensional target velocities projected onto the direction perpendicular to the look directions of the two receivers. The equation describing the iso-Doppler contours is derived in Appendix A. Figure 3.4 shows the geometry of this vector.

We refer to the set $(\boldsymbol{x}, \boldsymbol{v})$ satisfying (3.35) as the *hitchhiker iso-Doppler contours for moving targets*. We define the cross-sections of this set for fixed velocity as the position-space hitchhiker iso-Doppler contours, and for fixed position as the velocity-space hitchhiker iso-Doppler contours.

The position space iso-range contours in (3.33), as described in Section 3.3.3, are the intersections of warped hyperboloids with the ground topography.

The imaging operator reconstructs visible edges at the intersection of hitchhiker iso-range and iso-Doppler contours. Since one of the solutions of (3.28) and (3.29) is $\mathbf{x} = \mathbf{x}'$ for $\mathbf{v}_{\mathbf{x}} = \mathbf{v}_h$, we conclude that the imaging operator puts the visible

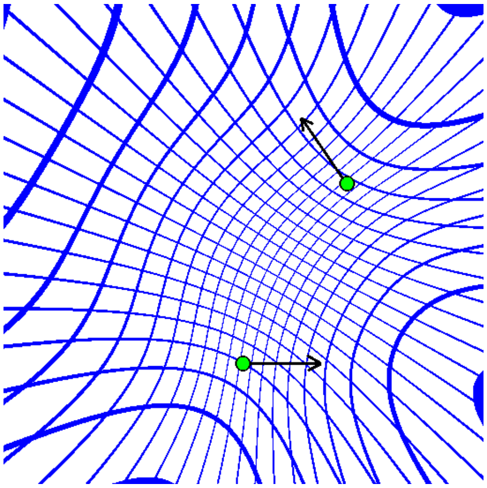

Figure 3.5: Intersection of the position space iso-range and iso-Doppler curves for flat topography. The green circles are the two receiving antennas, with their velocity vectors shown as arrows.

edges at the right location in the image. However, (3.28) and (3.29) may have additional solutions, resulting in artifacts in the reconstructed image. Some of these artifacts may be prevented by choosing an appropriate support for A_{ij} (illumination pattern) and appropriate flight trajectories for receivers. Figure 3.5 shows the intersection of the position space iso-range and iso-Doppler contours for particular antenna locations and antenna velocities indicated by solid dots and arrows. The figure suggests that in order to eliminate artifacts and ambiguities, the two receivers have to look at the same side of the scene with respect to the conjugate axis of the warped hyperbolas.

3.4.4 Determination of the FBP Filter

In the previous subsection, we showed that the imaging operator can reconstruct a position image of a scatterer at the correct location and orientation irrespective of the choice of the filter Q_{ij}, as long as the hypothesized velocity of a scatter is equal to its true velocity. In this section, we derive the filter such that the strength or contrast of the scatterer is also determined correctly. To do so, we choose the filter Q_{ij} such that the PSF of the imaging operator for each pair of receivers is approximately the Dirac delta function under the assumption that the hypothesized velocity $\mathbf{v}_h$ equals the true velocity $\boldsymbol{v}_{\mathbf{x}}$:

$$\begin{aligned} L_{ij}^{(\boldsymbol{v}_h,\boldsymbol{v}_h)}(\boldsymbol{x},\boldsymbol{x}') &\approx \delta(\boldsymbol{x}-\boldsymbol{x}') \\ &= \int e^{i(\boldsymbol{x}-\boldsymbol{x}')\cdot\boldsymbol{\xi}}\, d\boldsymbol{\xi}. \end{aligned} \tag{3.38}$$

To obtain the desired PSF given in (3.38) we make a Taylor series approximation of the phase around the point $\boldsymbol{x} = \boldsymbol{x}'$:

$$\Phi_{ij}^{(\boldsymbol{v}_h,\boldsymbol{v}_h)}(\omega, s, \mathbf{x}', \mathbf{x}) \approx (\boldsymbol{x}-\boldsymbol{x}')\frac{\omega}{c_0}\nabla_{\boldsymbol{x}}[-R_{ij}(\mathbf{x}, s) - B_{ij}(\mathbf{x}, \mathbf{v}_h, s)]|_{\boldsymbol{x}=\boldsymbol{x}'}. \tag{3.39}$$

Let

$$\Xi_{ij}(s, \boldsymbol{x}', \boldsymbol{v}_h) = \nabla_{\boldsymbol{x}}[-R_{ij}(\mathbf{x}, s) - B_{ij}(\mathbf{x}, \mathbf{v}_h, s)]|_{\boldsymbol{x}=\boldsymbol{x}'} \tag{3.40}$$

and

$$\boldsymbol{\xi}_{ij} = \frac{\omega}{c_0}\Xi_{ij}(s, \boldsymbol{x}', \boldsymbol{v}_h). \tag{3.41}$$

We now make the change of variables

$$(\omega, s) \to \boldsymbol{\xi}_{ij} = \frac{\omega}{c_0}\Xi_{ij}(s, \boldsymbol{x}', \boldsymbol{v}_h) \tag{3.42}$$

in the PSF to obtain

$$L_{ij}^{(\boldsymbol{v}_h,\boldsymbol{v}_h)}(\boldsymbol{x},\boldsymbol{x}') = \int_{\Omega_{ij}} e^{i(\boldsymbol{x}-\boldsymbol{x}')\cdot\boldsymbol{\xi}_{ij}} A_{ij}(\boldsymbol{\xi}_{ij}, \boldsymbol{x}', \boldsymbol{v}_h) Q_{ij}^{\boldsymbol{v}_h}(\boldsymbol{\xi}_{ij}, \boldsymbol{x}')\eta(\boldsymbol{\xi}_{ij}, \boldsymbol{x}', \boldsymbol{v}_h)\, d\boldsymbol{\xi}_{ij}, \tag{3.43}$$

where η is the determinant of the Jacobian that comes from the change of variables in (3.42),

$$\eta(\boldsymbol{\xi}_{ij}, \boldsymbol{x}', \boldsymbol{v}_h) = \left|\frac{\partial(\omega, s)}{\partial\boldsymbol{\xi}_{ij}}\right|, \tag{3.44}$$

and

$$\Omega_{ij} = \{\boldsymbol{\xi}_{ij} : \boldsymbol{\xi}_{ij} = \frac{\omega}{c_0}\boldsymbol{\Xi}_{ij}(s, \boldsymbol{x}', \boldsymbol{v}_h), A_{ij}(\boldsymbol{\xi}_{ij}, \boldsymbol{x}', \boldsymbol{v}_h) \neq 0\}. \tag{3.45}$$

In (3.43), for notational convenience, we redefine

$$A_{ij}(\boldsymbol{\xi}_{ij}, \boldsymbol{x}', \boldsymbol{v}_h) = A_{ij}(\omega(\boldsymbol{\xi}_{ij}), s(\boldsymbol{\xi}_{ij}), \boldsymbol{x}', \boldsymbol{v}_h) \tag{3.46}$$

$$Q_{ij}^{\boldsymbol{v}_h}(\boldsymbol{\xi}_{ij}, \boldsymbol{x}') = Q_{ij}^{\boldsymbol{v}_h}(\omega(\boldsymbol{\xi}_{ij}), s(\boldsymbol{\xi}_{ij}), \boldsymbol{x}'). \tag{3.47}$$

We refer to the set Ω_{ij} as the data collection manifold at $\boldsymbol{x}'$. Clearly, the vector $\boldsymbol{\xi}_{ij}$ can be interpreted as the Fourier vector that contributes to the reconstruction of a pixel at $\boldsymbol{x}'$. The set Ω_{ij} and the vector $\boldsymbol{\xi}_{ij}$ describes many of the properties of the reconstructed image as will be discussed in Part 2.

Since we desire our filter to make the PSF an approximate Dirac delta function, the optimal filter becomes

$$\begin{aligned} Q_{ij}^{\boldsymbol{v}_h}(\boldsymbol{\xi}_{ij}, \boldsymbol{x}', \boldsymbol{v}_h) &= \frac{\chi_\Omega A_{ij}^*(\boldsymbol{\xi}_{ij}, \boldsymbol{x}', \boldsymbol{v}_h)}{\eta(\boldsymbol{\xi}_{ij}, \boldsymbol{x}', \boldsymbol{v}_h)|A_{ij}(\boldsymbol{\xi}_{ij}, \boldsymbol{x}', \boldsymbol{v}_h)|^2} \\ &= \frac{\chi_\Omega A_{ij}^*(\boldsymbol{\xi}_{ij}, \boldsymbol{x}', \boldsymbol{v}_h)}{|A_{ij}(\boldsymbol{\xi}_{ij}, \boldsymbol{x}', \boldsymbol{v}_h)|^2}\frac{|\omega|}{c_0^2}|\Xi_{ij,1}\dot{\Xi}_{ij,2} - \Xi_{ij,2}\dot{\Xi}_{ij,1}|, \end{aligned} \tag{3.48}$$

where χ_Ω is a smooth cut-off function to prevent division by zero and $\boldsymbol{\Xi}_{ij} = [\boldsymbol{\Xi}_{ij,1}, \boldsymbol{\Xi}_{ij,2}]$.

The direction of the $\boldsymbol{\xi}_{ij}$ vector is defined by the vector $\boldsymbol{\Xi}_{ij}$ which is given by

$$\begin{aligned} \boldsymbol{\Xi}_{ij}(s, \boldsymbol{x}', \boldsymbol{v}_h) = &- D\psi(\boldsymbol{x}') \cdot [(\widehat{\mathbf{x}' - \boldsymbol{\gamma}_i(s)}) - (\widehat{\mathbf{x}' - \boldsymbol{\gamma}_j(s)})] \\ &- \frac{D\psi(\boldsymbol{x}') \cdot \mathbf{v}_{h,i}^{\perp} s + \partial_{\boldsymbol{x}'}^2 \psi(\boldsymbol{x}') \cdot \boldsymbol{v}_h(\psi(\boldsymbol{x}') - \boldsymbol{\gamma}_i^3(s))s}{|\mathbf{x}' - \boldsymbol{\gamma}_i(s)|} \\ &+ \frac{D\psi(\boldsymbol{x}') \cdot \mathbf{v}_{h,j}^{\perp} s + \partial_{\boldsymbol{x}'}^2 \psi(\boldsymbol{x}') \cdot \boldsymbol{v}_h(\psi(\boldsymbol{x}') - \boldsymbol{\gamma}_j^3(s))s}{|\mathbf{x}' - \boldsymbol{\gamma}_j(s)|}, \end{aligned} \tag{3.49}$$

where

$$D\psi(\boldsymbol{x}') = \begin{bmatrix} 1 & 0 & \partial\psi(\boldsymbol{x}')/\partial x'_1 \\ 0 & 1 & \partial\psi(\boldsymbol{x}')/\partial x'_2 \end{bmatrix} \tag{3.50}$$

$$\partial^2_{\boldsymbol{x}'} = \begin{bmatrix} \partial^2/\partial x'^2_1 & \partial^2/\partial x'_1 x'_2 \\ \partial^2/\partial x'_2 x'_1 & \partial^2/\partial x'^2_2 \end{bmatrix}, \tag{3.51}$$

and the matrix $D\psi(\boldsymbol{x}')$ projects a 3D vector onto the tangent plane of the ground topography, and the $\partial^2_{\boldsymbol{x}'}$ matrix is the Hessian operator. The derivation for the $\boldsymbol{\Xi}_{ij}$ vector can be found in Appendix B.

In the case of flat topography ($\psi(\boldsymbol{x}') = 0$), (3.49) reduces to

$$\boldsymbol{\Xi}_{ij}(s, \boldsymbol{x}', \boldsymbol{v}_h) = \boldsymbol{\Xi}_{ij,1}(s, \boldsymbol{x}', \boldsymbol{v}_h) + \boldsymbol{\Xi}_{ij,2}(s, \boldsymbol{x}', \boldsymbol{v}_h) \tag{3.52}$$

where

$$\boldsymbol{\Xi}_{ij,1}(s, \boldsymbol{x}', \boldsymbol{v}_h) = D\psi(\boldsymbol{x}') \cdot [(\widehat{\mathbf{x}' - \boldsymbol{\gamma}_j(s)}) - (\widehat{\mathbf{x}' - \boldsymbol{\gamma}_i(s)})] \tag{3.53}$$

$$\boldsymbol{\Xi}_{ij,2}(s, \boldsymbol{x}', \boldsymbol{v}_h) = \frac{D\psi(\boldsymbol{x}') \cdot \mathbf{v}^{\perp}_{h,j} s}{|\mathbf{x}' - \boldsymbol{\gamma}_j(s)|} - \frac{D\psi(\boldsymbol{x}') \cdot \mathbf{v}^{\perp}_{h,i} s}{|\mathbf{x}' - \boldsymbol{\gamma}_i(s)|}. \tag{3.54}$$

Figure 3.6 shows the two components of the $\boldsymbol{\Xi}_{ij}$ vector. The first component, portrayed on the left, is a function of the antenna locations and imaging geometry. This term remains the same as in the stationary case derived in [41]. The second term, shown on the right, is due to the movement of the targets.

The filter $\boldsymbol{\Xi}_{ij}(s, \boldsymbol{x}', \boldsymbol{v}_h)$ depends on A_{ij} and therefore both $R_T(\omega, \boldsymbol{x})$ and the transmitter-related geometric spreading term. When this information is unavailable, we can assume a uniform prior on R_T, corresponding to a white noise model for the ambient electromagnetic signal, and we can approximate the geometric spreading up to the radius of the imaging region of interest assuming the transmitter lies outside of this region. Since we are performing the imaging coherently, i.e. by matching the phase of the forward operator with the imaging operator, which does not include any of the terms above, the Jacobian resulting from the change of variables in the phase (3.42) plays a more significant role in obtaining the correct strengths of the

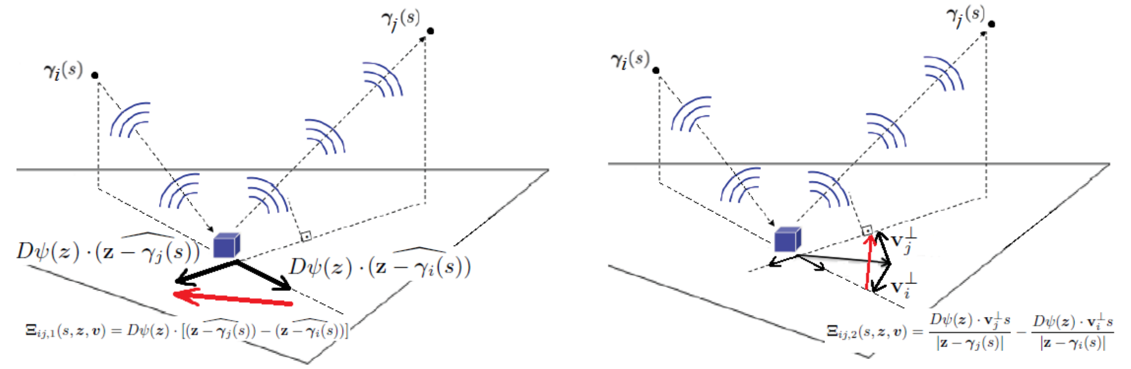

Figure 3.6: The two components of the Ξ_{ij} vector. $\Xi_{ij,1}$ is shown on the left and is due to the antenna look directions, and $\Xi_{ij,2}$, due to the $\mathbf{v}^\perp$ vectors, is shown on the right.

scatterers than the other terms involved in the filter. In addition, the scatterers will also be correctly positioned in the reconstruction image, since this is a function only of the phase matching procedure.

3.4.5 Velocity Estimation

To estimate the velocities of targets, we reconstruct a series of radiance images, each using a fixed hypothesized velocity for a range of velocities. Images that are reconstructed with an incorrect hypothesized velocity have smeared targets, while the image with the correct velocity will have a focused target. We present an analysis of the degree and nature of smearing in reconstructed images due to incorrect velocity in the next chapter.

There are a variety of metrics to measure the degree of focus in SAR images [6], [7], [57]-[62]. See [61] for a review of these metrics. We chose Shannon entropy as a measure of focus for each reconstructed image. Entropy provides distinct benefits for SAR, which includes being a sensitive measure of image focus quality, having a smooth dependence on autofocus parameters, and requiring no specific target or clutter model [59]. In general, one may choose to compute the image entropy over an energy-weighted version of the image as

$$g^{\boldsymbol{v}_h}(\boldsymbol{x}') = w(\boldsymbol{x}')\hat{r}^{\boldsymbol{v}_h}(\boldsymbol{x}'), \tag{3.55}$$

where $w(\boldsymbol{x}')$ is a two-dimensional weighting function as described in [60]. To use the original image, $w(\boldsymbol{x}')$ can simply be set to 1 for all $\boldsymbol{x}'$. To use a patch of the original image, $w(\boldsymbol{x}')$ can be set to 1 on the patch and zero outside. For various other choices of "energy" weighting, see [61].

We measure the degree of focus of each image, and we presume the images with the highest focus yield the correct velocity estimates. For a given radiance image reconstructed using the hypothesized velocity $\boldsymbol{v}_h$, its entropy is defined as

$$\mathrm{En}(\boldsymbol{v}_h) = -\int p(g^{\boldsymbol{v}_h}(\boldsymbol{x}')) \log[p(g^{\boldsymbol{v}_h}(\boldsymbol{x}'))] d\boldsymbol{x}', \tag{3.56}$$

where p is the probability density function or the normalized histogram of the image in the discrete case. As the error between true and hypothesized velocity of moving targets increases, the smearing artifacts increase, resulting in higher computed entropy values. Thus, the local minima of En correspond to the estimated target velocities.

If the number of moving targets in the scene is known prior to velocity estimation, then this number of minimum entropy images can simply be chosen from the image stack. If this quantity is unknown, however, then a criterion, such as constant false alarm rate, can be used to determine the number of moving targets in the scene[68]. The images reconstructed with the hypothesized velocities corresponding to the lowest entropy values then each display a focused (or nearly focused, considering the effects of noise and clutter) target moving with that particular velocity.

3.5 Computational Complexity Analysis

This section describes the algorithmic implementation of our method and analyze its computational complexity.

Our image reconstruction formula for a hypothesized velocity is presented in (3.23). After performing the $d\tau$ integration, the formula becomes

$$\begin{aligned} \hat{r}^{\boldsymbol{v}_h}(\boldsymbol{x}') = \sum_{i,j} \int & e^{-i\omega[-R_{ij}(\mathbf{x}',s)/c_0 - B_{ij}(\mathbf{x}',\mathbf{v}_h,s)/c_0]} \\ & \times D_{ij}(s,\omega) Q_{ij}^{\boldsymbol{v}_h}(\omega, s, \boldsymbol{x}')\, d\omega ds \end{aligned} \tag{3.57}$$

where $D_{ij}(s,\omega)$ is the Fourier transform of $d_{ij}(s,\tau)$ in the τ direction. Furthermore, the filter Q_{ij} can be decomposed as

$$Q_{ij}^{\boldsymbol{v}_h}(\omega,s,\boldsymbol{x}') = Q_{ij}^{\boldsymbol{v}_h,1}(s,\boldsymbol{x}')Q_{ij}^{\boldsymbol{v}_h,2}(\omega,s,\boldsymbol{x}')|\omega| \tag{3.58}$$

where

$$Q_{ij}^{\boldsymbol{v}_h,1}(s,\boldsymbol{x}') = |\Xi_{ij,1}\dot{\Xi}_{ij,2} - \Xi_{ij,2}\dot{\Xi}_{ij,1}| \tag{3.59}$$

$$Q_{ij}^{\boldsymbol{v}_h,2}(\omega,s,\boldsymbol{x}') = \frac{\chi_\Omega A_{ij}^*(\omega,s,\boldsymbol{x}',\boldsymbol{v}_h)}{|A_{ij}(\omega,s,\boldsymbol{x}',\boldsymbol{v}_h)|^2 c_0^2}. \tag{3.60}$$

Here, the $|\omega|$ factor is the well-known ramp filter from the tomography literature, the $Q_{ij}^{\boldsymbol{v}_h,1}$ filter compensates for the change of variables, and the $Q_{ij}^{\boldsymbol{v}_h,2}$ filter reverses the effects of the amplitude factor, which includes the beam pattern, waveform, and geometric spreading factors.

Assuming $\mathcal{O}(N)$ samples in both fast-time and slow-time and a scene sampled at $\mathcal{O}(N \times N)$ points, the image reconstruction procedure for a hypothesized velocity $\mathbf{v}_h$ can be implemented as follows:

1. *Correlating each pair of receiver data in fast-time:* The received signals for each pair of antennas are cross-correlated using (3.6) at each slow-time s. Therefore, for all s, the computational complexity of this step is $\mathcal{O}(N^2)$.

2. *Computing the Fourier transform in fast-time:* For each s the Fourier transform of $d_{ij}(s,\tau)$ can be computed in $\mathcal{O}(N\log N)$ computations, so for all s, this step has a computational complexity of $\mathcal{O}(N^2\log N)$. Note that if FFT-based cross-correlation is used in Step 1, these first two steps can be combined.

3. *Ramp filtering:* Let

$$\tilde{D}_{ij}(s,\omega) = |\omega| D_{ij}(s,\omega). \tag{3.61}$$

   For each s, this filtering can be computed in $\mathcal{O}(N)$ computations, making the computational complexity of this step $\mathcal{O}(N^2)$.

4. *Filtering with $Q_{ij}^{\boldsymbol{v}_h,2}$:* Let

$$\tilde{D}_{ij,Q_{ij}^{\boldsymbol{v}_h,2}}(s,\omega,\boldsymbol{x}') = \tilde{D}_{ij}(s,\omega) Q_{ij}^{\boldsymbol{v}_h,2}(\omega,s,\boldsymbol{x}'). \tag{3.62}$$

   For each s and $\boldsymbol{x}'$, this filtering can be performed in $\mathcal{O}(N)$ computations, so the computational complexity of this step is $\mathcal{O}(N^4)$ in general. If $Q_{ij}^{\boldsymbol{v}_h,2}$ is independent of $\boldsymbol{x}'$ however, this step reduces to $\mathcal{O}(N^2)$.

5. *Backprojection:* Let

$$\hat{r}_{ij,Q_{ij}^{\boldsymbol{v}_h,2}}(\boldsymbol{x}',s) = \int e^{-i\omega[-R_{ij}(\mathbf{x}',s)/c_0 - B_{ij}(\mathbf{x}',\mathbf{v}_h,s)/c_0]} \tilde{D}_{ij,Q_{ij}^{\boldsymbol{v}_h,2}}(s,\omega,\boldsymbol{x}')\, d\omega. \tag{3.63}$$

   For each s and $\boldsymbol{x}'$, (3.63) can be computed in $\mathcal{O}(N)$ computations. Thus, for all s and $\boldsymbol{x}'$, the computational complexity of this step is $\mathcal{O}(N^4)$.

6. *Partial image formation:* We form the partial image using

$$\hat{r}_{ij}^{\boldsymbol{v}_h}(\boldsymbol{x}') = \int Q_{ij}^{\boldsymbol{v}_h,1}(s,\boldsymbol{x}',\boldsymbol{v}_h) \hat{r}_{ij,Q_{ij}^{\boldsymbol{v}_h,2}}(\boldsymbol{x}',s)\, ds. \tag{3.64}$$

   For each point $\boldsymbol{x}'$ this integral can be computed in $\mathcal{O}(N)$, so the computational complexity of this step is $\mathcal{O}(N^3)$.

7. *Complete image formation:* We form our final image via

$$\hat{r}^{\boldsymbol{v}_h}(\boldsymbol{x}') = \sum_{i,j} \hat{r}_{ij}^{\boldsymbol{v}_h}(\boldsymbol{x}'). \tag{3.65}$$

   Assuming the number of receiver pairs is much less than N, the overall computational complexity of complete image formation is equal to the highest computational complexity of each of the steps. Therefore, the overall complexity for image formation is $\mathcal{O}(N^4)$. Note that for the case of a large number of receiver pairs, the complexity of this step will scale linearly with the number of receiver pairs.

8. *Entropy calculation:* Compute $\mathrm{En}(\boldsymbol{v}_h)$ by calculating the entropy for each

image in the stack with the formula

$$\mathrm{En}(\boldsymbol{v}_h) = -\sum_{\boldsymbol{x}'} p(\hat{r}^{\boldsymbol{v}_h}(\boldsymbol{x}')) \log[p(\hat{r}^{\boldsymbol{v}_h}(\boldsymbol{x}'))]. \tag{3.66}$$

The computational complexity of the entropy calculation will be $\mathcal{O}(N^2)$ for each of the histogram calculation, logarithm computation, and summation, yielding a complexity of $\mathcal{O}(N^2)$ for the overall step.

The computational complexity of the full image formation procedure will be that of the step with the highest complexity, which in the above form is dominated by the filtering and backprojection steps of $\mathcal{O}(N^4)$. The backprojection method described above is a Fourier-based technique. This can instead be implemented efficiently by using fast backprojection algorithms [69]-[71] or fast Fourier integral operator computation methods [72], [73], [63]. For example, with the fast Fourier integral operator computation method presented in [63], the filtered backprojection step can be performed with a computational complexity of $\mathcal{O}(N^2 \log N)$.

This image formation processes is repeated for each hypothesized velocity, and the images with the lowest entropy values are then chosen. Assuming $\mathcal{O}(M)$ hypothesized velocities, the full image reconstruction and velocity estimation procedure will have a computational complexity of $\mathcal{O}(MN^4)$, or of $\mathcal{O}(MN^2 \log N)$ if the fast Fourier integral operator algorithm mentioned above is used. However, if we assume that $M \ll N$, the full image reconstruction and velocity computational complexity reduces to the complexity of the single image formation procedure.

3.6 Numerical Simulations

3.6.1 Simulation Setup

This section describes the numerical simulations that were performed in order to demonstrate the algorithm and its performance. In the next chapter, we perform simulations to demonstrate properties relating to resolution and position error. We simulate a moving scene of size 512 × 512 meters that is discretized into 128 × 128 pixels, so that each pixel represents 4 square meters. The receiving antennas move in a circular aperture at a tangential velocity of 261 m/s. The circular aperture has a radius of 1.5 km, an altitude of 1 km, and is discretized into 2048 equally spaced samples.

Note that the assumption of targets having linear motion while the antennas are traversing a circular aperture may not be valid. However, this particular configuration was chosen so that velocity estimation-related effects can be deconvolved from potential limited-aperture artifacts.

The transmitter is a stationary tower located outside the circular flight trajectory at a distance of about 2.1 km from the center of the scene. The transmitter is using a rectangular pulse with an effective bandwidth of about 8 MHz. This is similar to the higher bandwidths used by sources of opportunity such as DVB-T and WiMax[15]. A graphical illustration of this setup is shown in Figure 3.7.

The velocities of the targets were varied to demonstrate the performance of the algorithm. The moving targets were simulated with speeds in the range of about 10 to 30 m/s, which is aligned with a range of normal vehicle speeds. For the hypothesized velocity, the speeds of the moving targets were assumed to be between 0 and 45 m/s. Therefore, the two-dimensional hypothesized velocity was varied from -45 to 45 m/s in each dimension with a step size of 2.25 m/s.

The data was generated by stepping through each slow-time and summing the signals scattered from each moving target in the scene. The velocity estimation and image reconstruction steps were then performed as described in Section 3.5. Note that the image reconstruction and velocity estimation procedure is based on the forward model, which is only an approximation to the method by which the data is collected. Additionally, as described in Section 3.4-D, we used an uninformative prior for the second-order statistics of the antenna beam patterns as well as constant geometric spreading factors in the image reconstruction.

3.6.2 Single Moving Target

The first simulation of our method shows a basic test case of a single target moving at a slower velocity of about 9 m/s towards the right. The scene at the initial time of $s = 0$ is shown in Figure 3.8. We refer to this setup as Scene 1. Figure 3.8 also shows the reconstructed image when a hypothesized velocity of zero is used.

This incorrect velocity assumption produces a smeared target in the reconstructed image, since echoes are received from multiple locations across the scene over the length of the aperture. Figure 3.9 shows a part of the entropy image over the range of hypothesized velocities from -20 m/s to 20 m/s. The minimum point in this entropy image corresponds to the true velocity. Finally, the image is reconstructed using the estimated true velocity, obtained from finding the minimum entropy point in the entropy image. This image is shown on the right in Figure 3.9, and displays the ideal result of perfect reconstruction with no error.

The second simulation uses a single moving target in the same starting location as the first simulation and moving towards the bottom right of the image with a much greater velocity of about [18.1, 18.1] m/s. In this situation, additional receivers were added to limit the amount of time necessary to collect the required data. We refer to this setup as Scene 2. Figure 3.10 on the left shows the plot of the entropy for hypothesized velocities of -50 m/s to 50 m/s in each direction of velocity. This plot shows a clear minimum entropy point at the true velocity of [18.1, 18.1] m/s. The reconstructed image is shown on the right side of this figure, which shows similar results to the first case.

3.6.3 Multiple Moving Targets

The third simulation demonstrates the algorithm's performance for a scene with multiple targets. The original scene for this simulation is shown on the left in Figure 3.11. There are two moving targets, one in the top left moving to the right at a velocity of 9 m/s and one in the bottom right moving towards the top left of the image traveling at about 12.8 m/s. In addition, there are two stationary targets; one is located just to the top right of the center of the scene and the other in the bottom left. We refer to this setup Scene 3. Figure 3.11 on the right shows the entropy for Scene 3. The three minimum points on the surface correspond to the true velocity of each of the two moving targets as well as the zero velocity. Figure 3.12 shows two of the reconstructed images corresponding to the velocity of the first target and the zero velocity, respectively. Figure 3.13 on the left shows the third hypothesized velocity reconstruction, which corresponds to the second moving target in the bottom right of the image. Accurate position reconstruction is obtained; however, with the multiple target case, we can see artifacts in each of the images resulting from the blurring of the incorrect targets. The method still reconstructs the true target at a much higher strength than the artifacts, however. Figure 3.13 on the right shows the cross-section of the horizontal row of the image containing the true target located in the bottom right corner. Here we can see that the amplitude of the target is much larger than the rest of the scene. To compare with the amplitude of a blurring artifact, a plot of the row containing the top right stationary target is shown in Figure 3.14. The maximum amplitude shown here is just under 0.5, which is about half of the amplitude of the focused target. Note that weak targets could be masked by stronger targets. However, for this to occur, the strong and weak targets must be close in position, and the smearing artifacts of the strong target must be in the direction of the weaker target.

3.6.4 Multiple Moving Targets Embedded in Clutter

Finally, in the fourth simulation we investigate the effects of clutter on the performance of the algorithm. We simulate a moving target in the top left of the scene moving towards the right at about 9 m/s. Clutter was added to the scene by using a Rayleigh distribution for the clutter amplitude as described in [74]. Although neither the forward model nor the image reconstruction method attempt to model or suppress clutter, we obtain acceptable results with a high enough Signal-to-Clutter Ratio (SCR). To test the sensitivity of velocity estimation, the peak SCR (the ratio between target strength and clutter strength) was varied from 0 to 36 dB with steps of 2 dB. A plot of velocity root-mean-square error versus SCR is shown in Figure 3.15. This plot portrays accurate estimation at higher SCR levels, but there is a decline in performance at around 18 dB. Until this point, we see a graceful degradation of performance, indicating a degree of robustness of method with respect to clutter. Below this SCR level, the clutter becomes too dominant for the algorithm to estimate the target velocity. The curve then flattens out again because of the natural upper bound set by the velocity search grid, since we use a finite range of hypothesized velocities.

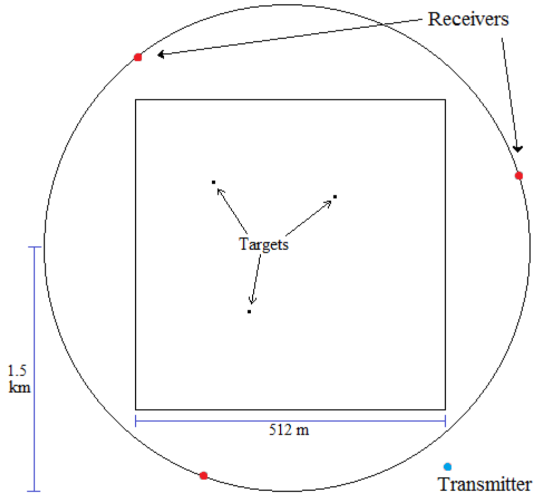

Figure 3.7: Setup for the simulations. The receivers move in a circular trajectory with a radius of 11 km, while the transmitter is stationary outside of the scene. The scene size is $[256 \times 256]$ m.

3.7 Conclusion

This chapter presents a method for image reconstruction and velocity estimation of a scene with moving targets using a network of passive receivers and non-cooperative sources of opportunity. Passive radar systems are an attractive solution because of their inherent cost, simplicity, and stealth advantages. Systems that are free of transmitters are cheaper to implement and harder to detect, which potentially increases the system's longevity. In addition, the problem of imaging moving targets is important to address, since targets of interest are often mobile, and without special processing they appear smeared and unfocused in the reconstructed image.

This chapter introduces a novel forward model and an FBP-type inversion method for passive imaging of a moving scene. The forward model is based on the correlation of received signals from different receivers and includes a phase term due to moving target displacement. We defined a backprojection operator and showed that if the true velocities of targets are used, our backprojection operator focuses the targets in the reconstructed radiance images. We then used a range of hypothesized

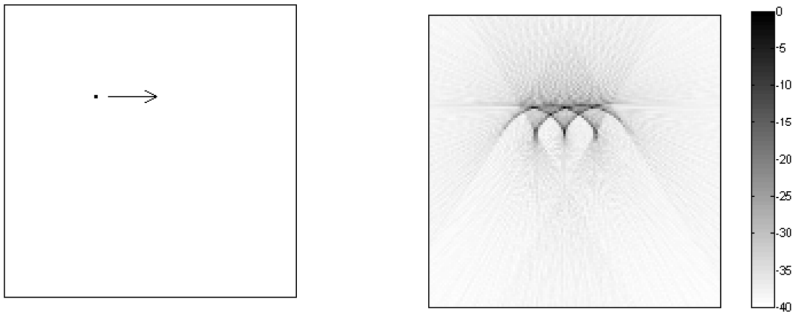

Figure 3.8: **Original setup of Scene 1 on the left along with the reconstruction on the right under the assumption of zero velocity. There is one moving target located in the upper left quadrant traveling towards the right at 1 m/s.**

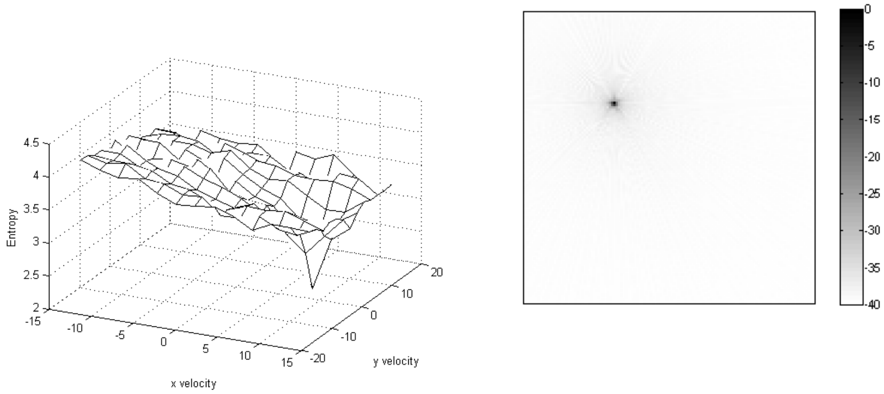

Figure 3.9: **The left figure shows the entropy associated with Scene 1 plotted as a function of hypothesized velocity. The minimum point (the darkest pixel) is at the correct target velocity, that is [1, 0] m/s. The image reconstruction corresponding to this hypothesized velocity is shown on the right.**

velocities and reconstructed a stack of radiance images, each one corresponding to a hypothesized velocity. We used entropy as a metric to measure the degree of focus in reconstructed images. The minimum entropy analysis yields the velocity estimate for each target as well as its corresponding image.

Our method relies on repeated use of backprojection operator which can be implemented efficiently by using fast backprojection algorithms or fast Fourier integral operator computation methods and by utilizing parallel processing on graphics processing units.

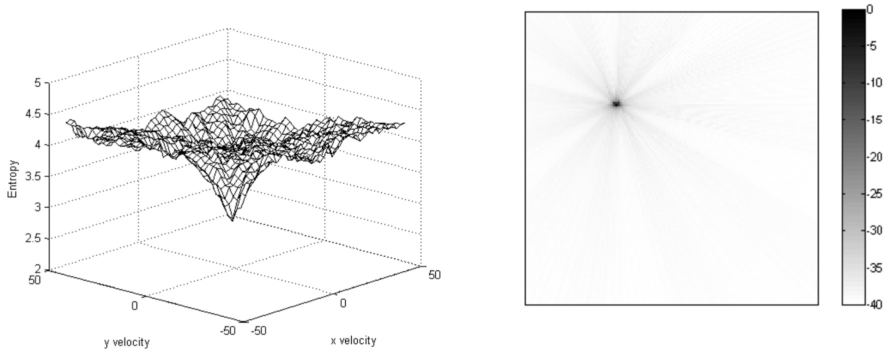

Figure 3.10: The left figure shows the entropy associated with Scene 2 plotted as a function of the hypothesized velocity over the full range of -50 m/s to 50 m/s in each direction. The minimum point is at [18.1, -18.1] m/s, the velocity of the moving target. The right figure shows the reconstructed image for Scene 2 with the hypothesized velocity for set to the estimated velocity vector of [18.1, -18.1] from minimum entropy.

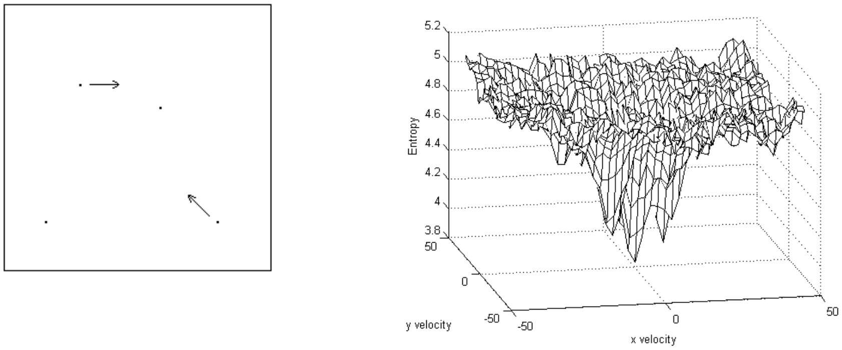

Figure 3.11: Scene 3 is shown on the left. There are two moving targets, one located in the upper left quadrant moving towards the right at velocity 9 m/s and one in the lower right quadrant moving towards the top left at velocity of about 12.8 m/s. There are also two stationary targets, one to the top right of the center of the scene and one in the bottom left. The right figure shows the entropy image associated with Scene 3. The minimum points of the image correspond to the true velocity of each of the moving targets as well as the zero velocity.

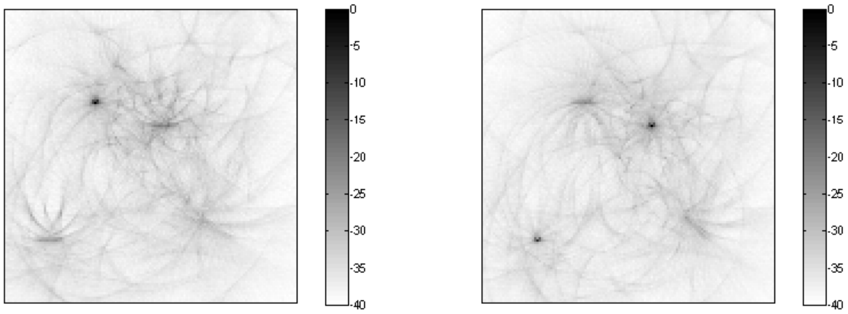

Figure 3.12: The reconstructed images for Scene 3 with the hypothesized velocity set to each of two of the three minimum points on the velocity image, the [9, 0] and [0, 0] velocities, respectively. Each image shows the focused target corresponding to the hypothesized velocity.

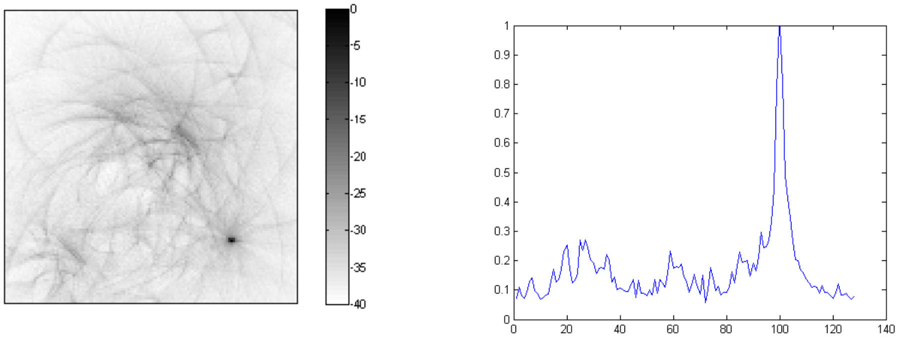

Figure 3.13: The left figure shows the reconstruction for the third minimum point in the entropy image with a hypothesized velocity of [-9, 9] m/s. Shown on the right is the horizontal cross-section of this reconstruction along the row containing the moving target. One can see here that the target still stands out above the blurring artifacts from the other moving targets.

We performed numerical simulations to demonstrate the viability of our method for single and multiple moving target scenarios. While our method does not explicitly consider clutter, our simulation study shows that entropy is a robust metric for estimating velocity at relatively low SCR levels. Additionally, since our image reconstruction method is backprojection-based, the image formation method holds in the presence of additive measurement noise under the assumption that the noise

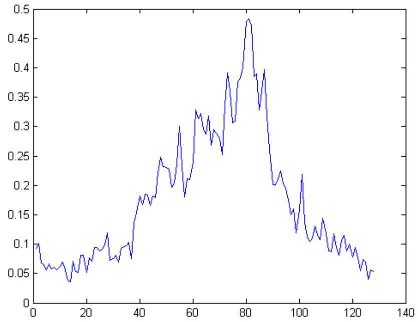

Figure 3.14: A plot of the top right stationary target in the third reconstructed image, focused for the bottom right moving target. The maximum amplitude shown here is just under 0.5, which is about half of the amplitude of the focused target.

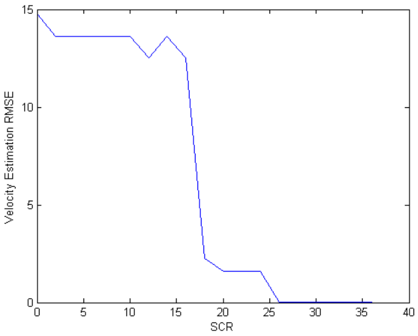

Figure 3.15: This plot shows the resulting RMSE for velocity estimation at various levels of SCRs. At higher SCR levels we still obtain accurate velocity estimation with a steady decline in performance as SCR is reduced.

is uncorrelated from one receiver to another [75]. When the noise and clutter are correlated, the results can be further improved by taking into account the statistics of the noise and clutter as in [76].

In this work we assumed that all targets were isotropic scatterers. However, when a wide enough aperture angle is used, this assumption is no longer valid, and one may wish to extend the model to account for anisotropic scatterers. This can be done by creating small subapertures defined by a small error in the Fourier vector, so that the isotropic assumption is valid for each subaperture. This technique is described in more detail in [77].

This technique is designed for imaging moving targets located on the ground, but the technique can be extended to image airborne targets in a straightforward manner. In that case, however, the number of unknowns would increase, both in position and velocity. As a result, the two-dimensional position-velocity ambiguities (as described in the next chapter) would extend to three-dimensional ambiguities. Additionally, the computational complexity would significantly increase.

In the next chapter, we analyze the performance of our method. We present position (radiance) and velocity resolution analysis and introduce a theory to analyze and predict smearing artifacts in the reconstructed radiance images due to incorrect velocity information.

CHAPTER 4

Passive Synthetic Aperture Hitchhiker Imaging of Ground Moving Targets - Performance Analysis

4.1 Introduction

In recent years, there has been growing interest in passive radar due to ever increasing radio frequency (RF) sources of opportunity, such as cell phone, TV, and radio broadcasting stations [24], [26]-[28], [36], [37], [39], [41]-[43], [45]. Additionally, passive radar systems are an attractive solution because of their inherent cost, simplicity, and stealth advantages. The problem of passive synthetic aperture imaging of moving targets is important, since targets of interest are often mobile. In the previous chapter, we introduce a method of passive imaging of ground moving targets using a network of airborne receivers and non-cooperative transmitters of opportunity. In this chapter, we derive and analyze the performance of the imaging method that was introduced. We present a resolution analysis on position and velocity and introduce a theory to analyze and predict smearing artifacts in the reconstructed position images due to incorrect velocity information. The investigation of achievable position and velocity resolution and error in target positioning due to velocity errors are important in designing and optimizing passive SAR imaging systems.

In the previous chapter, we present a novel forward model and an FBP-type image reconstruction combined with entropy optimization to reconstruct the radiance (position) images and to estimate two-dimensional velocities of ground targets. The forward model is based on the correlation of the received signals from multiple moving receivers. We design a backprojection operator and analyze its point spread function. The analysis shows that when the velocity of a scatterer/target is correctly estimated, the backprojection puts the target at the correct position and orientation in the image. The filter is designed to get the strength of targets correctly. We reconstruct a stack of radiance images, each corresponding to a fixed, hypothesized

---

This chapter is to appear in: S. Wacks and B. Yazici, "Passive synthetic aperture hitchhiker imaging of ground moving targets - part 2: Performance analysis," *IEEE Trans. Image Process.*.

velocity for a range of velocities. We analyze this stack of images using entropy as a measure of focus in order to estimate target velocities. The method is capable of imaging and estimating the velocities of multiple moving targets. While the method does not explicitly consider clutter, numerical simulations show that the entropy is a robust metric in estimating target velocities in relatively low signal-to-clutter ratios.

In this chapter, we examine the performance of the algorithm in two ways. First, we analyze the resolution of both target position and velocity estimation by looking at the bandwidth of range and spatial Doppler, respectively, available in the correlated data. Our analysis identifies several parameters related to transmitted waveforms and imaging geometry that contribute to position and velocity resolution. Next, we introduce a theory to analyze and predict smearing artifacts that appear in reconstructed radiance images due to the use of an incorrect hypothesized velocity in backprojection. The theory describes how velocity errors translate into positioning errors and the coupling between accurate target positioning and velocity estimation. We derive an analytic formula that relates the positioning errors/smearing caused by moving targets in images reconstructed using erroneous velocity information. This formula can be used for multiple purposes, both for the analysis and prediction of position errors arising from incorrectly hypothesized velocities, and understanding smearing artifacts in position images due to moving targets reconstructed under stationary scene assumption. Specifically, we also show that small errors in the velocity estimates results in small positioning errors in the reconstructed radiance images. Finally, we present extensive numerical simulations to demonstrate the performance of our method and to validate the theoretical results.

Section 4.2 reviews the forward model, image reconstruction, and velocity estimation algorithms from the previous chapter. Section 4.3 analyzes the position (radiance) resolution of the image reconstruction, assuming our hypothesized velocity is equal to the true velocity of the moving scene. Then, the velocity resolution is investigated by analyzing the potential velocity bandwidth available in the data. Section 4.4 removes the assumption of a correctly hypothesized velocity and instead analyzes the nature of errors in target positioning due to an incorrect velocity. We present a theory and an analytic formula to show how the position and velocity errors are coupled. Numerical simulations are then presented in Section 4.5. Finally, the chapter is concluded in Section 4.6.

4.2 Overview

This section briefly summarizes the forward model, radiance image reconstruction and velocity estimation methods described in the previous chapter to establish notation.

4.2.1 Forward Model

In radar signal processing, a target is typically an object of interest in a scene that is being imaged. The term clutter is used for scattering objects that are not of interest. Note that we use the term scatterer for point targets. Thus, targets can be a composed of a single or multiple scatterers.

We denote the location of the scatters on the ground by $\mathbf{x} = [\boldsymbol{x}, \psi(\boldsymbol{x})] \in \mathbb{R}^3$, where $\boldsymbol{x} = [x_1,\ x_2] \in \mathbb{R}^2$ and ψ is a known, smooth function for ground topography, i.e., $x_3 = \psi(\boldsymbol{x})$. Since the targets are moving on the ground, the three-dimensional velocity $\mathbf{v}_\mathbf{x}$ of a moving scatterer located at $\mathbf{x}$ at some reference time is given by $\mathbf{v}_\mathbf{x} = [\boldsymbol{v}_{\boldsymbol{x}}, \nabla_{\boldsymbol{x}}\psi(\boldsymbol{x}) \cdot \boldsymbol{v}_{\boldsymbol{x}}]$ where $\nabla_{\boldsymbol{x}}\psi(\boldsymbol{x})$ is the gradient of the ground topography.

We assume that there are N airborne receivers traversing trajectories $\boldsymbol{\gamma}_i$, $i = 1, ..., N$ and a single transmitter of opportunity located at $\mathbf{y}$. Under the assumption that the range variation due to targets and receivers' movement within one pulse transmission and reception is negligible [78], the received signal can be modeled as

$$\begin{aligned} f_i(s,t) = \int & \mathrm{e}^{-\mathrm{i}\omega[t-(|\mathbf{x}-\boldsymbol{\gamma}_i(s)|+|\mathbf{x}-\mathbf{y}|)/c_0-((\widehat{\mathbf{x}-\boldsymbol{\gamma}_i(s)})+(\widehat{\mathbf{x}-\mathbf{y}}))\cdot\mathbf{v}_\mathbf{x} s/c_0]} \\ & \rho(\boldsymbol{x}) A_i(\omega, s, \boldsymbol{x}, \boldsymbol{v})\, d\omega d\boldsymbol{x}, \end{aligned} \tag{4.1}$$

where s denotes the slow-time or synthetic aperture sampling interval, t denotes fast-time, A_i is a slow-varying function of frequency ω that depends on the transmitted waveform and geometric spreading factors, and ρ is the two-dimensional ground reflectivity function at the beginning of the synthetic aperture $s = 0$.

We next cross-correlate the received signals f_i, $i = 1, ..., N$ from different receivers and arrive at the forward model

$$\begin{aligned} d_{ij}(s,\tau) &= \mathcal{F}[r](s,\tau), \quad i,j = 1,...,N, \quad i \neq j \\ &= \int e^{-i\omega[\tau - R_{ij}(\mathbf{x},s)/c_0 - B_{ij}(\mathbf{x},\mathbf{v},s)/c_0]} A_{ij}(\omega,s,\boldsymbol{x},\boldsymbol{v}) r(\boldsymbol{x},\boldsymbol{v})\, d\boldsymbol{v} d\boldsymbol{x} d\omega, \end{aligned} \tag{4.2}$$

where d_{ij} denotes the cross-correlated received signal from the ith and jth receivers and τ denotes *hitchhiker fast-time*, and

$$A_{ij}(\omega,s,\boldsymbol{x},\boldsymbol{v}) = A_{R_{ij}}(\omega,s,\boldsymbol{x},\boldsymbol{v}) \frac{R_T(\omega,\boldsymbol{x})}{(4\pi)^2|\mathbf{x}+\mathbf{v}_{\mathbf{x}}s-\mathbf{y}|^2}, \tag{4.3}$$

$$R_{ij}(\mathbf{x},s) = |\mathbf{x}-\boldsymbol{\gamma}_i(s)| - |\mathbf{x}-\boldsymbol{\gamma}_j(s)|, \tag{4.4}$$

$$B_{ij}(\mathbf{x},s) = [(\widehat{\mathbf{x}-\boldsymbol{\gamma}_i(s)}) - (\widehat{\mathbf{x}-\boldsymbol{\gamma}_j(s)})] \cdot \mathbf{v}s, \tag{4.5}$$

where $\widehat{\mathbf{x}}$ denotes the unit vector in the direction of $\mathbf{x}$.

A_{ij} is a slow-varying function of ω satisfying the assumption (17) in [79]. $r(\boldsymbol{x},\boldsymbol{v})$ is the phase-space radiance function defined by $r(\boldsymbol{x},\boldsymbol{v}) \approx R_\rho(\boldsymbol{x})\varphi(\boldsymbol{v},\boldsymbol{v}_{\mathbf{x}})$ where R_ρ is the 2D scene radiance and $\varphi(\boldsymbol{v},\boldsymbol{v}_x)$ is a smooth function of $\boldsymbol{v}$ that approximates $\delta(\boldsymbol{v}-\boldsymbol{v}_{\mathbf{x}})$.

Let

$$\varphi_{ij}(\mathbf{x},\mathbf{v},s) = R_{ij}(\mathbf{x},s) + B_{ij}(\mathbf{x},\mathbf{v},s). \tag{4.6}$$

Then, the phase of $\mathcal{F}$ is

$$\omega[\tau - \frac{1}{c_0}\varphi_{ij}(\mathbf{x},\mathbf{v},s)] \tag{4.7}$$

and its amplitude is A_{ij}.

4.2.2 Image Formation

For a given hypothesized velocity $\boldsymbol{v}_h$, we form a position image via the following filtered backprojection operator:

$$\begin{aligned}\mathcal{K}[d_{ij}](\boldsymbol{x}') &= \hat{r}_{ij}^{\boldsymbol{v}_h}(\boldsymbol{x}') \\ &= \int e^{i\omega[\tau - R_{ij}(\mathbf{x}',s)/c_0 - B_{ij}(\mathbf{x}',\mathbf{v}_h,s)/c_0]} d_{ij}(s,\tau) Q_{ij}^{\boldsymbol{v}_h}(\omega, s, \boldsymbol{x}')\, d\omega ds d\tau\end{aligned} \tag{4.8}$$

where Q_{ij} is the filter that varies slowly with ω derived in [79].

The final image is formed by coherently summing over all pairs of images:

$$\hat{r}^{\boldsymbol{v}_h}(\boldsymbol{x}') = \sum_{i,j} \hat{r}_{ij}^{\boldsymbol{v}_h}(\boldsymbol{x}'). \tag{4.9}$$

Note that under the assumption that A_{ij} and Q_{ij} are slow-varying functions of ω, both $\mathcal{F}$ and $\mathcal{K}$ become Fourier Integral Operators (FIO).

The point spread function (PSF) analysis in [79] shows that irrespective of the choice of Q_{ij}, the backprojection operator positions the scatterer located at $\mathbf{x}$ in the scene correctly in the reconstructed image whenever $\mathbf{v}_h = \mathbf{v}_{\mathbf{x}}$. Additionally, we design the filter Q_{ij} so that the PSF function is approximately $\delta(\mathbf{x} - \mathbf{x}')$ whenever $\mathbf{v}_h = \mathbf{v}_{\mathbf{x}}$. This filter is found to be

$$Q_{ij}(\boldsymbol{\xi}_{ij}, \boldsymbol{x}', \boldsymbol{v}_h) = \frac{\chi_\Omega A_{ij}^*(\boldsymbol{\xi}_{ij}, \boldsymbol{x}', \boldsymbol{v}_h)}{|A_{ij}(\boldsymbol{\xi}_{ij}, \boldsymbol{x}', \boldsymbol{v}_h)|^2} \frac{|\omega|}{c_0^2} |\Xi_{ij,1}\dot{\Xi}_{ij,2} - \Xi_{ij,2}\dot{\Xi}_{ij,1}|, \tag{4.10}$$

where $\boldsymbol{\Xi}_{ij} = [\boldsymbol{\Xi}_{ij,1}, \boldsymbol{\Xi}_{ij,2}]$, with

$$\boldsymbol{\Xi}_{ij}(s, \boldsymbol{x}', \boldsymbol{v}) = \nabla_{\boldsymbol{x}}[-R_{ij}(\mathbf{x}, s) - B_{ij}(\mathbf{x}, \mathbf{v}, s)]|_{\boldsymbol{x}=\boldsymbol{x}'} \tag{4.11}$$

and

$$\boldsymbol{\xi}_{ij} = \frac{\omega}{c_0} \boldsymbol{\Xi}_{ij}(s, \boldsymbol{x}', \boldsymbol{v}). \tag{4.12}$$

χ_Ω is a smooth cut-off function to prevent division by zero, Ω is the set of points $\mathbf{x}'$ where $A_{ij}(\omega, s, \boldsymbol{x}, \boldsymbol{v}) \neq 0$ and A_{ij}^* denotes the complex conjugate of A_{ij}.

4.2.3 Velocity Estimation Algorithm

To estimate the velocity of the moving targets, a stack of images is formed by filtering and backprojecting the correlated data over a range of hypothesized velocities. Minimum entropy is then used as a measure of focus for each image. Entropy is computed for each image by

$$\mathrm{En}(\boldsymbol{v}_h) = -\sum_{\boldsymbol{x}'} p(\hat{r}(\boldsymbol{x}', \boldsymbol{v}_h)) \log[p(\hat{r}(\boldsymbol{x}', \boldsymbol{v}_h))], \tag{4.13}$$

where p is a normalized histogram for the discrete image. Since moving targets are focused more sharply when their hypothesized velocity is correct, target velocities are determined by the local minima of En over the range of hypothesized velocities.

In the following two sections, we analyze position and velocity resolutions and the positioning errors due to incorrect estimation of target velocities.

4.3 Resolution Analysis

This section analyzes the resolution in the available data for both position and velocity. This tells us which factors are important to focus on for increasing the resolution in each of these dimensions, allowing for more accurate image reconstruction and velocity estimation. First, we study the resolution in reconstructing a position image for the correct hypothesized velocity. Afterward, the velocity resolution available in the data is analyzed.

4.3.1 Resolution of Reconstructed Position Images

To analyze the resolution of the reconstructed images, we analyze the bandwidth of the point spread function. Recall that the PSF of the imaging operator $\mathcal{K}$ is the kernel of the image fidelity operator $\mathcal{KF}$. When the hypothesized velocity $\boldsymbol{v}_h$ is equal to the correct velocity $\boldsymbol{v}_{\mathbf{x}}$ and the filter Q_{ij} is chosen as in (4.10), for a given pair of receivers this kernel is approximated by

$$L_{ij}^{(\boldsymbol{v}_h, \boldsymbol{v}_h)}(\boldsymbol{x}, \boldsymbol{x}') = \int_{\Omega_{ij}} e^{i(\boldsymbol{x}-\boldsymbol{x}')\cdot\boldsymbol{\xi}_{ij}} d\boldsymbol{\xi}_{ij}, \tag{4.14}$$

where

$$\Omega_{ij} = \{\boldsymbol{\xi}_{ij} : \boldsymbol{\xi}_{ij} = \frac{\omega}{c_0}\boldsymbol{\Xi}_{ij}(s, \boldsymbol{x}', \boldsymbol{v}_h),\ \boldsymbol{x}' \in \operatorname{supp}(A_{ij}Q_{ij}^{\boldsymbol{v}_h}\}. \tag{4.15}$$

The point spread function shows that the reconstructed image is a band-limited version of the original image, with a bandwidth determined by the data collection manifold, Ω_{ij}. Alternatively, we can interpret the vector $\boldsymbol{\xi}_{ij}$ as the Fourier vector that contributes to the reconstruction of the pixel at $\boldsymbol{x}'$. Thus, to obtain good resolution at $\boldsymbol{x}'$, it is desirable for this vector to span a wide range of angles and have a large magnitude. The bandwidth contribution of $\boldsymbol{\xi}_{ij}$ to the reconstructed image is

$$\begin{aligned} |\boldsymbol{\xi}_{ij}| = \Bigg| \frac{\omega}{c_0} \Bigg[& D\psi(\boldsymbol{x}')[(\widehat{\mathbf{x}' - \boldsymbol{\gamma}_i(s)}) - (\widehat{\mathbf{x}' - \boldsymbol{\gamma}_j(s)})] \\ & - \frac{D\psi(\boldsymbol{x}') \cdot \mathbf{v}_i^{\perp} s + \partial_{\boldsymbol{x}'}^2 \psi(\boldsymbol{x}') \cdot \boldsymbol{v}(\psi(\boldsymbol{x}') - \boldsymbol{\gamma}_i^3(s))s}{|\mathbf{x}' - \boldsymbol{\gamma}_i(s)|} \\ & + \frac{D\psi(\boldsymbol{x}') \cdot \mathbf{v}_j^{\perp} s + \partial_{\boldsymbol{x}'}^2 \psi(\boldsymbol{x}') \cdot \boldsymbol{v}(\psi(\boldsymbol{x}') - \boldsymbol{\gamma}_j^3(s))s}{|\mathbf{x}' - \boldsymbol{\gamma}_j(s)|} \Bigg] \Bigg|, \end{aligned} \tag{4.16}$$

where

$$D\psi(\boldsymbol{x}) = \begin{bmatrix} 1 & 0 & \partial\psi(\boldsymbol{x})/\partial x_1 \\ 0 & 1 & \partial\psi(\boldsymbol{x})/\partial x_2 \end{bmatrix}, \tag{4.17}$$

and

$$\mathbf{v}_i^{\perp} = \mathbf{v} - (\widehat{\mathbf{x} - \boldsymbol{\gamma}_i(s)})[(\widehat{\mathbf{x} - \boldsymbol{\gamma}_i(s)}) \cdot \mathbf{v}], \tag{4.18}$$

$$\mathbf{v}_j^{\perp} = \mathbf{v} - (\widehat{\mathbf{x} - \boldsymbol{\gamma}_j(s)})[(\widehat{\mathbf{x} - \boldsymbol{\gamma}_j(s)}) \cdot \mathbf{v}]. \tag{4.19}$$

The $D\psi(\boldsymbol{x})$ matrix projects a three dimensional vector onto the tangent plane of the ground topography. Note that $\mathbf{v}_i^{\perp}$ represents the component of the target velocity in the direction perpendicular to the look direction, $(\widehat{\mathbf{x} - \boldsymbol{\gamma}_i(s)})$ of the ith receiver.

For flat topography, (4.16) simplifies to

$$|\boldsymbol{\xi}_{ij}| = \left| \frac{\omega}{c_0} D\psi(\boldsymbol{x}') \left[[(\widehat{\mathbf{x}' - \boldsymbol{\gamma}_i(s)}) - (\widehat{\mathbf{x}' - \boldsymbol{\gamma}_j(s)})] + \frac{\mathbf{v}_j^{\perp} s}{|\mathbf{x}' - \boldsymbol{\gamma}_j(s)|} - \frac{\mathbf{v}_i^{\perp} s}{|\mathbf{x}' - \boldsymbol{\gamma}_i(s)|} \right] \right|. \tag{4.20}$$

From this equation we can make conclusions about the resolution of the reconstructed image. First, we see that the bandwidth of the transmitted waveform, $f = \omega/2\pi$, directly contributes to the magnitude of $\boldsymbol{\xi}_{ij}$, and increasing this parameter yields a corresponding increase in reconstructed image resolution.

If we assume a stationary scene, the two $\mathbf{v}^{\perp}$ terms vanish and we are left with the hitchhiker look direction, which is the difference in antenna look directions $(\widehat{\mathbf{x}' - \boldsymbol{\gamma}_i(s)}) - (\widehat{\mathbf{x}' - \boldsymbol{\gamma}_j(s)})$ projected onto the tangent plane of the ground topography. The magnitude of this term is proportional to the hitchhiker angle θ_h, which is the angle between the projection of these two vectors onto the tangent plane of the ground topography:

$$|D\psi(\boldsymbol{x}')(\widehat{\mathbf{x}' - \boldsymbol{\gamma}_i(s)}) - D\psi(\boldsymbol{x}')(\widehat{\mathbf{x}' - \boldsymbol{\gamma}_j(s)})| = 2|\sin(\theta_h/2)|. \tag{4.21}$$

This angle is depicted in Figure 4.1. When this angle is small the antennas are close together, and this term will approach zero. For the best resolution, the sine function should be maximized by forcing $\theta_h = 180^\circ$, i.e., a larger the hitchhiker angle increases the position resolution.

Additionally, the bandwidth contribution of $\boldsymbol{\xi}_{ij}$ to the reconstructed image is affected by the target velocities. To understand the contribution of the velocity of moving targets to position resolution, we decompose $\boldsymbol{\xi}_{ij}$ into two components

$$\mathbf{L}_{ij} = \mathbf{L}_{ij}(\mathbf{x}', s) = (\widehat{\mathbf{x}' - \boldsymbol{\gamma}_i(s)}) - (\widehat{\mathbf{x}' - \boldsymbol{\gamma}_j(s)}), \tag{4.22}$$

$$\mathbf{V}_{ij} = \mathbf{V}_{ij}(\mathbf{x}', \mathbf{v}, s) = \frac{\mathbf{v}_j^{\perp} s}{|\mathbf{x}' - \boldsymbol{\gamma}_j(s)|} - \frac{\mathbf{v}_i^{\perp} s}{|\mathbf{x}' - \boldsymbol{\gamma}_i(s)|}, \tag{4.23}$$

where (4.22) denotes the hitchhiker look direction and (4.23) defines the velocity components of $\boldsymbol{\xi}_{ij}$ given in (4.20). Assuming that $|\mathbf{v}_i^{\perp} s| \ll |\mathbf{x}' - \boldsymbol{\gamma}_i(s)|$ for all i, we

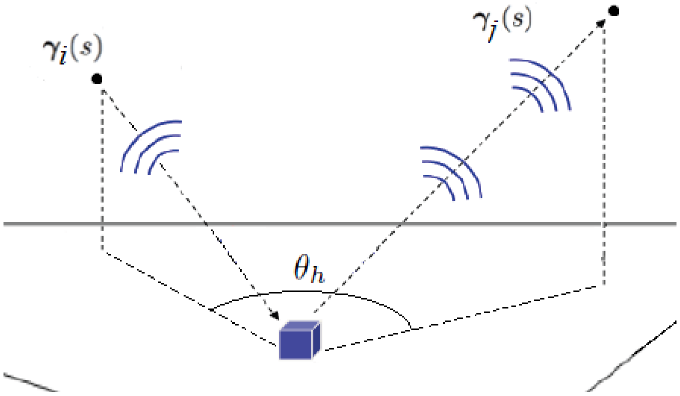

Figure 4.1: Hitchhiker angle θ_h, the angle between the antenna look direction vectors projected onto the tangent plane of the ground topography.

make the following approximation

$$|\mathbf{L}_{ij} + \mathbf{V}_{ij}| \approx |\mathbf{L}_{ij}| + \hat{\mathbf{L}}_{ij} \cdot \mathbf{V}_{ij}. \tag{4.24}$$

From this equation, we see that the bandwidth contribution is proportional to the component of the velocity term in the hitchhiker look direction. $\mathbf{v}_i^{\perp}$ is orthogonal to the look direction of antenna i and $\mathbf{v}_j^{\perp}$ is orthogonal to the look direction of antenna j, i.e.,

$$(\widehat{\mathbf{x}' - \boldsymbol{\gamma}_i(s)}) \cdot \mathbf{v}_i^{\perp} = 0, \tag{4.25}$$

$$(\widehat{\mathbf{x}' - \boldsymbol{\gamma}_j(s)}) \cdot \mathbf{v}_j^{\perp} = 0. \tag{4.26}$$

Therefore, the dot product simplifies to

$$\begin{aligned} \hat{\mathbf{L}}_{ij} \cdot \mathbf{V}_{ij} =& \frac{(\widehat{\mathbf{x}' - \boldsymbol{\gamma}_i(s)}) \cdot \mathbf{v}_j^{\perp} s}{|\mathbf{x}' - \boldsymbol{\gamma}_j(s)|} + \frac{(\widehat{\mathbf{x}' - \boldsymbol{\gamma}_j s})) \cdot \mathbf{v}_i^{\perp} s}{|\mathbf{x}' - \boldsymbol{\gamma}_i(s)|} \\ =& |\mathbf{v}| \sin(\theta_h) s \left[\frac{\sin\theta_j}{|\mathbf{x}' - \boldsymbol{\gamma}_j(s)|} + \frac{\sin\theta_i}{|\mathbf{x}' - \boldsymbol{\gamma}_i(s)|} \right], \end{aligned} \tag{4.27}$$

where $\sin(\theta_i)$ and $\sin(\theta_j)$ are the angles between the velocity vector and look directions of antennas i and j, respectively. In this expression, the distances between the scene and each of the receivers, $|\mathbf{x}' - \boldsymbol{\gamma}_i(s)|$ and $|\mathbf{x}' - \boldsymbol{\gamma}_j(s)|$, are negatively correlated with the magnitude of $\boldsymbol{\xi}_{ij}$. Therefore, the closer the antennas are to the scene of interest, the better the resulting image resolution. In addition, the magnitude is also directly proportional to the magnitude $|\mathbf{v}|$, so the resolution also increases with the speed of the moving target. Finally, the sine of all three angles are present in this expression. The closer the angles are to 90°, the larger these terms will be.

High image resolution also requires a wide angular diversity in $\boldsymbol{\xi}_{ij}$ vectors. The direction of $\boldsymbol{\xi}_{ij}$ is determined largely by the hitchhiker look direction. The angular span of the $\boldsymbol{\xi}_{ij}$ vectors in the data collection manifold is determined by the "effective" length of the aperture. Assuming that appropriate flight trajectories are chosen, the aperture length is directly proportional to the length of s and the number of receiver pairs. Figure 4.2 shows the set of Fourier vectors, $\boldsymbol{\xi}_{ij}$, $i, j = 1, 2, 3$ obtained by three receivers each traversing a 45° arc over a circular aperture in tandem for a set of slow-time values. We see that each pair of receivers collects $\boldsymbol{\xi}_{ij}$ vectors spanning a different range of directions for the same set of slow-time values. The angular range of the Fourier vectors for each pair depends on the length of slow-time and the magnitude of the Fourier vectors depends on the hitchhiker look-direction for a fixed bandwidth. Clearly, increasing the number of receivers increases the angular span of the Fourier vectors for a fixed coherent processing interval (CPI). Hence a large number of receivers can be used to collect high resolution information in a relatively short CPI. This may be advantageous in imaging fast maneuvering targets.

Table 4.1 summarizes these conclusions. Under most conditions, the stationary term will dominate, since the velocity component is normalized by the antenna ranges. The dominating parameters here are represented in the first part of the table above the horizontal line. However, when this stationary term becomes small it can still be affected by the velocity component. These parameters are shown in the second part of the table.

4.3.2 Velocity Resolution

Our image formation method reconstructs position images for a discrete set of velocities in a given range. The sampling of the velocity range is limited by the velocity resolution available in the acquired data. To understand the velocity

Table 4.1: Table of Image Resolution Parameters

Parameter	Increase (↑)	Resolution
Signal bandwidth $f = \omega/2\pi$	↑	↑
Hitchhiker angle $\sin(\theta_h/2)$	↑	↑
Distance $\|\mathbf{x}' - \boldsymbol{\gamma}_i(s)\|$, $\|\mathbf{x}' - \boldsymbol{\gamma}_j(s)\|$	↑	↓
Target speed $\|\mathbf{v}\|$	↑	↑
Angles between antenna look direction and target velocity θ_i, θ_j	↑	↑
Aperture length s	↑	↑
Number of receivers	↑	↑

resolution and how finely the range of velocities can be discretized, we analyze the velocity bandwidth available in the data using the forward model (4.2).

We rewrite the forward model (4.2) in the following alternative form

$$\mathcal{F}[r](s,\tau) = \int e^{i\boldsymbol{\varsigma}\cdot\boldsymbol{v}} e^{-i\omega[\tau - R_{ij}(s,\mathbf{x})/c_0]} A_{ij}(\omega, s, \boldsymbol{x}, \boldsymbol{v}) r(\boldsymbol{x}, \boldsymbol{v}) \, d\boldsymbol{x} d\boldsymbol{v} d\omega \tag{4.28}$$

where

$$\boldsymbol{\varsigma} = \omega s[(\widehat{\mathbf{x} - \boldsymbol{\gamma}_i(s)}) - (\widehat{\mathbf{x} - \boldsymbol{\gamma}_j(s)})]. \tag{4.29}$$

We can now interpret $\boldsymbol{\varsigma}$ as the Fourier vector associated with the velocity of the scatterer located at $\mathbf{x}$ at $s = 0$. In an analogous fashion to the $\boldsymbol{\xi}$ vector in Equation (4.14), the $\boldsymbol{\varsigma}$ vector provides information about the resolution in the velocity space. Directional diversity, as well as the length of this vector, determine the velocity resolution available in the correlated data d_{ij}. There are three factors that determine the length and direction of $\boldsymbol{\varsigma}$: the bandwidth of the transmitted waveform, the synthetic aperture length and hitchhiker look direction. All three factors agree with intuition. Larger transmitted waveform bandwidth implies shorter processing windows and hence finer acquisition of range variation from one processing window to another which translates into finer velocity information. Longer aperture length shows that more information about the target velocity can be acquired as the target moves farther away from its original location. Both of these parameters are scaled by the length of the hitchhiker look direction vector, which is maximized when the

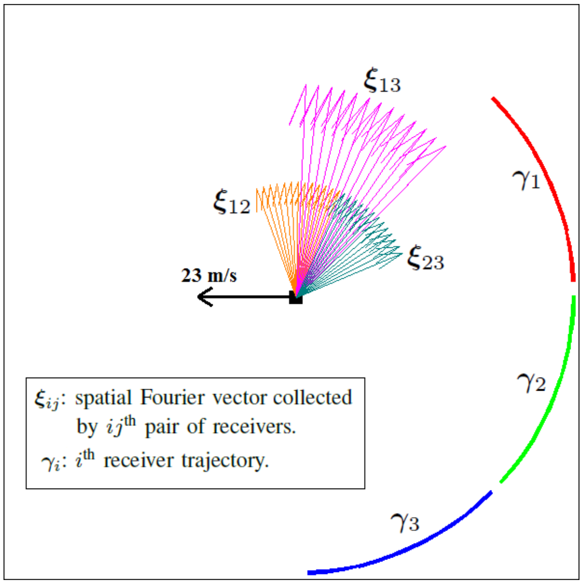

Figure 4.2: Data collection manifold Ω_{ij}, i.e. set of spatial Fourier vectors. $\boldsymbol{\xi}_{ij}$ for $i, j = 1, 2, 3$, collected by three pairs of receivers over a range of slow-time values for a point target moving with velocity 23 m/s towards the left. Each receiver is separated by $45°$ and traversing $45°$ of a circular aperture. Clearly, each pair of receivers increases the angular span of Fourier vectors for a fixed coherent processing interval.

hitchhiker angle is $180°$.

Similarly to the position error simulation, the angle of the $\boldsymbol{\varsigma}$ vector is determined by the hitchhiker look direction. Therefore, angular diversity in the ς vector is improved by a large synthetic aperture length as well as multiple receiver pairs. These parameters are summarized in Table 4.2.

Table 4.2: Table of Velocity Resolution Parameters

Parameter	Increase (↑)	Resolution
Transmitted waveform bandwidth $f = \omega/2\pi$	↑	↑
Aperture length s	↑	↑
Hitchhiker angle θ_h	↑	↑
Number of receivers	↑	↑

4.4 Position Error Analysis in Reconstructed Images Due to Incorrect Velocity

This section addresses the following important questions in passive SAR imaging of moving targets:

1. Passive SAR images of moving targets reconstructed under the stationary scene assumption contain positioning errors or smearing artifacts. Given the imaging geometry and target velocities, can we develop a theory to analyze and predict the positioning errors in SAR images? In return, such a theory can be utilized to determine target velocities.

2. We have shown in the previous chapter that radiance images can be focused if the target velocities are known a priori or correctly estimated. Based on this result, we reconstruct radiance images for a set of hypothesized velocities and select the velocity that yields the best focus. However, both the discretized hypothesized velocity and the estimated velocity may not be identically equal to the true velocity of the targets. Thus, if the hypothesized or estimated target velocity deviates from the true velocity, what would be the positioning errors in radiance images? Furthermore, if a small error is made in the hypothesized or estimated target velocity, is the resulting positioning error small? In other words, is our method of reconstructing radiance (position) images robust with respect to error in velocity estimation?

To analyze and predict positioning errors due to moving targets or erroneous velocity estimation, we use microlocal analysis, specifically the results that explain how the edges or scatterer locations in the scene are propagated into the reconstructed image by the filtered backprojection operator (4.8).

The concept of canonical relations explains how an FIO propagates scene information to acquired data for a given imaging geometry and other parameters. The Hörmander-Sato theorem, which relies on the composition of the canonical relations [67, 66], describes how the information acquired from the scene is propagated into the reconstructed image via the composition of the two FIOs defined as forward and inverse maps.

Recall that from the previous chapter that the phase of the image fidelity operator $\mathcal{KF}$ is given by

$$\Phi_{ij}^{(\boldsymbol{v},\boldsymbol{v}_h)}(\omega, s, \mathbf{x}', \mathbf{x}) = \varphi_{ij}(\mathbf{x}', \mathbf{v}_h, s) - \varphi_{ij}(\mathbf{x}, \mathbf{v}, s) \tag{4.30}$$

$$= \frac{\omega}{c_0}[R_{ij}(\mathbf{x}', s) + B_{ij}(\mathbf{x}', \mathbf{v}_h, s) - R_{ij}(\mathbf{x}, s) - B_{ij}(\mathbf{x}, \mathbf{v}, s)] \tag{4.31}$$

where $\mathbf{x}$ and $\mathbf{v}$ are scene parameters or target position and velocity and $\mathbf{x}'$ is the image parameter and $\mathbf{v}_h$ is the hypothesized velocity for which the FBP image is formed. The Hörmander-Sato theorem tells us that a scatterer located at $\mathbf{x}$ at $s = 0$ moving with velocity $\mathbf{v}_\mathbf{x}$ is formed at locations $\mathbf{x}'$ moving with velocity $\mathbf{v}_h$ that satisfy the two equations

$$\partial_\omega \Phi_{ij}^{(\boldsymbol{v},\boldsymbol{v}_h)}(\omega, s, \mathbf{x}', \mathbf{x}) = \varphi_{ij}(\mathbf{x}', \mathbf{v}_h, s) - \varphi_{ij}(\mathbf{x}, \mathbf{v}, s) = 0, \tag{4.32}$$

$$\partial_s \Phi_{ij}^{(\boldsymbol{v},\boldsymbol{v}_h)}(\omega, s, \mathbf{x}', \mathbf{x}) = \dot{\varphi}_{ij}(\mathbf{x}', \mathbf{v}_h, s) - \dot{\varphi}_{ij}(\mathbf{x}, \mathbf{v}, s) = 0, \tag{4.33}$$

where $\dot{\varphi}$ denotes the derivative of φ with respect to s. Clearly, one of the solutions of (4.32) and (4.33) is $\mathbf{x}' = \mathbf{x}$ when $\mathbf{v}_h = \mathbf{v}_\mathbf{x}$, which tells us that the scatter is reconstructed at the correct position (and orientation) whenever the hypothesized velocity of the scatterer is equal to its true velocity. Now let us assume that an error is made in the hypothesized velocity, i.e., $\mathbf{v}_h$ used in image reconstruction does not equal $\mathbf{v} = \mathbf{v}_\mathbf{x}$ but rather

$$\mathbf{v}_\epsilon = \mathbf{v}_\mathbf{x} + \epsilon \Delta \mathbf{v}, \tag{4.34}$$

where $\epsilon \Delta \mathbf{v}$ is the error in hypothesized velocity and ϵ is a small constant. The backprojection operator then maps the scatterer to an erroneous location $\mathbf{x}' + \Delta \mathbf{x}'$ in the reconstructed image that satisfies the conditions

$$\varphi_{ij}(\mathbf{x}' + \Delta \mathbf{x}', \mathbf{v} + \epsilon \Delta \mathbf{v}, s) - \varphi_{ij}(\mathbf{x}, \mathbf{v}, s) = 0, \tag{4.35}$$

$$\dot{\varphi}_{ij}(\mathbf{x}' + \Delta \mathbf{x}', \mathbf{v} + \epsilon \Delta \mathbf{v}, s) - \dot{\varphi}_{ij}(\mathbf{x}, \mathbf{v}, s) = 0, \tag{4.36}$$

where $\Delta\mathbf{x}'$ denotes the positioning error due to velocity error $\epsilon\Delta\mathbf{v}$. Our objective is to determine an approximate expression for $\Delta\mathbf{x}'$ in terms of the velocity error $\epsilon\Delta\mathbf{v}$.

By making a Taylor series approximation around $\epsilon = 0$ for each equation, we find the following relationships for position error:

$$\begin{aligned} \Xi_{ij}(\mathbf{x}', \mathbf{v}, s) \cdot \Delta\mathbf{x}' &= -\mathbf{L}_{ij}(\mathbf{x}', s) \cdot \Delta\mathbf{v} s\epsilon, \qquad (4.37) \\ -\dot{\Xi}_{ij}(\mathbf{x}', \mathbf{v}, s) \cdot \Delta\mathbf{x}' &= \mathbf{L}_{ij}(\mathbf{x}', s) \cdot \Delta\mathbf{v}\epsilon - \dot{\mathbf{L}}_{ij}(\mathbf{x}', s) \cdot \Delta\mathbf{v} s\epsilon, \qquad (4.38) \end{aligned}$$

where $\mathbf{L}_{ij}(\mathbf{x}', s)$ is the hitchhiker look direction

$$\mathbf{L}_{ij}(\mathbf{x}', s) = [(\widehat{\mathbf{x}' - \boldsymbol{\gamma}_i(s)}) - (\widehat{\mathbf{x}' - \boldsymbol{\gamma}_j(s)})], \qquad (4.39)$$

and $\dot{\mathbf{L}}_{ij}(\mathbf{x}', s)$ represents the derivative of $\mathbf{L}_{ij}(\mathbf{x}', s)$ with respect to s. It is given by

$$\dot{\mathbf{L}}_{ij}(\mathbf{x}', s) = \frac{\dot{\boldsymbol{\gamma}}_i^{\perp}(s)}{|\mathbf{x}' - \boldsymbol{\gamma}_i(s)|} - \frac{\dot{\boldsymbol{\gamma}}_j^{\perp}(s)}{|\mathbf{x}' - \boldsymbol{\gamma}_j(s)|}, \qquad (4.40)$$

with

$$\begin{aligned} \dot{\boldsymbol{\gamma}}_i^{\perp}(s) &= \dot{\boldsymbol{\gamma}}_i(s) - (\widehat{\mathbf{x}' - \boldsymbol{\gamma}_i(s)})[\dot{\boldsymbol{\gamma}}_i(s) \cdot (\widehat{\mathbf{x}' - \boldsymbol{\gamma}_i(s)})], \qquad (4.41) \\ \dot{\boldsymbol{\gamma}}_j^{\perp}(s) &= \dot{\boldsymbol{\gamma}}_j(s) - (\widehat{\mathbf{x}' - \boldsymbol{\gamma}_j(s)})[\dot{\boldsymbol{\gamma}}_j(s) \cdot (\widehat{\mathbf{x}' - \boldsymbol{\gamma}_j(s)})]. \qquad (4.42) \end{aligned}$$

See Appendix C for the derivation of (4.37) and (4.38).

Note that $\dot{\boldsymbol{\gamma}}_i^{\perp}(s)$ represents the component of the velocity of the ith receiver in the direction perpendicular to the look direction of the receiver.

Equations (4.37) and (4.38) represent the amount of position error in the direction of two different vectors: Ξ_{ij} and $\dot{\Xi}_{ij}$. To see the true error magnitude in each direction, we normalize the two equations with respect to the magnitude of these vectors and obtain

$$\widehat{\boldsymbol{\Xi}}_{ij} \cdot \Delta\mathbf{x}' = \frac{-1}{|\boldsymbol{\Xi}_{ij}|}\mathbf{L}_{ij}(\mathbf{x}', s) \cdot \Delta\mathbf{v}s\epsilon, \tag{4.43}$$

$$\widehat{\dot{\boldsymbol{\Xi}}}_{ij} \cdot \Delta\mathbf{x}' = \frac{-1}{|\dot{\boldsymbol{\Xi}}_{ij}|}\left[\mathbf{L}_{ij}(\mathbf{x}', s) \cdot \Delta\mathbf{v}\epsilon - \dot{\mathbf{L}}_{ij}(\mathbf{x}', s) \cdot \Delta\mathbf{v}s\epsilon\right]. \tag{4.44}$$

It is important to note that the magnitude factor $|\dot{\boldsymbol{\Xi}}_{ij}|$ contains the range terms in the denominator. When we normalize the second equation and divide by this magnitude, the range terms multiply the error, which can result in a significant quantity. To understand this error relationship further, we analyze the simplified case of a short synthetic aperture viewing a small scene. Additionally, we assume the antenna ranges are of the same order: $|\mathbf{x}' - \boldsymbol{\gamma}_i(s)| \approx |\mathbf{x}' - \boldsymbol{\gamma}_j(s)|$. Under these assumptions, we have the relationships

$$\mathbf{L}_{ij} \perp [\dot{\boldsymbol{\gamma}}_i^{\perp}(s) - \dot{\boldsymbol{\gamma}}_j^{\perp}(s)], \tag{4.45}$$

$$\mathbf{L}_{ij} \approx \boldsymbol{\Xi}_{ij}. \tag{4.46}$$

Thus, the position errors in (4.43) and (4.44) further simplify to

$$\widehat{\mathbf{L}}_{ij} \cdot \Delta\mathbf{x}' = -\widehat{\mathbf{L}}_{ij}(\mathbf{x}', s) \cdot \Delta\mathbf{v}s\epsilon, \tag{4.47}$$

$$\widehat{\dot{\mathbf{L}}}_{ij} \cdot \Delta\mathbf{x}' = \frac{-1}{|\dot{\boldsymbol{\Xi}}_{ij}|}\left[\mathbf{L}_{ij}(\mathbf{x}', s) \cdot \Delta\mathbf{v}\epsilon - \dot{\mathbf{L}}_{ij}(\mathbf{x}', s) \cdot \Delta\mathbf{v}s\epsilon\right]. \tag{4.48}$$

We look at two extreme cases: the velocity error perpendicular to the hitchhiker look direction and the velocity error parallel to the hitchhiker look direction. In the case where the velocity error is perpendicular to the hitchhiker look direction, $\Delta\mathbf{v} \perp \mathbf{L}_{ij}$. Here, the first equation becomes zero and all of the position error is in the direction of $\dot{\boldsymbol{\Xi}}_{ij}$, as shown in the second equation. In the second case, where $\Delta\mathbf{v} \parallel \mathbf{L}_{ij}$, we obtain a position error in both directions. This is because the first equation is only in the direction of $\mathbf{L}_{ij}$, while the second equation has both the hitchhiker look direction and perpendicular antenna velocity direction. These conclusions are summarized in Table 4.3.

Table 4.3: Table of Position and Velocity Error Relationships

Case	Error in $\mathbf{L}_{ij}$	Error in $\dot{\mathbf{L}}_{ij}$
Velocity error perpendicular to look direction ($\Delta\mathbf{v} \perp \mathbf{L}_{ij}$)	None	$\frac{1}{\lvert\dot{\boldsymbol{\Xi}}_{ij}\rvert}\dot{\mathbf{L}}_{ij} \cdot \Delta\mathbf{v}s\epsilon$
Velocity error parallel to look direction ($\Delta\mathbf{v} \parallel \mathbf{L}_{ij}$)	$-\hat{\mathbf{L}}_{ij} \cdot \Delta\mathbf{v}s\epsilon$	$\frac{-1}{\lvert\dot{\boldsymbol{\Xi}}_{ij}\rvert}\mathbf{L}_{ij} \cdot \Delta\mathbf{v}\epsilon$

From the analysis presented in this section, we draw two important conclusions: 1. If a scene has moving targets and the backprojection image is reconstructed under the assumption that the scene is stationary, equations (4.43) and (4.44) quantify the smearing artifacts or positioning errors in the reconstructed image with $\Delta\mathbf{v} = -\mathbf{v}_{\mathbf{x}}$, where $\mathbf{v}_{\mathbf{x}}$ corresponds to the target velocity at true position $\mathbf{x}$. 2. Equations (4.43) and (4.44) show that if the error in hypothesized velocity is in the order of ϵ, then the positioning errors in the FBP images are also in the order of ϵ. Hence, our image reconstruction method is robust. In the following section, we numerically validate the analysis and theory presented in this and previous sections.

4.5 Numerical Simulations

This section presents two sets of numerical simulations to demonstrate the different types of theoretical performance analysis presented in the previous sections. All of the simulations are performed with a square scene of size [512 × 512] meters discretized into [128 × 128] pixels, so that each pixel represents 4 square meters. The receiving antennas fly in a circular flight trajectory around the scene with a radius of 1.5 km, an altitude of 1 km, and a speed of 261 m/s. The number of receivers, distance traveled, and separation of receivers were all varied in order to demonstrate these individual effects on image resolution.

Since our image formation method is based on filtered backprojection onto iso-range curves, we need high resolution waveforms with large bandwidth. Some examples of waveforms applicable to our method would be wireless network signals (WiFi), digital video broadcasting terrestrial (DVB-T) signals, and WiMAX waveforms. These signals have bandwidths in the MHz range [15], [37]. The transmitter is a stationary tower located outside the circular flight trajectory at a distance of about 2.1 km from the center of the scene. The transmitter uses a rectangular pulse of various lengths to demonstrate the impact of signal bandwidth on image resolution. A graphical illustration of this setup is shown in Figure 4.3.

The data was generated by stepping through each slow-time and summing the signals scattered from each moving target in the scene. The velocity estimation and image reconstruction steps were performed as described in Section 4.2. Note that the image reconstruction and velocity estimation procedure is based on the forward model, which is only an approximation to the method by which the data is collected. These performance analysis simulations used one target moving at 8 m/s. The target's location is updated according to the slow-time variable, since we make the start-stop approximation in the model.

4.5.1 Resolution Analysis Simulations

In the first set of simulations, three different parameters are varied to show their increasing effect on image resolution for a correct hypothesized velocity. Transmitted wave bandwidth, synthetic aperture length, and hitchhiker angle all varied to demonstrate these dominant factors in image resolution.

First, we demonstrate the importance of bandwidth in image resolution. This was accomplished by changing the sampling frequency of the fast-time variable t, which is analogous to the transmitted pulse width and corresponds to bandwidth. The sampling frequency was varied in order to keep the bandwidth in a range around what one would find from available illuminating sources of opportunity, such as digital TV and WiMax signals [15], [37]. Bandwidth was varied from about 3 to 17 MHz. The simulations were performed with two receivers flying over half of a circular synthetic aperture. Table 4.4 shows the bandwidths used, as well as the 3-dB width of the cross-section of the reconstructed target in both the x-direction and y-direction. The decreasing target width indicates an increase in resolution, as we expect from an increasing bandwidth. Figures 4.4 and 4.5 show the reconstructed images, along with the plot of the horizontal cross-sections for the lowest and highest bandwidth used, respectively.

In the second set of simulations, we vary the length of the synthetic aperture.

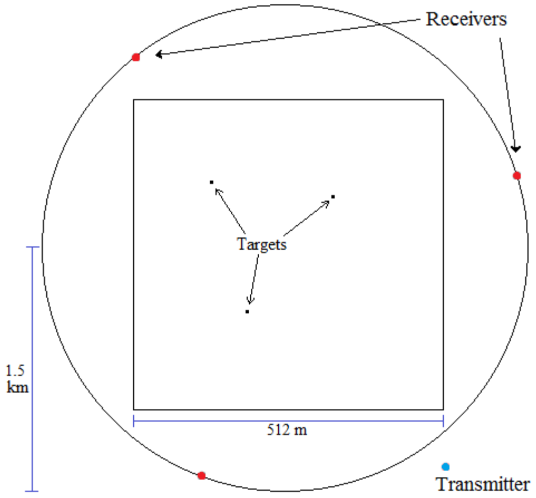

Figure 4.3: Setup for the simulations. The receivers move in a circular trajectory with a radius of 1.5 km, while the transmitter is stationary outside of the scene. The scene size is $[512 \times 512]$ **m.**

Here, two receivers traversed the circular trajectory separated by a phase of 180° for various amounts of time. The flight time was varied from 2.1 seconds to 10.6 seconds, corresponding to aperture lengths from about 548 m to 2767 m, and the corresponding target cross-section widths are shown in Table 4.5. Here we can see that the cross-range resolution (the x-direction in this scenario) is greatly improved by the increasing aperture length. Figures 4.6 and 4.7 show the reconstructed images, along with the plot of the horizontal cross-sections for the shortest and longest apertures used, respectively.

The third parameter altered was the hitchhiker angle, θ_h, discussed in Section 4.3. This angle is an important property of the geometry because it directly determines the amount of data that is able to be recovered by the receivers. We vary the angle from 10° to 70° and show the corresponding results in Table 4.6. Figures 4.8 and 4.9 show the reconstructed images along with the plot of the horizontal cross-sections for the smallest and largest angles used, respectively.

Table 4.4: Bandwidth of the sources of opportunity versus the 3 dB width of the reconstructed target in each direction

Bandwidth (MHz)	x-direction 3-dB Width (m)	y-direction 3-dB Width (m)
2.8	83.0	47.3
5.5	44.0	20.3
8.3	25.7	15.1
11.1	23.6	9.9
13.9	28.5	7.6
16.6	24.0	7.4

Table 4.5: Aperture length of the receiving antennas versus the 3 dB width of the reconstructed target in each direction

Aperture length (s)	x-direction 3-dB Width (m)	y-direction 3-dB Width (m)
2.1	52.6	4.2
4.2	26.9	4.3
6.3	17.6	4.3
8.5	16.0	4.4
10.6	14.8	4.8

Table 4.6: Hitchhiker angle between the receiving antennas versus the 3 dB width of the reconstructed target in each direction

Hitchhiker angle (degrees)	x-direction 3-dB Width (m)	y-direction 3-dB Width (m)
10	35.1	36.6
25	14.2	12.8
40	12.0	9.1
55	10.6	8.6
70	10.1	8.4

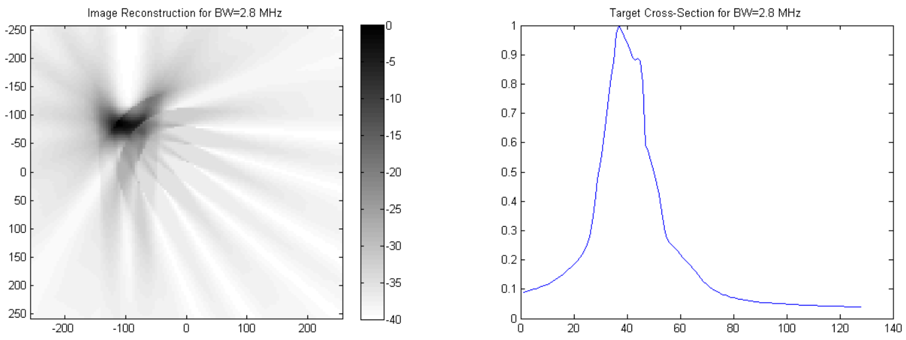

Figure 4.4: Results for the case of bandwidth = 2.8 MHz. Left is the reconstructed image and right is the plot of the cross-section of the moving target.

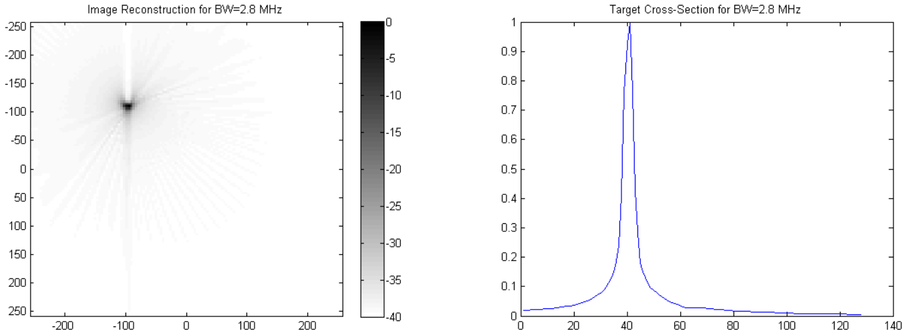

Figure 4.5: Results for the case of bandwidth = 16.6 MHz. Left is the reconstructed image and right is the plot of the cross-section of the moving target.

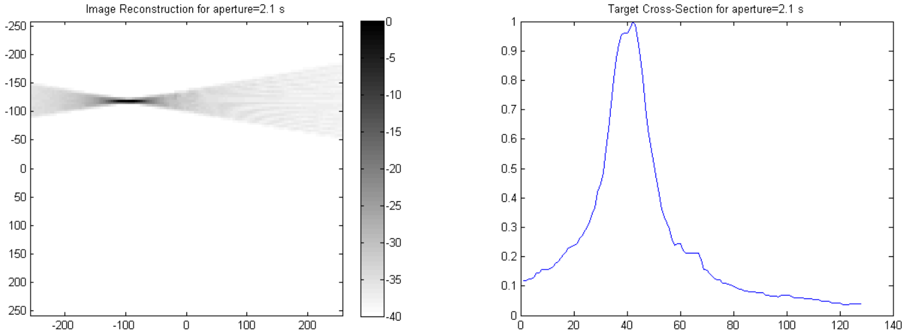

Figure 4.6: Results for the case of aperture length = 4.2 s. Left is the reconstructed image and right is the plot of the cross-section of the moving target.

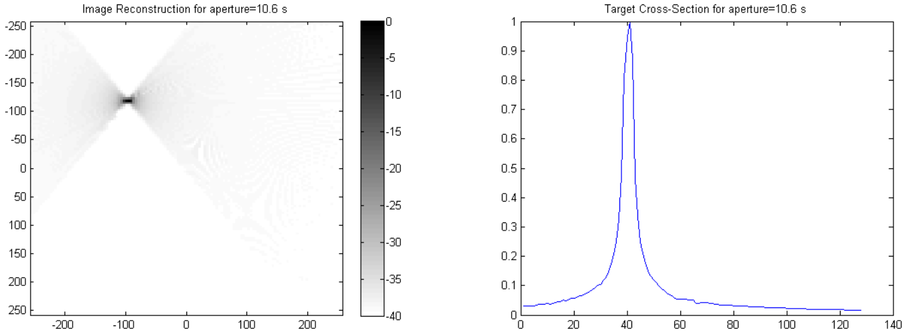

Figure 4.7: Results for the case of aperture length = 21.2 s. Left is the reconstructed image and right is the plot of the cross-section of the moving target.

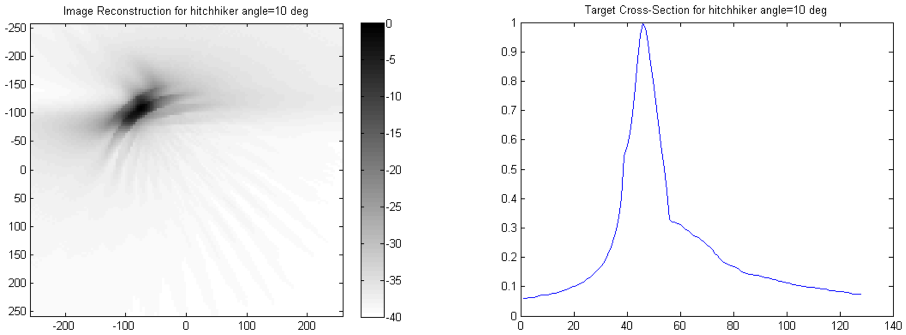

Figure 4.8: Results for the case of hitchhiker angle = 10°. Left is the reconstructed image and right is the plot of the cross-section of the moving target.

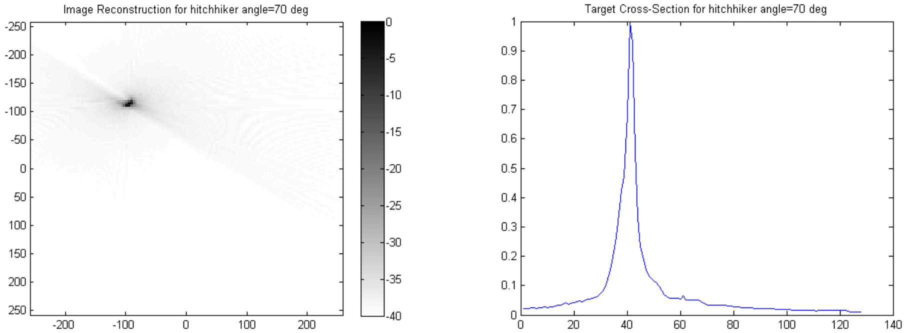

Figure 4.9: Results for the case of hitchhiker angle = 70°. Left is the reconstructed image and right is the plot of the cross-section of the moving target.

4.5.2 Position Error Simulations

This section presents a set of simulations to illustrate the analysis done previously for error in position as a result of an incorrect hypothesized velocity. In each of two scenarios, a short aperture and single target were used to simulate the scenario of an approximately constant look direction and small scene, respectively. In each case, the length of the aperture was 1.1 s and the speed of the moving target was 28 m/s. Additionally, the hypothesized velocity was zero, so the error in velocity was equal in magnitude but opposite in direction to the target's true velocity.

Figures 4.10 and 4.11 show results for the target traveling parallel and perpendicular, respectively, to the hitchhiker look direction for two antennas. The axes at the bottom-left of each image show these two directions, and the two markers

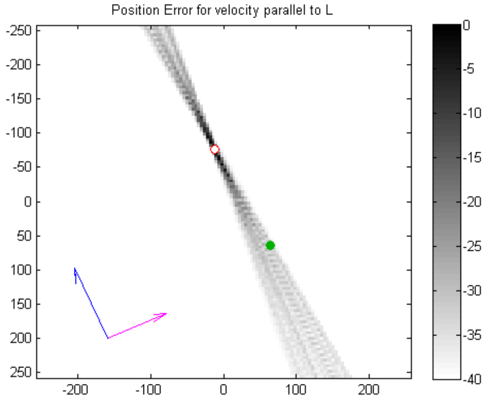

Figure 4.10: Reconstructed image with a short aperture and target traveling parallel to the hitchhiker look direction. The solid circle is the original location of the target, and the hollow circle is the reconstructed location.

show the true and reconstructed positions of the target. The dark, filled circle is the original location, and the empty circle is the reconstructed location.

Table 4.7 summarizes the numerical results of these simulations. The table shows both the calculated and measured position error for the target in each direction of each simulation. The calculated error was obtained from equations (4.47) and (4.48), and the measured error was obtained from finding the difference between the true and reconstructed target positions. The first two rows show the error for the first simulation, where the target was moving up and towards the right, parallel to the look direction. In this situation, we obtain error in both directions, since each has a $\mathbf{L} \cdot \Delta \mathbf{v}$ term. The last two rows show the results for the second simulation, where the target velocity is approximately perpendicular to the look direction. In this scenario, the error in the look direction is almost zero since the only term that contributes to error in this direction is the dot product between orthogonal vectors. In reality, the error is slightly higher than zero, because only an approximately orthogonal velocity was used, as well as error contributions by numerical rounding and image resolution. An error in the $\hat{\dot{\mathbf{L}}}$ direction is still found, since this error has contributing terms in addition to the look direction.

Another set of simulations was performed with the same imaging geometry as in the previous scenario but with the speed of the target varying in order to show

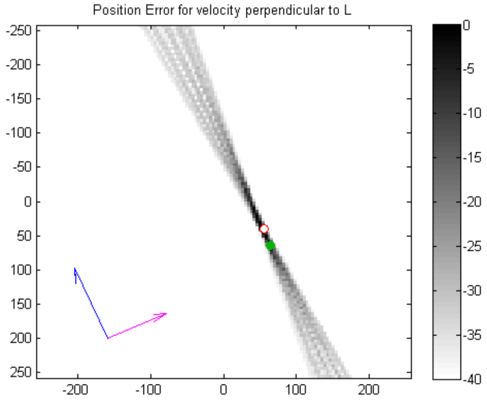

Figure 4.11: Reconstructed image with a short aperture and target traveling perpendicular to the hitchhiker look direction. The solid circle is the original location of the target, and the hollow circle is the reconstructed location.

Table 4.7: Table of Predicted vs Measured Position Error

Setup	Direction	Predicted Error	Measured Error
$\Delta\mathbf{v} \parallel \mathbf{L}_{ij}$	$\mathbf{L}_{ij}$	16.0	13.0
$\Delta\mathbf{v} \parallel \mathbf{L}_{ij}$	$\dot{\mathbf{L}}_{ij}$	157.7	158.7
$\Delta\mathbf{v} \perp \mathbf{L}_{ij}$	$\mathbf{L}_{ij}$	1.3	2.4
$\Delta\mathbf{v} \perp \mathbf{L}_{ij}$	$\dot{\mathbf{L}}_{ij}$	29.2	25.2

the linear relationship between velocity error and position error. The target was moving towards the right with a speed ranging from 0 to 17 m/s. The position error versus speed is plotted in the look direction, $\mathbf{L}_{ij}$, in Figure 4.12 and in the derivative of the look direction, $\dot{\mathbf{L}}_{ij}$, in Figure 4.13. The blue lines show the predicted error, computed from (4.47) and (4.48), and the red lines show the measured error. The variations and discrepancies between the predicted and measured errors arise mostly from two factors: the look direction is not constant over the flight trajectory (it must be approximated by the average look direction), and the position of the reconstructed target is estimated by simply extracting the brightest spot in the image. Nevertheless, these graphs clearly demonstrate the increasing nature of the position error as the speed of the target increases.

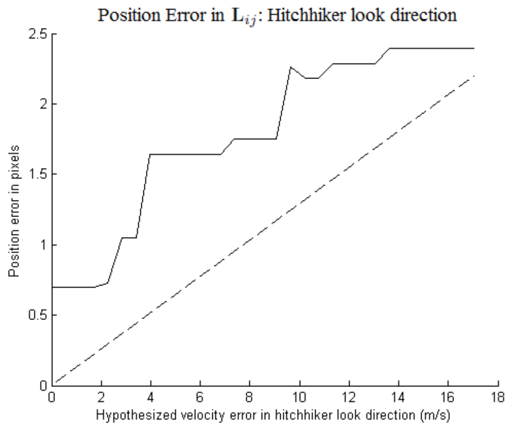

Figure 4.12: Plot of the measured (solid) and predicted (dashed) position error along the hitchhiker look direction axis. The error in this direction is generally much smaller, but the increasing relationship between position and velocity error can still be seen here.

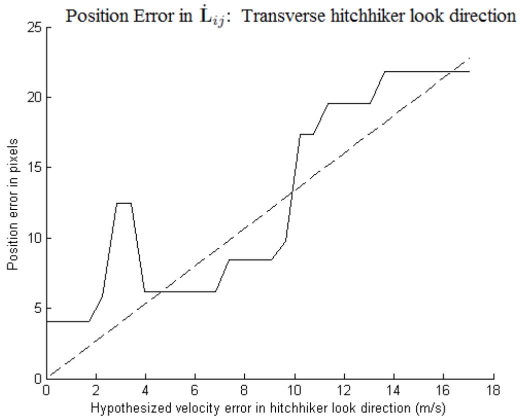

Figure 4.13: Plot of the measured (solid) and predicted (dashed) position error along the axis of the time derivative of the hitchhiker look direction. One can see from this plot that the position error tends to increase as the hypothesized velocity error increases, and low hypothesized velocity errors yield more accurate reconstructed target positioning.

4.6 Conclusion

This chapter provided a performance analysis of the image reconstruction and velocity estimation method presented in the previous chapter. Specifically we analyzed the resolution in both position and velocity spaces as well as the smearing artifacts from moving targets. The method is an extension of the stationary case investigated in [41]-[43], by collecting signals with a network of mobile, passive receivers. These signals are correlated, and filtered backprojection is used to reconstruct a series of images over a range of hypothesized velocities. Entropy is then used to analyze smearing and choose the focused images with the estimated velocity for each moving target. Performance analysis of this method allows us to identify important factors involved in optimizing the system for high image resolution and accurate velocity estimation.

We began with a quick overview of the important aspects of the algorithm detailed in Chapter 3. Next, a detailed resolution analysis was performed by looking at the form of the data from the forward model. Assuming a correctly hypothesized velocity, the image resolution was determined by looking at the bandwidth of the forward operator. Factors such as signal bandwidth, hitchhiker angle, number of receivers, and scene distance were identified as either contributing positively or negatively toward image resolution. Similarly for velocity resolution, the Fourier vector associated with velocity was analyzed to determine which factors increase or decrease the bandwidth in the velocity dimension of the data. Signal bandwidth, aperture length, and hitchhiker angle all contribute positively toward the velocity resolution. The angular span of the velocity Fourier vectors is increased with a large synthetic aperture or multiple receiver pairs. Increasing the number of receivers contributes to the angle diversity without increasing CPI, which is an important technique when imaging fast-maneuvering targets. The second major area of analysis involved the position error incurred when the hypothesized velocity is not equal to the true velocity. Simplifications were made to then split the error into two components: one in the hitchhiker look direction and the other in its perpendicular direction. We finally illustrated these results via numerical simulations.

Although the goal for this performance analysis was to analyze how imaging parameters affect position and velocity resolution as well as the positioning errors of moving targets, the method is applicable in the presence of additive white Gaussian noise. Under the assumption that the scene reflectivity and additive measurement noise are statistically uncorrelated and the additive measurement noise is zero-mean, then the cross-receiver correlation step yields a new random process (a new additive noise) that is a zero-mean and statistically uncorrelated in both slow-time and fast-time difference of arrival (the τ variable). Under these conditions, the filtered-backprojection (FBP) method will provide the minimum mean squared error image, as shown in [75]. For colored noise, the filter can be modified to include prewhitening as we have shown in [76].

In future work, other aspects of performance analysis that are useful may be explored. An analysis that studies the variation in image entropy with respect to hypothesized velocity can be performed. The selection of images from image stack will determine the accuracy of velocity estimates as well as the degree of smearing, since the smearing is a function of incorrect velocity estimates. Therefore, an analysis of entropy, the metric of choice for final image selection, would also provide a valuable understanding to the problem. Other examples are errors in receiver locations and phase coherence of the received signals. The algorithm and performance analysis both assume we have accurate locations for the mobile receivers at each slow-time; however, it is useful to analyze the error that occurs when there are small deviations between the true position and measured position of the antennas. Furthermore, the received signals at each receiver are combined coherently, so analyzing the effects of phase incoherence would be instructive as well. Additionally, the resolution analysis and position error analysis can be studied further to craft even more intelligent velocity estimation schemes. For example, the position error analysis can be used to describe various smearing artifacts in reconstructed images, which may then lead to an estimate of the velocity from the smears themselves. Finally, this work requires a relatively high bandwidth in order to accurately position the moving targets. However, since many of the available sources of opportunity transmit narrowband waveforms, obtaining high bandwidth may not always be possible. We investigate this scenario in the following chapters of this thesis.

CHAPTER 5

Doppler Synthetic Aperture Hitchhiker Imaging of Ground Moving Targets

5.1 Introduction

Doppler synthetic aperture radar (DSAR) uses ultra-narrowband waveforms to achieve high Doppler resolution instead of the high range resolution sought by conventional SAR. The synthetic aperture hitchhiker imaging of ground moving targets method presented in the previous chapters relies on the availability of relatively wideband sources of opportunity in order to take advantage of high range resolution to form position images of a scene of interest. However, many sources of opportunity are actually ultra-narrowband in nature, with bandwidths on the order of kHz.

. To form high resolution reflectivity (position) images, the data is backprojected onto iso-Doppler contours instead of the conventional iso-range contours. This radar modality has the distinct advantages of using cheaper transmitters, and in many cases, dedicated transmitters may not be required, since existing RF signals in the environment often have the desired ultra-narrowband properties. The Doppler imaging modality has been considered for the stationary case in [80]-[86]. Specifically, [81]-[84] consider the case of moving target imaging, but do not take into account clutter explicitly. The concept of using iso-Doppler contours for imaging with narrowband waveforms has also been presented in [87]-[89].

In addition, the Doppler SAR modality can be applied to passive imaging, since many transmitters of opportunity possess the desired ultra-narrowband properties. Passive imaging using sparse distributed apertures is described in [90], [91], and [36]. Furthermore, a theory for passive SAR imaging using ultra-narrowband sources of opportunity is described in [42] and [43]. In this modality, the received signals are cross-correlated between pairs of receivers in order to perform the imaging with limited knowledge of transmitter location.

5.2 Forward Model

The problem of passive moving target imaging with ultra-narrowband sources of opportunity plays a significant role in passive radar. Since many available sources of opportunity do not have a high enough bandwidth to obtain acceptable range resolution, we can use their narrowband frequency domain properties to reconstruct high resolution images. The goal of this problem is to obtain the data from Doppler shift instead of time delay and then backproject onto these iso-Doppler contours to obtain the reconstructed images.

5.2.1 Model for the Incident Field

The incident field for an antenna located at $\mathbf{y}$ transmitting the signal $s(t)$ is described by the wave equation

$$(\nabla^2 - \frac{1}{c}\partial_t^2)E^{in}(\mathbf{z},t) = \delta(\mathbf{z}-\mathbf{y})s(t). \tag{5.1}$$

The Green's function solution for free space is used to provide the solution for the electric field which we write as

$$(\nabla^2 - \frac{1}{c}\partial_t^2)g(\mathbf{z},t) = -\delta(\mathbf{z})\delta(t), \tag{5.2}$$

where

$$g(\mathbf{z},t) = \frac{\delta(t-|\mathbf{z}|/c_0)}{4\pi|\mathbf{z}|}, \tag{5.3}$$

and c_0 is the speed of light in a vacuum. Assuming a transmitter located at $\boldsymbol{\gamma}_T(t)$ transmitting a waveform $p(t)$ the electric field can be expressed as

$$E^{in}(\mathbf{z},t) = -\int \frac{\delta(t-t'-|\mathbf{z}-\boldsymbol{\gamma}_T(t)|/c_0)}{4\pi|\mathbf{z}-\boldsymbol{\gamma}_T(t)|}p(t')\,dt'. \tag{5.4}$$

5.2.2 Model for the Scattered Field

Let $E^{sc}(\mathbf{x},t)$ denote the scattered field. Using the Born approximation, the scattered field is then modeled as

$$\begin{aligned}E^{sc}(\mathbf{y},t) = \int & \frac{\delta(t-t'-|\mathbf{y}-\mathbf{z}|/c_0)}{4\pi|\mathbf{y}-\mathbf{z}|} V(\boldsymbol{\alpha}(\mathbf{z},t')) \\ & \times \frac{\delta(t'-t''-|\mathbf{z}-\boldsymbol{\gamma}_T(t'')|/c_0)}{4\pi|\mathbf{z}-\boldsymbol{\gamma}_T(t'')|} \ddot{p}(t'')\, dt'dt''d\mathbf{z}.\end{aligned} \tag{5.5}$$

Let $\boldsymbol{\gamma}_R(t)$ denote the trajectory of the receiver at time t. The received signal $r(t)$ is

$$\begin{aligned}r(t) = E^{sc}(\boldsymbol{\gamma}_R(t),t) = \int & \frac{\delta(t-t'-|\boldsymbol{\gamma}_R(t)-\mathbf{z}|/c_0)}{4\pi|\boldsymbol{\gamma}_R(t)-\mathbf{z}|} V(\boldsymbol{\alpha}(\mathbf{z},t')) \\ & \times \frac{\delta(t'-t''-|\mathbf{z}-\boldsymbol{\gamma}_T(t'')|/c_0)}{4\pi|\mathbf{z}-\boldsymbol{\gamma}_T(t'')|} \ddot{p}(t'')\, dt'dt''d\mathbf{z}.\end{aligned} \tag{5.6}$$

Assuming that the waveform is transmitted starting at time s, the wave is emitted from the transmitter at time $s+t''$, for $t'' \in [0,T]$, reaches the target at time $s+t'$, and arrives at the receiving antenna at time $s+t$. Note that t'', t', and t are relative time variables within the interval that starts at time s. Thus, for this short time interval, we have

$$\begin{aligned}r(s+t) = \int & \frac{\delta(t-t'-|\boldsymbol{\gamma}_R(s+t)-\mathbf{z}|/c_0)}{4\pi|\boldsymbol{\gamma}_R(s+t)-\mathbf{z}|} V(\boldsymbol{\alpha}(\mathbf{z},s+t')) \\ & \times \frac{\delta(t'-t''-|\mathbf{z}-\boldsymbol{\gamma}_T(s+t'')|/c_0)}{4\pi|\mathbf{z}-\boldsymbol{\gamma}_T(s+t'')|} \ddot{p}(s+t'')\, dt'dt''d\mathbf{z}.\end{aligned} \tag{5.7}$$

Making the change of variables

$$\mathbf{z} \to \mathbf{x} = \boldsymbol{\alpha}(\mathbf{z},t) = \boldsymbol{\Gamma}^{-1}(\mathbf{z},t), \tag{5.8}$$

we obtain

$$\begin{aligned}r(s+t) = \int & \frac{\delta(t-t'-|\boldsymbol{\gamma}_R(s+t)-\boldsymbol{\Gamma}(\mathbf{x},s+t')|/c_0)}{4\pi|\boldsymbol{\gamma}_R(s+t)-\boldsymbol{\Gamma}(\mathbf{x},s+t')|} V(\mathbf{x})|\nabla_{\mathbf{x}}\boldsymbol{\Gamma}(\mathbf{x},s+t')| \\ & \times \frac{\delta(t'-t''-|\boldsymbol{\Gamma}(\mathbf{x},s+t')-\boldsymbol{\gamma}_T(s+t'')|/c_0)}{4\pi|\boldsymbol{\Gamma}(\mathbf{x},s+t')-\boldsymbol{\gamma}_T(s+t'')|} \ddot{p}(s+t'')\, dt'dt''d\mathbf{x}.\end{aligned} \tag{5.9}$$

Assuming the targets follow a linear motion

$$\boldsymbol{\Gamma}(\mathbf{x},t) \approx \mathbf{x} + \mathbf{v}_{\mathbf{x}} t, \tag{5.10}$$

then $|\nabla_{\mathbf{x}}\boldsymbol{\Gamma}(\mathbf{x}, s+t')| \approx 1$. Additionally, substituting $V(\mathbf{x}) = \rho(\boldsymbol{x})\delta(x3 - \psi(\boldsymbol{x}))$, we obtain

$$\begin{aligned} r(s+t) = \int & \frac{\delta(t - t' - |\boldsymbol{\gamma}_R(s+t) - (\mathbf{x} + \mathbf{v}_{\mathbf{x}}(s+t'))|/c_0)}{4\pi|\boldsymbol{\gamma}_R(s+t) - (\mathbf{x} + \mathbf{v}_{\mathbf{x}}(s+t'))|}\rho(\boldsymbol{x}) \\ & \times \frac{\delta(t' - t'' - |\mathbf{x} + \mathbf{v}_{\mathbf{x}}(s+t') - \boldsymbol{\gamma}_T(s+t'')|/c_0)}{4\pi|\mathbf{x} + \mathbf{v}_{\mathbf{x}}(s+t') - \boldsymbol{\gamma}_T(s+t'')|}\ddot{p}(s+t'')\, dt' dt'' d\boldsymbol{x}. \end{aligned} \tag{5.11}$$

We now make the approximations

$$\boldsymbol{\gamma}_R(s+t) \approx \boldsymbol{\gamma}_R(s) + \dot{\boldsymbol{\gamma}}_R(s)t, \tag{5.12}$$

$$\boldsymbol{\gamma}_T(s+t'') \approx \boldsymbol{\gamma}_T(s) + \dot{\boldsymbol{\gamma}}_T(s)t'', \tag{5.13}$$

and the far field approximations $|\boldsymbol{\gamma}_R(s) - \mathbf{x} - \mathbf{v}_{\mathbf{x}} s| \gg |\dot{\boldsymbol{\gamma}}_R(s)t - \mathbf{v}_{\mathbf{x}} t'|$ and $|\mathbf{x} + \mathbf{v}_{\mathbf{x}} s - \boldsymbol{\gamma}_T(s)| \gg |\mathbf{v}_{\mathbf{x}} t' - \dot{\boldsymbol{\gamma}}_T(s)t''|$ to obtain

$$\begin{aligned} |\boldsymbol{\gamma}_R(s+t) - (\mathbf{x} + \mathbf{v}_{\mathbf{x}}(s+t'))| \approx {} & |\boldsymbol{\gamma}_R(s) - \mathbf{x} - \mathbf{v}_{\mathbf{x}} s| \\ & + (\widehat{\boldsymbol{\gamma}_R(s) - \mathbf{x} - \mathbf{v}_{\mathbf{x}} s}) \cdot (\dot{\boldsymbol{\gamma}}_R(s)t - \mathbf{v}_{\mathbf{x}} t') \end{aligned} \tag{5.14}$$

$$\begin{aligned} |\mathbf{x} + \mathbf{v}_{\mathbf{x}}(s+t') - \boldsymbol{\gamma}_T(s+t'')| \approx {} & |\mathbf{x} + \mathbf{v}_{\mathbf{x}} s - \boldsymbol{\gamma}_T(s)| \\ & + (\widehat{\mathbf{x} + \mathbf{v}_{\mathbf{x}} s - \boldsymbol{\gamma}_T(s)}) \cdot (\mathbf{v}_{\mathbf{x}} t' - \dot{\boldsymbol{\gamma}}_T(s)t''). \end{aligned} \tag{5.15}$$

Furthermore, we make a small scene assumption and short aperture assumption so that $|\boldsymbol{\gamma}_R(s) - \mathbf{x}| \gg |\mathbf{x}|$ and $(\widehat{\boldsymbol{\gamma}_R(s) - \mathbf{x}}) \approx (\widehat{\boldsymbol{\gamma}_R(s_0) - \mathbf{x}})$. Then the antenna look direction is written as

$$(\widehat{\boldsymbol{\gamma}_R(s) - \mathbf{x} - \mathbf{v}_{\mathbf{x}} s}) \approx (\widehat{\boldsymbol{\gamma}_R(s_0) - \mathbf{x}_0}), \tag{5.16}$$

and if we define the origin of the coordinate system at $\mathbf{x}_0$, then we simply write $\widehat{\boldsymbol{\gamma}_R(s_0)}$.

Using (5.12)-(5.16) and performing the t' and t'' we obatin

$$r(s+t) = \int \frac{\ddot{p}(s+\alpha_{RT}t-\tau_{RT})\rho(\boldsymbol{x})}{G_R(s,\mathbf{x})G_T(s,\mathbf{x})}\, d\boldsymbol{x}, \tag{5.17}$$

where

$$\alpha_{RT} = \frac{1-\widehat{\boldsymbol{\gamma}_R(s_0)}\cdot\dot{\boldsymbol{\gamma}}_R(s)/c_0}{1+\widehat{\boldsymbol{\gamma}_T(s_0)}\cdot\dot{\boldsymbol{\gamma}}_T(s)/c_0}\cdot\frac{1+\widehat{\boldsymbol{\gamma}_T(s_0)}\cdot\mathbf{v}_{\mathbf{x}}/c_0}{1-\widehat{\boldsymbol{\gamma}_R(s_0)}\cdot\mathbf{v}_{\mathbf{x}}/c_0}, \tag{5.18}$$

$$\begin{aligned}\tau_{RT} =& |\boldsymbol{\gamma}_R(s)-(\mathbf{x}+\mathbf{v}_{\mathbf{x}}s)|/c_0 + |\boldsymbol{\gamma}_T(s)-(\mathbf{x}+\mathbf{v}_{\mathbf{x}}s)|/c_0 \\ &+ (\widehat{\boldsymbol{\gamma}_R(s_0)}+\widehat{\boldsymbol{\gamma}_T(s_0)})\cdot\mathbf{v}_{\mathbf{x}}s/c_0,\end{aligned} \tag{5.19}$$

and $G_R(s,\mathbf{x})$ and $G_T(s,\mathbf{x})$ are the geometric spreading terms for the receiver and transmitter, respectively. With the start-stop approximation for the motion between target and transmitter, we have

$$\alpha_R = \frac{1-\widehat{\boldsymbol{\gamma}_R(s_0)}\cdot\dot{\boldsymbol{\gamma}}_R(s_0)/c_0}{1-\widehat{\boldsymbol{\gamma}_R(s_0)}\cdot\mathbf{v}_{\mathbf{x}}/c_0}. \tag{5.20}$$

For an ultra-narrowband waveform we model the signal as

$$p(t) = \tilde{p}(t)e^{i\omega_0 t}, \tag{5.21}$$

where $\tilde{p}(t)$ is the slowly varying envelope and ω_0 the carrier frequency. Substituting (5.21) into (5.17) we obatin

$$r(s+t) = \omega_0^2 \int \frac{\tilde{p}(s+\alpha_R t-\tau_{RT})e^{i\omega_0(s+\alpha_R t-\tau_{RT})}\rho(\boldsymbol{x})}{G_R(s,\mathbf{x})G_T(s,\mathbf{x})}\, d\boldsymbol{x}. \tag{5.22}$$

5.2.3 Cross-Receiver Correlation

Let $f_i(s,t)$ denote the received signal for the receiver located at $\boldsymbol{\gamma}_i(s)$. We correlated, scale, and window corresponding "data processing intervals" of received data at two different antenna positions to form the data

$$d_{ij}(s,\mu) = \int f_i(s,t) f_j^*(s,\mu t)\phi(t)\, dt, \tag{5.23}$$

where $\phi(t)$ is a smooth windowing function of finite support. Substituting (5.22) into (5.23) we obatin

$$\begin{aligned} d_{ij}(s,\mu) = \omega_0^4 \int & \frac{e^{i\omega_0(s+\alpha_i t-\tau_{iT})} e^{-i\omega_0(s+\alpha_j \mu t-\tau_{jT})}}{G_{ij}(s,\mathbf{x},\mathbf{v}_{\mathbf{x}})} \\ & \times \tilde{p}(s+\alpha_i t-\tau_{iT})\rho(\boldsymbol{x})\tilde{p}(s+\alpha_j t-\tau_{jT})\rho(\boldsymbol{x}')\, d\boldsymbol{x} d\boldsymbol{x}' dt. \end{aligned} \tag{5.24}$$

We assume $\tilde{p}(\mu t) \approx \tilde{p}(t)$ since $\tilde{p}(t)$ is a slowly-varying function of time. Additionally, we use the incoherent field approximation

$$E[\rho(\boldsymbol{x})\rho(\boldsymbol{x}')] \approx R_\rho(\boldsymbol{x})\delta(\boldsymbol{x}-\boldsymbol{x}') \tag{5.25}$$

and take the expected value of the correlation to write

$$\begin{aligned} d_{ij}(s,\mu) &= \omega_0^4 \int e^{i\omega_0[s+\alpha_i\alpha_T t-\tau_{iT}]} e^{-i\omega_0[s+\alpha_j\alpha_T\mu t-\tau_{jT}]} \tilde{A}_{ij}(s,\boldsymbol{x},\boldsymbol{v}_{\mathbf{x}}) R_\rho(\boldsymbol{x})\, d\boldsymbol{x} dt \\ &= \omega_0^4 \int e^{i\omega_0[(\alpha_i-\alpha_j\mu)\alpha_T t-\tau_{ij}]} \tilde{A}_{ij}(s,\boldsymbol{x},\boldsymbol{v}_{\mathbf{x}}) R_\rho(\boldsymbol{x})\, d\boldsymbol{x} dt. \end{aligned} \tag{5.26}$$

We now define the *phase-space radiance function* as

$$r(\boldsymbol{x},\boldsymbol{v}) = R_\rho(\boldsymbol{x})\delta(\boldsymbol{v}-\boldsymbol{v}_{\boldsymbol{x}}), \tag{5.27}$$

and we combine the ω_0^4 and $e^{i\omega_0\tau_{ij}}$ terms with the amplitude and define the forward operator as

$$\begin{aligned} \mathcal{F}_{ij}[r](s,\mu) &:= d(s,\mu) \\ &= \int e^{i\omega_0 t[(\alpha_i-\alpha_j\mu)]} A_{ij}(s,\boldsymbol{x},\boldsymbol{v}) r(\boldsymbol{x},\boldsymbol{v})\, d\boldsymbol{x} d\boldsymbol{v} dt. \end{aligned} \tag{5.28}$$

5.2.4 Analysis of Forward Model

The critical set, defined by $(\boldsymbol{x},\boldsymbol{v})$ where $\partial_t\phi(\mathbf{x},\mathbf{v},s,t,\mu)=0$, or

$$\omega_0(\alpha_i-\alpha_j\mu) = 0, \tag{5.29}$$

is

$$\{(\boldsymbol{x}, \boldsymbol{v}) \in \mathbb{R}^2 \times \mathbb{R}^2 : S_{ij} = \mu\}, \tag{5.30}$$

where

$$\begin{aligned} S_{ij}(s, \mathbf{x}, \mathbf{v}) &= \frac{\alpha_i(s, \mathbf{x}, \mathbf{v})}{\alpha_j(s, \mathbf{x}, \mathbf{v})} \\ &= \frac{1 - \widehat{\boldsymbol{\gamma}_i(s_0)} \cdot \dot{\boldsymbol{\gamma}}_i(s)/c_0}{1 - \widehat{\boldsymbol{\gamma}_i(s_0)} \cdot \mathbf{v}/c_0} \cdot \frac{1 - \widehat{\boldsymbol{\gamma}_j(s_0)} \cdot \mathbf{v}/c_0}{1 - \widehat{\boldsymbol{\gamma}_j(s_0)} \cdot \dot{\boldsymbol{\gamma}}_j(s)/c_0}. \end{aligned} \tag{5.31}$$

This manifold defines the iso-Doppler contours that indicate what information is obtained from the forward model.

5.3 Image Formation

Since the data from the forward model is two-dimensional and the hitchhiker iso-Doppler contours are four-dimensional, we may not be able to backproject to this manifold such that the point spred function is focused in both the position and velocity spaces. Similarly to the wideband case of synthetic aperture hitchhiker imaging of ground moving targets, in order to form a radiance image, we backproject onto iso-Doppler contours for a hypothesized target velocity, $\boldsymbol{v}_h$.

5.3.1 Filtered Backprojection Operator

For a given hypothesized velocity $\boldsymbol{v}_h$, we define The filtered backprojection image formation operator is now defined for the $(i, j)^{\text{th}}$ pair of receivers as

$$\begin{aligned} \mathcal{K}_{ij}[d](\boldsymbol{x}') &:= \hat{r}_{ij}^{\boldsymbol{v}_h}(\boldsymbol{x}') \\ &= \int e^{-i\omega_0 t[(\alpha_i - \alpha_j \mu)]} Q_{ij}(s, \boldsymbol{x}', \boldsymbol{v}_h) d_{ij}(s, \mu)\, dt ds d\mu, \end{aligned} \tag{5.32}$$

where $Q_{ij}(s, \boldsymbol{x}', \boldsymbol{v}_h)$ is the filter to be determined. To form the final $\boldsymbol{v}_h$-radiance image, we sum the reconstructed images from all pairs of receivers as

$$\hat{r}^{\boldsymbol{v}_h}(\boldsymbol{x}') = \sum_{i,j} \hat{r}_{ij}^{\boldsymbol{v}_h}(\boldsymbol{x}'). \tag{5.33}$$

5.3.2 Analysis of the Point Spread Function

Plugging in (5.28) into (5.32) we obtain the image fidelity operator

$$\mathcal{K}_{ij}\mathcal{F}_{ij}[r](\boldsymbol{x}') = \int L_{\boldsymbol{v}}^{\boldsymbol{v}_h}(\boldsymbol{x}, \boldsymbol{x}') r(\boldsymbol{x}, \boldsymbol{v}) \, d\boldsymbol{x} d\boldsymbol{v} \tag{5.34}$$

where

$$\begin{aligned} L_{\boldsymbol{v}}^{\boldsymbol{v}_h}(\boldsymbol{x}, \boldsymbol{x}') = \int & e^{-i\omega_0 t'[(\alpha_i(s,\mathbf{x}',\mathbf{v}_h) - \alpha_j(s,\mathbf{x}',\mathbf{v}_h)\mu)]} e^{i\omega_0 t[(\alpha_i(s,\mathbf{x},\mathbf{v}) - \alpha_j(s,\mathbf{x},\mathbf{v})\mu)]} \\ & \times Q_{ij}(s, \boldsymbol{x}', \boldsymbol{v}_h) A_{ij}(s, \boldsymbol{x}, \boldsymbol{v}) \, dt' dt ds d\mu \end{aligned} \tag{5.35}$$

is the point spread function. Performing the $d\mu$ integration yields

$$t' = t \frac{\alpha_j(s, \mathbf{x}, \mathbf{v})}{\alpha_j(s, \mathbf{x}', \mathbf{v}_h)}. \tag{5.36}$$

Plugging back into the point spread function, we obtain

$$L_{\boldsymbol{v}}^{\boldsymbol{v}_h}(\boldsymbol{x}, \boldsymbol{x}') = \int e^{-i\Phi(\omega_0, t, s, \mathbf{x}, \mathbf{v}, \mathbf{x}', \mathbf{v}_h)} Q_{ij}(s, \boldsymbol{x}', \boldsymbol{v}_h) A_{ij}(s, \boldsymbol{x}, \boldsymbol{v}) \, dt' dt ds d\mu, \tag{5.37}$$

where

$$\Phi(\omega_0, t, s, \mathbf{x}, \mathbf{v}, \mathbf{x}', \mathbf{v}_h) = \omega_0 t \left[\frac{\alpha_j(s, \mathbf{x}, \mathbf{v})}{\alpha_j(s, \mathbf{x}', \mathbf{v}_h)} \alpha_i(s, \mathbf{x}', \mathbf{v}_h) - \alpha_i(s, \mathbf{x}, \mathbf{v}) \right]. \tag{5.38}$$

According to the Hörmander-Sato theorem, the main contributions to the point spread function of the image fidelity operator come from the critical set of the phase, which satisfy the conditions

$$\partial_t \Phi(\omega_0, t, s, \mathbf{x}, \mathbf{v}, \mathbf{x}', \mathbf{v}_h) = 0 \tag{5.39}$$

$$\partial_s \Phi(\omega_0, t, s, \mathbf{x}, \mathbf{v}, \mathbf{x}', \mathbf{v}_h) = 0. \tag{5.40}$$

From (5.38), we can see that when the hypothesized velocity $\mathbf{v}_h$ equals the true velocity $\mathbf{v}_{\mathbf{x}}$, one of the solutions to the critical set conditions is $\mathbf{x}' = \mathbf{x}$, so the scatterer is positioned at the correct location in the reconstructed image.

5.3.3 Determination of the Filter

We design the filter so that the point spread function of the image fidelity operator (5.34) is approximately a Dirac delta function. We write this as

$$L_{\boldsymbol{v}}^{\boldsymbol{v}_h}(\boldsymbol{x}, \boldsymbol{x}') \approx \int_{\Omega_{ij}} e^{i\boldsymbol{\xi}_{ij}\cdot(\boldsymbol{x}-\boldsymbol{x}')}\, d\boldsymbol{\xi}_{ij}, \tag{5.41}$$

where Ω_{ij} is the data collection manifold for the imaging geometry. To determine $\boldsymbol{\xi}_{ij}$, we make a Taylor series approximation in the phase about the point $(\boldsymbol{x} - \boldsymbol{x}')$, so that

$$\Phi(\omega_0, t, s, \mathbf{x}, \mathbf{v}, \mathbf{x}', \mathbf{v}_h) \approx \nabla_{\boldsymbol{x}}\Phi(\omega_0, t, s, \mathbf{x}, \mathbf{v}, \mathbf{x}', \mathbf{v}_h)|_{\boldsymbol{x}=\boldsymbol{x}'} \cdot (\boldsymbol{x} - \boldsymbol{x}') \tag{5.42}$$

and

$$\boldsymbol{\xi}_{ij} = \nabla_{\boldsymbol{x}}\Phi(\omega_0, t, s, \mathbf{x}, \mathbf{v}, \mathbf{x}', \mathbf{v}_h)|_{\boldsymbol{x}=\boldsymbol{x}'}. \tag{5.43}$$

Finally, the filter $Q_{ij}(s, \boldsymbol{x}', \boldsymbol{v}_h)$ becomes

$$Q_{ij}(s, \boldsymbol{x}', \boldsymbol{v}_h) = \frac{A_{ij}^*(s, \boldsymbol{x}', \boldsymbol{v}_h)}{\eta_{ij}(s, \boldsymbol{x}', \boldsymbol{v}_h)|A_{ij}(s, \boldsymbol{x}', \boldsymbol{v}_h)|^2} \tag{5.44}$$

where η_{ij} is the Jacobian that comes from the change of variables $(t, s) \to \boldsymbol{\xi}_{ij}$.

5.4 Numerical Simulations

Numerical simulations were performed in order to demonstrate the method described in the previous section and its performance. The size of the simulated scene is 2048 × 2048 meters, discretized into 256 × 256 pixels. The scene coordinates used place the origin at the center, so that the scene goes from -1024 meters to +1024 meters in each dimension. The antennas travel in a circular aperture of radius 6000 meters at a speed of 200 m/s and altitude of 1000 meters. The antennas traverse 45° of the trajectory, discretized into 2048 samples.

The transmitter is a stationary tower located at $(4000, -4000)$ meters relative to the center of the scene, at an altitude of 500 meters. We simulate a single frequency waveform at 100 MHz.

5.4.1 Single Moving Target

This simulation uses a single moving target positioned at $(-200, 500)$, traveling at 6 m/s at an angle of $-50°$ from the x-axis. The original scene is showed in Figure 5.1, and the reconstructed image for a hypothesized velocity of 0 m/s is shown in Figure 5.2. Similarly to the wideband case, the target is smeared as a result of the incorrect velocity hypothesis. As the target moves over the length of data collection, the displacement from its original location grows, causing the smearing. When we constructed with the true velocity, we obtain the focused point shown in Figure 5.3. Finally, we look at the stack of images formed over the range of hypothesized velocities from -10 to 10 m/s in each of the x and y-directions. The entropy map is shown in Figure 5.4, and the minimum entropy point is at the velocity of $(3, -5)$ m/s, which is very close to the true velocity of $(4, -5)$ m/s.

5.4.2 Multiple Moving Targets

The multiple moving target simulation contains three point targets: one stationary target located at $(-400, -400)$, one moving target located at $(-200, 500)$ traveling at 6 m/s at $-50°$ from the positive x-axis with components of $(3.9, -4.6)$ m/s, and one moving target located at $(400, -300)$ traveling at 12 m/s at 280° from the positive x-axis with components of $(2.1, -11.8)$ m/s. A stack of images was reconstructed over the range of hypothesized velocities from -13 to 13 m/s in each direction at steps of 1 m/s. The entropy map is shown in Figure 5.6. The three minimum points of the entropy map, in increasing order, correspond to the velocities of $(0, 0)$ m/s, $(3, -5)$ m/s, and $(3, -11)$ m/s. Figure 5.7 shows the reconstructed image for the hypothesized velocity of $(0, 0)$. In this image, we can see that the stationary target in the bottom left is focused, while the other two targets are smeared. Figure 5.8 shows the reconstructed image for the hypothesized velocity of $(3, -5)$. In this

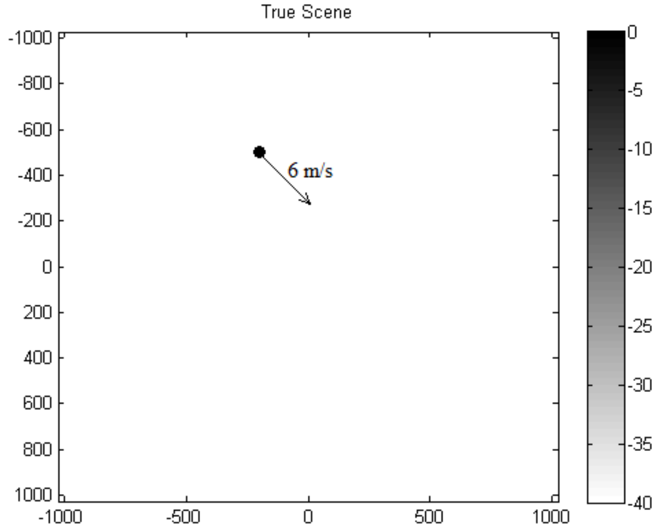

Figure 5.1: The original scene for the single moving target simulation. there is one target moving at a velocity of 6 m/s traveling towards the bottom right of the scene at an angle of -50° from the positive x-axis.

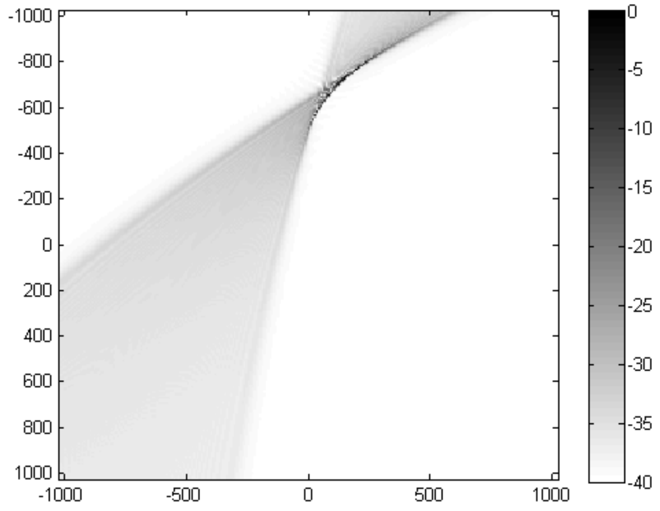

Figure 5.2: Reconstructed scene for simulation 1 with zero hypothesized velocity. The target is smeared and mispositioned as a result of the incorrect hypothesized velocity.

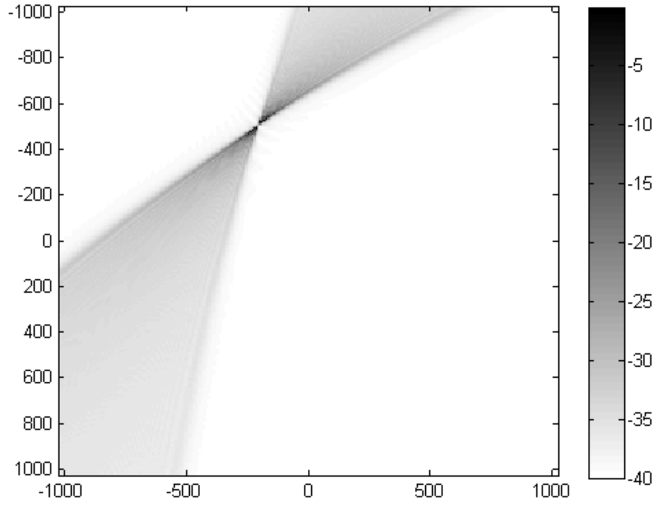

Figure 5.3: **Reconstructed scene with the hypothesized velocity set to the true velocity. Here, the target is both focused and located at the correct position in the reconstructed image.**

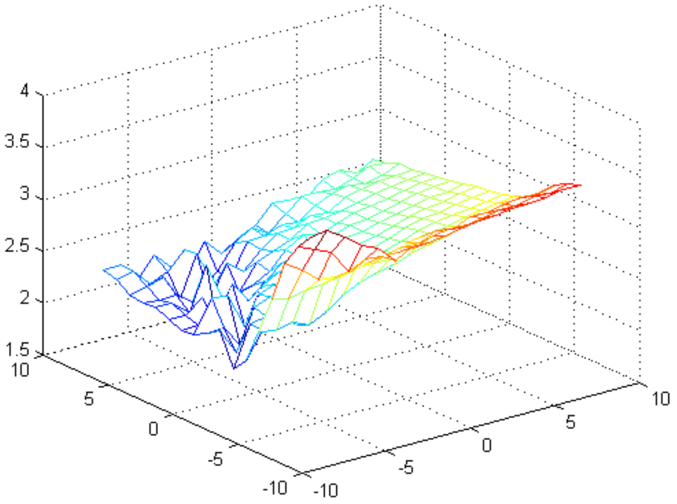

Figure 5.4: **Entropy map over the range of two-dimensional hypothesized velocities. The minimum point is at the velocity of $(3, -5)$ m/s.**

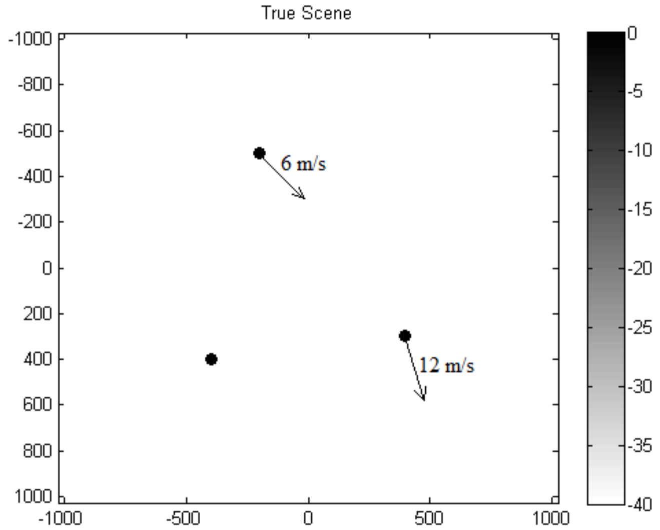

Figure 5.5: The original scene for the single moving target simulation. there is one target moving at a velocity of 6 m/s traveling towards the bottom right of the scene at an angle of $-50°$ from the positive x-axis.

image, we can see that the moving target at the top of the scene, while the other two targets are smeared. Finally, Figure 5.9 shows the reconstructed image for the hypothesized velocity of $(3, -11)$. In this image, the moving target in the bottom right of the scene is most focused, while the other two targets are smeared.

5.5 Conclusion

In this chapter we developed the method for Doppler hitchhiker imaging of ground moving targets. This method relies on sources of opportunity that use ultra-narrowband waveforms. These waveforms are quite common among available illuminators of opportunity, and since they are unsuitable for use with conventional SAR imaging approaches that rely on range information, special methods must be employed to take advantage of these signals.

High resolution images are formed with ultra-narrowband waveforms by measuring Doppler shift in the received signal, and backprojecting to iso-Doppler contours instead of the iso-range contours commonly used in conventional SAR. Since these waveforms are long in duration and very narrow in frequency, the iso-Doppler

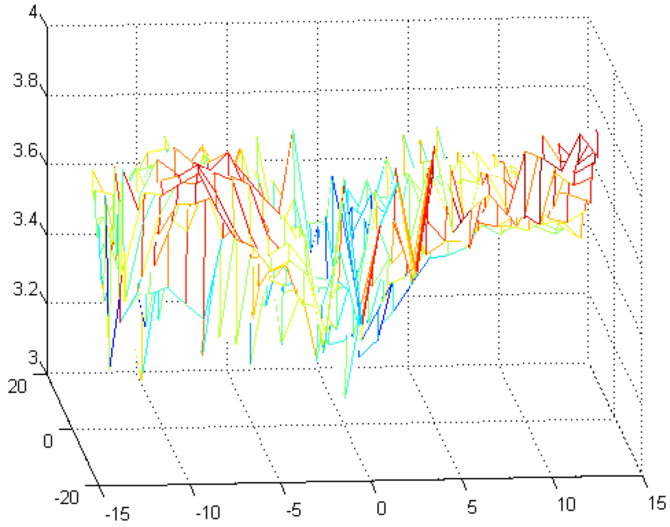

Figure 5.6: Entropy map over the range of two-dimensional hypothesized velocities. The minimum point is at the velocity of $(3, -5)$ m/s.

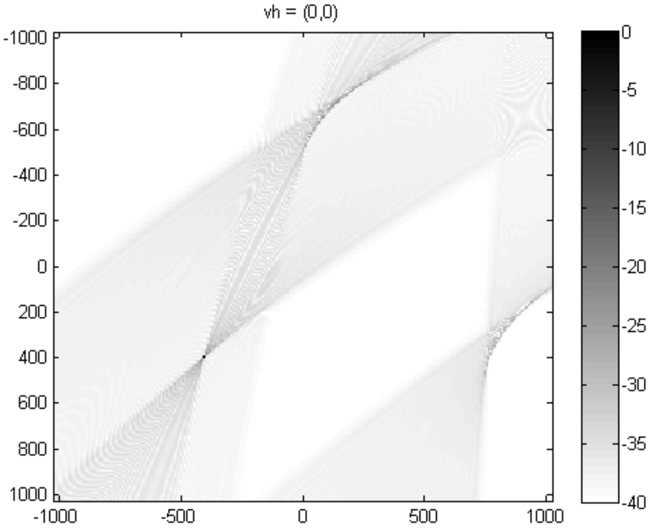

Figure 5.7: Reconstructed scene for simulation 1 with zero hypothesized velocity. The target is smeared and mispositioned as a result of the incorrect hypothesized velocity.

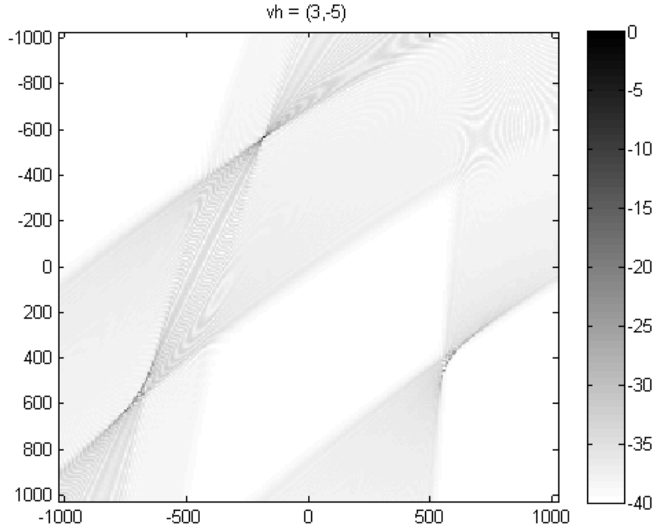

Figure 5.8: Reconstructed scene with the hypothesized velocity set to the true velocity. Here, the target is both focused and located at the correct position in the reconstructed image.

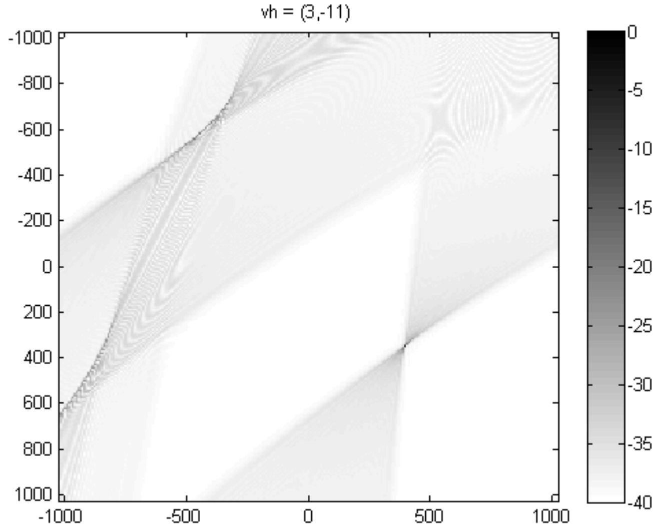

Figure 5.9: Reconstructed scene with the hypothesized velocity set to the true velocity. Here, the target is both focused and located at the correct position in the reconstructed image.

contours have the high resolution that contributes to a focused reflectivity image. We first develop a novel forward model where the received signals at pairs of receivers are correlated, which measures the ratio of Doppler scale factors between the two receivers. This allows backprojection without knowledge of the transmitter location or waveform. We demonstrate in numerical simulations how this type of backprojection yields focused images for a correct hypothesized velocity and how entropy can be used as measure of focus for velocity estimation.

As with the wideband case of hitchhiker ground moving target imaging, this method does not explicitly take clutter into account. Therefore, clutter suppression techniques must be employed in conjunction with this method. In the next chapter, we develop the theory for how the well-known displaced phase center antenna and along-track interferometry techniques for conventional SAR can be applied to the case of Doppler-SAR, where we use ultra-narrowband waveforms.

CHAPTER 6
Two-Channel Doppler SAR Imaging of Ground Moving Targets

6.1 Introduction

In this chapter we present a theory for performing moving target synthetic aperture radar (SAR) imaging with two-channel clutter suppression by combining the displaced phase center antenna (DPCA) and along-track interferometry (ATI) techniques with Doppler SAR.

DPCA and ATI are well-studied methods for suppressing clutter and detecting moving targets with two receiver channels. These approaches involve placing the two receiving antenna phase centers sufficiently far apart along a flight path, so that the second antenna passes through the same location as the first antenna after an integral number of pulses. The two received signals will then be the same for all stationary scatterers. DPCA and ATI take advantage of the similarity between the two sets of data by subtracting and multiplying complex conjugates, respectively.

In this chapter, we combine these two-channel clutter suppression techniques, DPCA and ATI, with Doppler-SAR (DSAR), which has the advantages stated in the previous chapter, notably the application to passive synthetic aperture radar. We first show that with conventional radar, the signals at two receivers differ by a range-rate term in the phase, nonzero only for moving targets. Section 6.3 shows that under a certain set of constraints, in DSAR, the two signals at different receivers differ only by a Doppler-rate term in the phase. Subtracting the signals eliminates the stationary clutter component of the scattered signal, and the moving target information can be extracted from this differential Doppler term.

Portions of this chapter to appear in: S. Wacks and B. Yazici, "Bistatic Doppler-SAR DPCA imaging of ground moving targets," *IEEE Proc. Radar Conf.*, Cincinnati, OH, 2014.

6.1.1 Overview of DPCA and ATI

When observing a scene of interest from an airborne platform, special complications arise with moving targets that do not otherwise need to be considered for the case of a stationary antenna. For a stationary antenna, the only Doppler shifts in the received signal are those from target motion, but with a moving antenna, the majority of clutter (stationary) scatterers are now moving with respect to the antenna. Therefore, each scatterer will induce a different Doppler shift, depending on the angle between it and the antenna velocity. The literature calls this effect a spreading of the clutter Doppler spectrum, since it spreads from an essentially zero-width spike at zero-Doppler, to a wider area related to the bandwidth of the signal and speed of the antenna.

One of the earliest and most successful methods for mitigating this moving platform effect is the so called displaced phase center antenna (DPCA) technique [1], [92], [93]. This approach relies on two receiving antenna channels spaced sufficiently far apart (traditionally 1-2 pulse repetition intervals) in the same direction as the platform motion using the same beam pattern and look direction. This allows the second antenna to pass through the exact same spot as the first antenna an integral number of pulses later, allowing it to have the same received signal for all stationary scatterers. By subtracting the two signals at the appropriate time delay, all that is left is the response from moving targets in the scene.

Along-track interferometry (ATI) is a well known technique for clutter suppression and velocity estimation of moving targets. Two antenna phase centers are place on either a single or a second moving platform that passes through the location of the first platform after a time delay. This allows two data sets created via the same imaging geometry, but at different times. This time difference allows the dynamic properties of the scene of interest, such as moving target information, to be captured, but the stationary ground clutter remains constant. ATI relies on the phase difference between two images by multiplying one image with the complex conjugates of the other one [93]-[95].

6.1.2 Literature Survey

Multichannel approaches to radar, and specifically the DPCA technique, date back to the 1950s. In [1], a detailed history of this development is presented, and credits GE with the initial invention in 1952. GE showed that subtracting two received signals at a proper time delay or azimuth shift canceled much of the clutter signal.

[92] is an early work that explores some of the more theoretical aspects of DPCA. In this paper, the authors compare DPCA to the more generic space-time adaptive processing (STAP) for both airborne and space-based radar systems. It is known that STAP can be more optimal in most situations by taking advantage of prior information and more receiver channels, but it suffers from higher computational complexity, and the required target-free prior clutter information is not always available. The paper details pros and cons of the two techniques on the basis of antenna complexity, computational complexity, and target attenuation. The fundamental concepts in STAP are more fully discussed in [96], a key paper from 1999.

Another technique that takes advantage of the phase difference between channels resulting from moving targets is along-track interferometry (ATI). This technique was first developed in [97] for the purpose of estimating ocean currents, but it can be applied to ground moving targets in the same way. ATI operates by subtracting the phase instead of the magnitude of the two channels, by multiplying together complex conjugates of the individual images.

A summary and comparison of both the DPCA and ATI techniques is described in [98]. In [98], simulations are performed using each technique under difference noise and clutter levels. The authors conclude that DPCA performance can be affected by high levels of noise, while ATI is relatively robust under these circumstances. Another paper that considers both methods is [99]. In this paper the authors develop a moving target detection and velocity estimation method that helps to overcome the problem of ambiguous velocities. The data is split into multiple subbands, and ATI follows a DPCA step for each subband. Since each subband is based off a different center frequency, the interferograms yield different ranges of velocities, eliminating many velocity estimation ambiguities. In [93], the authors describe how DPCA and ATI mitigate the response from different types of clutter. From this conclusion, the authors present a hybrid method that multiplies the thresholded ATI image with the DPCA image in order to cancel both types of clutter.

The effectiveness of the DPCA technique has been demonstrated experimentally numerous times, both in simulation and on real data. For example, in [100], after presenting the background theory of DPCA along with predicted clutter suppression levels, the technique is performed on C-band radar to provide up to 23 dB of clutter cancellation. In preparation for Canada's RADARSAT-2 satelite, [101] presents preliminary, but promising results for DPCA clutter suppression on simulated data. The parameters that were chosen were assumed to be close to those of the RADARSAT-2 system. In [102], using the RADARSAT-2 system, clutter cancellation is performed on the raw, azimuth-uncompressed data instead of SAR images. This paper shows promising results and indicates that by performing the technique on the raw data, information loss associated with fast-moving objects is avoided. Additionally, the ATI technique has been demonstrated with success in [103]. This experiment shows the robustness and of ATI and is able to detect slow moving targets in a noisy environment.

6.2 Clutter Cancellation for a Point Target Using Two-Channel Wideband SAR

In order to compare the results of the two-channel Doppler-SAR techniques, we briefly summarize the main conclusions for the conventional case. Note that in conventional radar, signals are assumed to be relatively wideband. The information contained in the phase of the forward model is related to the range or time delay of the scatterers.

We consider two receiving antenna phase centers collecting data at positions $\boldsymbol{\gamma}_R^1(s)$ and $\boldsymbol{\gamma}_R^2(s)$ and a stationary transmitter located at $\boldsymbol{\gamma}_T$. We assume that at time $s + \Delta s$ the second antenna passes through the location of the first antenna at time s with the same velocity. Therefore, $\boldsymbol{\gamma}_R^1(s) = \boldsymbol{\gamma}_R^2(s + \Delta s)$ and $\dot{\boldsymbol{\gamma}}_R^1(s) = \dot{\boldsymbol{\gamma}}_R^2(s + \Delta s)$.

The model for the received signal at the n^{th} antenna from a point target at location $\mathbf{x}_0$ as

$$f^n(s,t) = \int e^{i\omega[t-R^n(s,\mathbf{x}_0)/c_0-\mathbf{L}^n(s,\mathbf{x}_0)\cdot\mathbf{v}_0 s/c_0]} \times A(\omega,s,\boldsymbol{x}_0)\rho(\boldsymbol{x}_0)\,d\omega \tag{6.1}$$

where

$$R^n(s,\mathbf{x}) = |\mathbf{x}+\mathbf{v}_{\mathbf{x}}s-\boldsymbol{\gamma}_R^n(s)| + |\mathbf{x}+\mathbf{v}_{\mathbf{x}}s-\boldsymbol{\gamma}_T| \tag{6.2}$$

$$\mathbf{L}^n(s,\mathbf{x}) = \widehat{(\mathbf{x}+\mathbf{v}_{\mathbf{x}}s-\boldsymbol{\gamma}_R^n(s))} + \widehat{(\mathbf{x}+\mathbf{v}_{\mathbf{x}}s-\boldsymbol{\gamma}_T)} \tag{6.3}$$

and the moving target follows the trajectory $\mathbf{z}(s) = \mathbf{x}_0 + \mathbf{v}_0 s$. The geometry of this configuration is depicted in Figure 6.1. The received signal for the second receiver at a time $s+\Delta s$ is then

$$\begin{aligned} f^2(s+\Delta s,t) &= \int e^{i\omega[t-R^2(s+\Delta s,\mathbf{x}_0)/c_0-\mathbf{L}^2(s+\Delta s,\mathbf{x}_0)\cdot\mathbf{v}_0(s+\Delta s)/c_0]} \\ &\quad \times A(\omega,s,\boldsymbol{x}_0)\rho(\boldsymbol{x}_0)\,d\omega \\ &\approx \int e^{i\omega[t-R^1(s,\mathbf{x}_0)/c_0-\mathbf{L}^1(s,\mathbf{x}_0)\cdot\mathbf{v}_0 s/c_0]} e^{i\omega\mathbf{L}^1(s,\mathbf{x}_0)\cdot\mathbf{v}_0\Delta s/c_0} \\ &\quad \times A(\omega,s,\boldsymbol{x}_0)\rho(\boldsymbol{x}_0)\,d\omega, \end{aligned} \tag{6.4}$$

which takes the same form as the received signal at the first channel with an extra phase shift term $\mathbf{L}^1(s,\mathbf{x})\cdot\mathbf{v}_0\Delta s/c_0$. This extra phase term is viewed as a range-rate, which adds an extra range value to the measurement when multiplied by the extra time Δs.

We then assume a transmitted waveform has frequencies at $\omega = \omega_0 + \omega'$ where ω_0 is the carrier frequency and $\omega_0 \gg \omega'$. Using this approximation, conventional DPCA approximates the extra phase shift by a constant, as done in [93], independent of frequency. So we can write

$$f^2(s+\Delta s,t) \approx e^{-i\omega_0\mathbf{L}^1(s,\mathbf{x}_0)\cdot\mathbf{v}_0\Delta s/c_0} f^1(s,t). \tag{6.5}$$

When the velocity of the target is zero, as in the case with stationary clutter, these signals will be equal. When the velocity of the target is nonzero, the signals differ in phase, which is the basis for clutter suppression and moving target detection in both the DPCA and ATI techniques.

6.3 Forward Model for Two-Channel Doppler SAR

For Doppler-SAR, we assume an ultra-narrowband transmitted waveform. We begin with the received signal model

$$r(t) = \int e^{i\omega_0[t-R(t,\mathbf{x})/c_0]}\tilde{p}(t-R(t,\mathbf{x}))A(\omega_0,t,\mathbf{x})V(\mathbf{x})\,d\mathbf{x}, \tag{6.6}$$

where

$$A(\omega_0,t,\mathbf{x}) = \frac{J_R(\omega_0,t,\mathbf{x})J_T(\omega_0,t,\mathbf{x})}{G_R(t,\mathbf{x})G_T(t,\mathbf{x})}. \tag{6.7}$$

The amplitude term contains the antenna beam pattern parameteres in J_R and J_T and the geometric spreading terms in G_R and G_T. $\tilde{p}(t)$ is the slowly-varying envelope of the transmitted signal $p(t)$, ω_0 is the carrier frequency, and $R(t,\mathbf{x})$ is the bistatic range - the sum of ranges from the transmitter to target and target to receiver.

Additionally, we substitute the ground topography function as

$$\rho(\boldsymbol{x}) = V(\mathbf{x})\delta(x_3-\psi(\boldsymbol{x})) \tag{6.8}$$

to obtain

$$r(t) = \int e^{i\omega_0[t-R(t,\mathbf{x})/c_0]}\tilde{p}(t-R(t,\mathbf{x}))A(\omega_0,t,\boldsymbol{x})\rho(\boldsymbol{x})\,d\boldsymbol{x}. \tag{6.9}$$

We form the data by correlating the received signal with scaled versions of the transmitted signal and obtain

$$\begin{aligned} d(s,\mu) &= \int r(t)p^*(\mu(t-sT))\phi(t-sT)\,dt \\ &= \int e^{i\omega_0[t-R(t,\mathbf{x})/c_0]}e^{-i\omega_0\mu(t-sT)}\tilde{p}^*(\mu(t-sT))\tilde{p}(t-R(t,\mathbf{x})) \\ \times &\quad A(\omega_0,s,\boldsymbol{x})\rho(\boldsymbol{x})\phi(t-sT)\,d\boldsymbol{x}dt, \end{aligned} \tag{6.10}$$

where $\phi(t)$ is a smooth windowing function with $t \in [0,T]$. Next, we make a linearization in the range $R(t,\mathbf{x})$ about $t = sT$

$$\begin{aligned} R(t,\mathbf{x}) &\approx R(sT,\mathbf{x}) + \big[(\widehat{\mathbf{x}+\mathbf{v}sT-\boldsymbol{\gamma}}_R(sT))\cdot(\mathbf{v}-\dot{\boldsymbol{\gamma}}_R(sT)) \\ &\qquad + (\widehat{\mathbf{x}+\mathbf{v}sT-\boldsymbol{\gamma}}_T)\cdot\mathbf{v}\big](t-sT) \\ &= R(sT,\mathbf{x}) + \beta(sT,\mathbf{x},\mathbf{v})(t-sT). \end{aligned} \tag{6.11}$$

To simplify the notation we write $R(sT,\mathbf{x})$ as $R(s,\mathbf{x})$ and $\beta(sT,\mathbf{x},\mathbf{v})$ as $\beta(s,\mathbf{x},\mathbf{v})$. $\beta(s,\mathbf{x},\mathbf{v})$ is then the Doppler shift of the received signal due to both the moving receiver and the moving target. Substituting into (6.10) we obtain

$$\begin{aligned} d(s,\mu) = \int & e^{i\omega_0 t[(1-\mu)-\beta(s,\mathbf{x},\mathbf{v})]}e^{-i\omega_0 R(s,\mathbf{x})/c_0]}e^{i\omega_0\mu sT}e^{i\omega_0 sT\beta(s,\mathbf{x},\mathbf{v})} \\ & \times \tilde{p}^*(\mu(t-sT))\tilde{p}(t-R(t,\mathbf{x}))A(\omega_0,s,\boldsymbol{x})\rho(\boldsymbol{x})\phi(t-sT)\,d\boldsymbol{x}dt. \end{aligned} \tag{6.12}$$

With the ultra-narrowband assumption, we approximate $\tilde{p}^*(\mu(t-sT))\tilde{p}(t-R(t,\mathbf{x})) \approx 1$ and combine $e^{-i\omega_0 R(sT,\mathbf{x})/c_0]}e^{i\omega_0\mu sT}$ with the amplitude term to write

$$d(s,\mu) = \int e^{i\omega_0 t[(1-\mu)-\beta(s,\mathbf{x},\mathbf{v})]}e^{i\omega_0 sT\beta(s,\mathbf{x},\mathbf{v})}\tilde{A}(\omega_0,s,\boldsymbol{x},\mu)\rho(\boldsymbol{x})\phi(t-sT)\,d\boldsymbol{x}dt. \tag{6.13}$$

We then expand $\beta(s,\mathbf{x},\mathbf{v})$ around $s = s_c$ in the remaining exponential term and write

$$\begin{aligned} \beta(s,\mathbf{x},\mathbf{v}) &\approx \beta(s_c,\mathbf{x},\mathbf{v}) + \dot{\beta}(s_c,\mathbf{x},\mathbf{v})(s-s_c) + \ddot{\beta}(s_c,\mathbf{x},\mathbf{v})\frac{(s-s_c)^2}{2} \\ &= \beta(s_c,\mathbf{x},\mathbf{v}) + \ddot{\beta}(s_c,\mathbf{x},\mathbf{v})\frac{(s-s_c)^2}{2}, \end{aligned} \tag{6.14}$$

where s_c satisfies $\dot{\beta}(s_c,\mathbf{x},\mathbf{v}) = 0$. We combine the quadratic term with the amplitude and obtain

$$d(s,\mu) = \int e^{i\omega_0 t[(1-\mu)-\beta(s,\mathbf{x},\mathbf{v})]} e^{i\omega_0 s_c T\beta(s_c,\mathbf{x},\mathbf{v})} \tilde{A}(\omega_0, s, \boldsymbol{x}, \mu)\rho(\boldsymbol{x})\phi(t-sT)\, d\boldsymbol{x}dt. \tag{6.15}$$

Finally, if we backproject this data to the iso-Doppler contours we will reconstruct the reflectivity function

$$e^{i\omega_0 s_c T\beta(s_c,\mathbf{x},\mathbf{v})}\rho(\boldsymbol{x}) \tag{6.16}$$

We assume we are receiving signals at two antenna phase centers moving in tandem so that after a time delay of Δs, the second antenna passes through the location of the first antenna with the same velocity. Therefore, $\boldsymbol{\gamma}_R^1(s) = \boldsymbol{\gamma}_R^2(s+\Delta s)$ and $\dot{\boldsymbol{\gamma}}_R^1(s) = \dot{\boldsymbol{\gamma}}_R^2(s+\Delta s)$. Backprojecting to the iso-Doppler contours, the first antenna will reconstruct the image

$$\rho_1(\boldsymbol{x}) = e^{i\omega_0 s_c T\beta_1(s_c,\mathbf{x},\mathbf{v})}\rho(\boldsymbol{x}), \tag{6.17}$$

and after a time delay of Δs, the second antenna will reconstruct the image

$$\rho_2(\boldsymbol{x}) = e^{i\omega_0 s_c T\beta_2(s_c+\Delta s,\mathbf{x},\mathbf{v})}\rho(\boldsymbol{x}). \tag{6.18}$$

Using the above assumptions about the relationship between the two antenna channels, we simplify $\beta_2(s+\Delta s,\mathbf{x},\mathbf{v})$ to

$$\begin{aligned}\beta_2(s+\Delta s,\mathbf{x},\mathbf{v}) &= \frac{1}{c_0}[(\mathbf{x}+\mathbf{v}(s+\widehat{\Delta s)-}\boldsymbol{\gamma}_R^2(s+\Delta s))\cdot(\mathbf{v}-\dot{\boldsymbol{\gamma}}_R^2(s+\Delta s)) \\ &\quad + (\mathbf{x}+\mathbf{v}(\widehat{s+\Delta s})-\boldsymbol{\gamma}_T)\cdot\mathbf{v}] \\ &\approx \beta_1(s,\mathbf{x},\mathbf{v}) + \beta_d(s,\mathbf{x},\mathbf{v})\Delta s\end{aligned} \tag{6.19}$$

where

$$\beta_d(s,\mathbf{x},\mathbf{v}) = \frac{1}{c_0}\left[\frac{\mathbf{v}_R^{\perp}\cdot(\mathbf{v}-\dot{\boldsymbol{\gamma}}_R^1(s))}{|\mathbf{x}+\mathbf{v}s-\boldsymbol{\gamma}_R^1(s)|} + \frac{\mathbf{v}_T^{\perp}\cdot\mathbf{v}}{|\mathbf{x}+\mathbf{v}s-\boldsymbol{\gamma}_T|}\right], \tag{6.20}$$

and

$$\mathbf{v}_R^{\perp} = \mathbf{v} - (\mathbf{x} + \widehat{\mathbf{v}s - \boldsymbol{\gamma}_R^1}(s))[(\mathbf{x} + \widehat{\mathbf{v}s - \boldsymbol{\gamma}_R^1}(s)) \cdot \mathbf{v}] \tag{6.21}$$

$$\mathbf{v}_T^{\perp} = \mathbf{v} - (\mathbf{x} \widehat{+ \mathbf{v}s -} \boldsymbol{\gamma}_T)[(\mathbf{x} \widehat{+ \mathbf{v}s -} \boldsymbol{\gamma}_T) \cdot \mathbf{v}]. \tag{6.22}$$

The vectors $\mathbf{v}_R^{\perp}$ and $\mathbf{v}_T^{\perp}$ represent the target velocity vector projected in the direction perpendicular to the receiver look direction and transmitter look direction, respectively. Finally, plugging back into the reconstructed image for the second antenna, we obtain

$$\begin{aligned} \rho_2(\boldsymbol{x}) &= e^{i\omega_0 s_c T \beta_2(s_c + \Delta s, \mathbf{x}, \mathbf{v})} \rho(\boldsymbol{x}) \\ &\approx e^{i\omega_0 s_c T [\beta_1(s_c, \mathbf{x}, \mathbf{v}) + \beta_d(s_c, \mathbf{x}, \mathbf{v}) \Delta s]} \rho(\boldsymbol{x}) \\ &= e^{i\omega_0 s_c T \beta_d(s_c, \mathbf{x}, \mathbf{v}) \Delta s} \rho_1(\boldsymbol{x}) \end{aligned} \tag{6.23}$$

The $\beta_d(s, \mathbf{x}, \mathbf{v})$ term can be interpreted as a Doppler-rate, and after multiplication by the time delay Δs, adds an additional Doppler shift to the received signal, which becomes combined into the scene reflectivity. This scenario is depicted in Figure 6.1. The two antennas are shown at two points in time, s in red, and $s + \Delta s$ in blue. At time s, the moving target caused a Doppler shift of β_1, measured at the first antenna. After a time shift of Δs, as shown in the blue trajectory, the second antenna measures the Doppler shift of $\beta_2 \approx \beta_1 + \beta_d \Delta s$ at the same location as the first antenna.

This result is intuitive and is analogous to the one from conventional SAR. As described in the previous section, in conventional (wideband) SAR, range is measured via time delay using relatively wideband signals. The phase shift between the two receiving channels is a difference in range, which is the range-rate multiplied by the time delay. As shown here, in Doppler-SAR, since we measure Doppler shift, the phase shift between the two channels is a Doppler shift. This Doppler shift is the result of the Doppler-rate multiplied by the time delay between the two data sets.

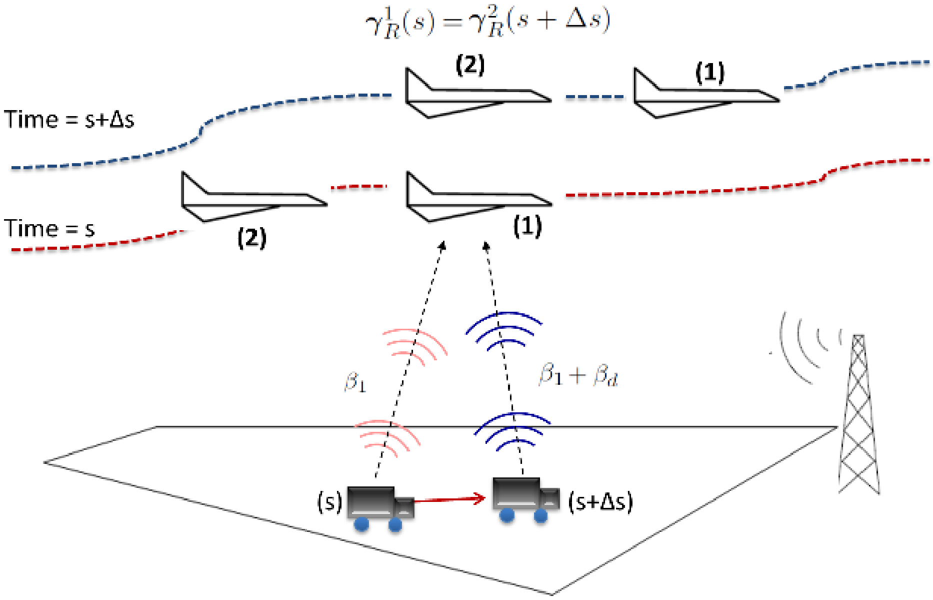

Figure 6.1: Illustration of the temporal Doppler shift measured at two different times for the location $\gamma_R^1(s) = \gamma_R^2(s+\Delta s)$. At time s, receiver 1 measures the Dopppler shift β_1. At time $s + \Delta s$, receiver 2 measures the Doppler shift $\beta_1 + \beta_d$ at the same trajectory location.

6.4 Clutter Suppression Using Two-Channel Doppler SAR

Under the assumptions of two phase centers traveling in tandem, we have a data model where the two sets of data differ only by a single phase shift. This phase shift is zero for stationary targets, and nonzero for moving targets. The DPCA and ATI techniques have been well studied in the case of conventional SAR. In this section, we show how the two techniques can be applied to Doppler-SAR.

6.4.1 Displaced Phase Center Antenna

The displaced phase center antenna (DPCA) technique cancels the stationary clutter by subtracting the two channels. Since the image reconstruction method is linear, the subtraction can be performed either in the data domain or the image domain. When subtracting the two channels at a time shift of Δs we obtain

$$\begin{aligned}\mathcal{K}[d^1(s,\mu) - d^2(s+\Delta s,\mu)] &= \mathcal{K}[d^1(s,\mu)] - \mathcal{K}[d^2(s+\Delta s,\mu)] \\ &= \rho_1(\boldsymbol{x}) - e^{i\omega_0 s_c T\beta_d(s_c,\mathbf{x},\mathbf{v})\Delta s}\rho_1(\boldsymbol{x}) \\ &= \rho_1(\boldsymbol{x})[1 - e^{i\omega_0 s_c T\beta_d(s_c,\mathbf{x},\mathbf{v})\Delta s}],\end{aligned} \tag{6.24}$$

where $\mathcal{K}$ is the backprojection operator. We see that for stationary targets, the Doppler shift is zero, and the subtraction returns no target at that pixel.

6.4.2 Along-Track Interferometry

In interferometric SAR, two receiver channels are used to capture slightly different information. Images are then formed for each channel and their complex conjugates are multiplied. An image of the phase (or interferogram) of the resulting product is used to find the difference in phase of the two channels. In along-track interferometry (ATI), the two channels are displaced along the velocity vector of the antennas just as described in the previous section, so that they acquire information about the same scene from the same location, but at different points in time.

Multiplying the image formed from the first channel by the complex conjugate of the image formed from the second channel, we obtain

$$\rho_1(\boldsymbol{x})\rho_2^*(\boldsymbol{x}) = |\rho_1(\boldsymbol{x})|^2 e^{-i\omega_0 s_c T\beta_d(s_c,\mathbf{x},\mathbf{v})\Delta s}. \tag{6.25}$$

When looking at the phase function

$$\Phi = \omega_0 s_c T\beta_d(s_c,\mathbf{x},\mathbf{v})\Delta s, \tag{6.26}$$

we see that stationary objects, which have no Doppler shift, will be zero in the phase image.

6.5 Numerical Simulations

We performed numerical simulations with moving targets under various types of stationary clutter in order to visually see the effect of the different clutter suppression techniques. Two receivers were flying in tandem in a circular trajectory around the scene with a radius of 6 km at a speed of 200 m/s. The receivers were flying at an altitude of 1 km over 45° of the aperture. The two receiver channels were displaced such that the second phase center passed through the same location as the first phase center after a time delay of 0.5 ms.

A single stationary transmitter was placed at the coordinates $(4000, -4000)$ m at an altitude of 1 km, where the origin is the center of the scene of interest. The waveform was a single frequency signal at 80 MHz lasting 1 μs in length.

The first simulation demonstrates the simplest possible case of a single moving target with no clutter or noise. Figure 6.2 shows the original scene with the moving target traveling at a speed of 8 m/s at an angle of 280° from the positive x-axis. The reconstructed image from the first channel is shown in Figure 6.3. The target is smeared because we backproject to zero-velocity iso-Doppler contours. As shown in the previous chapter, if we were to backproject to contours for the correct target velocity, we would obtain a focused image. Finally, the results of the DPCA and ATI clutter suppression techniques are shown in Figure 6.4 and Figure 6.5, respectively. The DPCA image looks very similar to the single channel image since there is no clutter. The ATI image shows positive phase components where the moving target response was backprojected. Since we are backprojecting using such a small part of the aperture and with no filtering, the target response is relatively smeared. Also, note that the phase of the image is wrapped to the range of $-\pi$ to π, this may cause periodic ambiguities in the resulting phase image, since it is not actually the unwrapped interferometric phase function we desire.

The second simulation expands on the results of the first by adding in a large stationary object. This would be similar to a large building in a real-life scenario. Figure 6.6 shows the original scene, with the same moving target as with the first scenario, and now with a stationary rectangular object near the center of the scene. The reconstructed image for the first channel is shown in Figure 6.6. The building response is smeared and significantly overpowers the moving target response. When the DPCA technique is used, we are able to completely cancel out the stationary target response, as shown in Figure 6.8. This image is identical to Figure 6.4, the

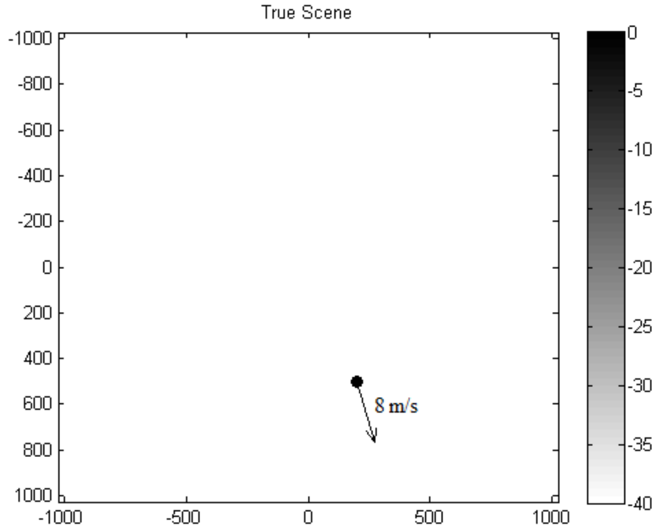

Figure 6.2: Original scenario for the first simulation. There is a single moving target located at $(200, -500)$ moving at 8 m/s at an angle of $280°$ from the positive x-axis.

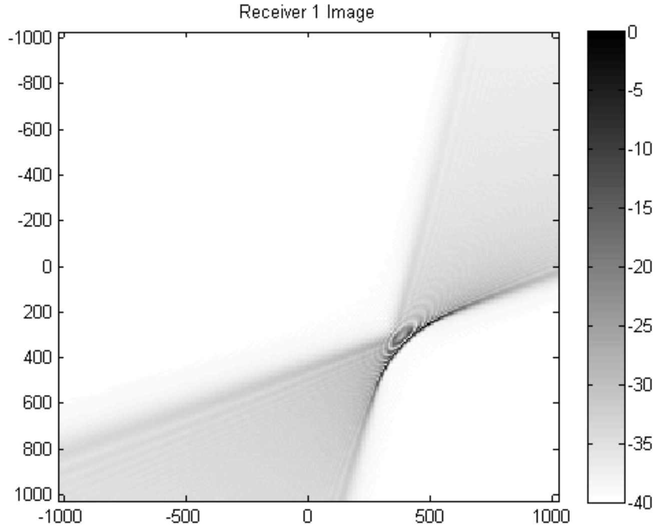

Figure 6.3: Reconstructed image for the first antenna channel. The receiver 1 data is backprojected to zero-velocity iso-Doppler contours, yielding the moving target reconstruction shown here. There is no stationary clutter in the image, so we see the moving target response adequately in this figure.

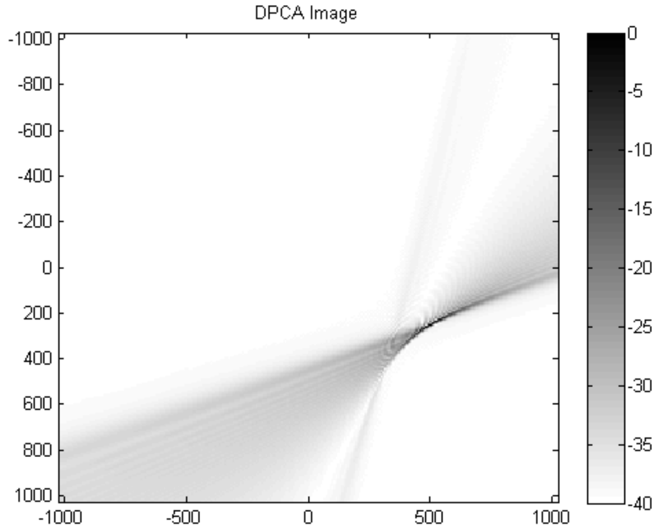

Figure 6.4: DPCA image for the first scenario. The reconstructed images from each channel are subtracted from each other. Since the target response is slightly different for each receiver, and there is no stationary clutter, the image looks similar to the one created by a single channel.

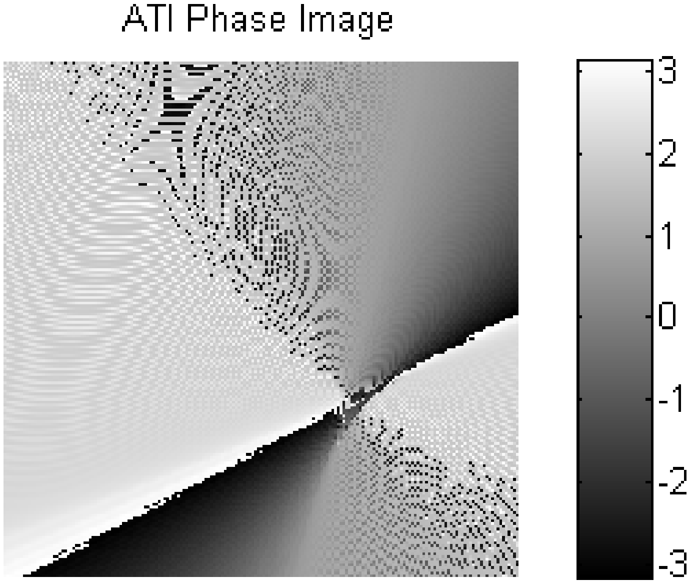

Figure 6.5: ATI image for the first scenario. The image shows a positive interferometric phase for all pixels on the image that have a contribution from the moving target.

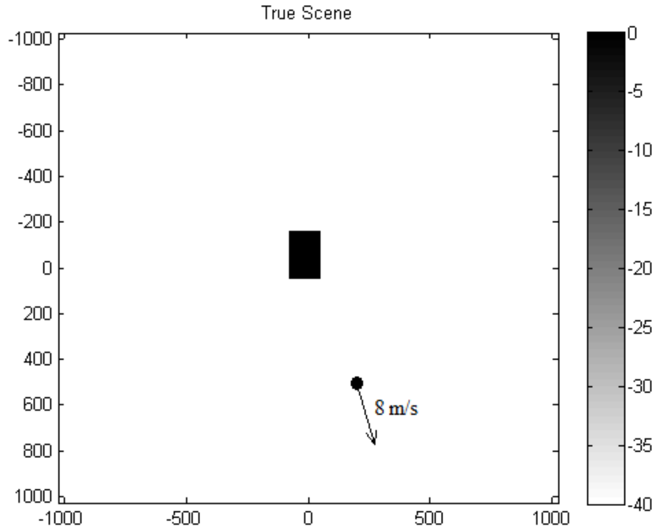

Figure 6.6: Original scenario for the second simulation. In addition to the single moving target, we have an extended stationary target, which will contaminate the moving target response in single channel data.

DPCA image for the first scenario, since the nonstationary component of the scene is the same. Finally, we see the interferogram from the ATI technique in Figure 6.9. In this figure, the stationary clutter response is eliminated, and we see positive phase contributions from the moving target response in the bottom right area of the image.

In the third scenario, we add random stationary clutter to every pixel in the image, in addition to the large extended stationary target and multiple moving targets. The original scene is shown in Figure 6.10. In addition to the moving target in the previous simulations, there is a moving target in the top left moving at 8 m/s at an angle of $-50°$ and a moving target in the top right moving at 4 m/s at $20°$. Along with these moving targets there are two stationary point targets in the bottom left and bottom right. Random clutter was added to each pixel using a Rayleigh distribution and a signal-to-clutter ratio (SCR) of -10 dB. Figure 6.11 shows the image reconstruction for the first channel. As with the previous simulation, the smeared responses of the extended stationary target and the random clutter mask all visibility of the three moving targets. When we subtract the images reconstructed

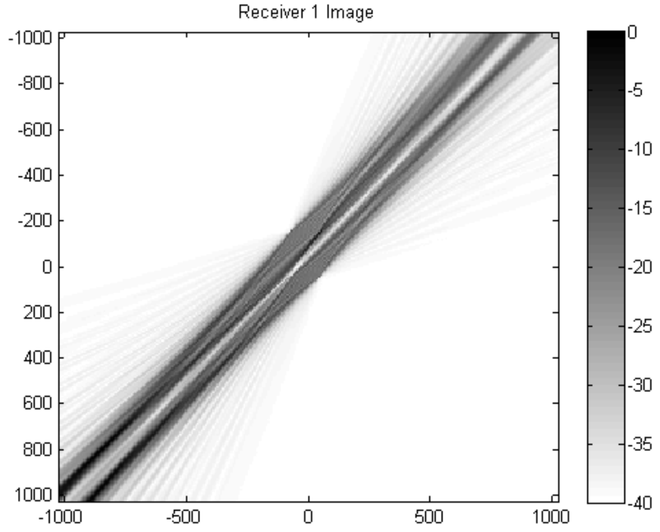

Figure 6.7: Reconstructed image for the first channel in scenario 2. The extended stationary target is smeared and masks the moving target signature completely.

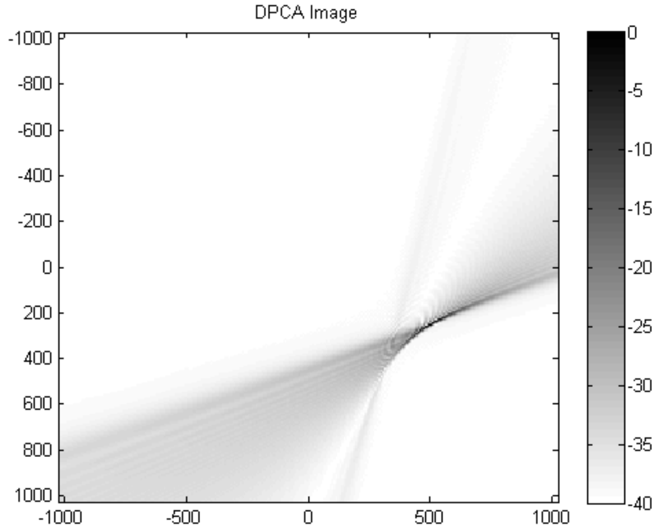

Figure 6.8: DPCA image for the second simulation. The response from the extended stationary target is completely canceled, and we are left with the moving target response. This image is identical to the DPCA image from the first simulation, because the moving target has the same parameters.

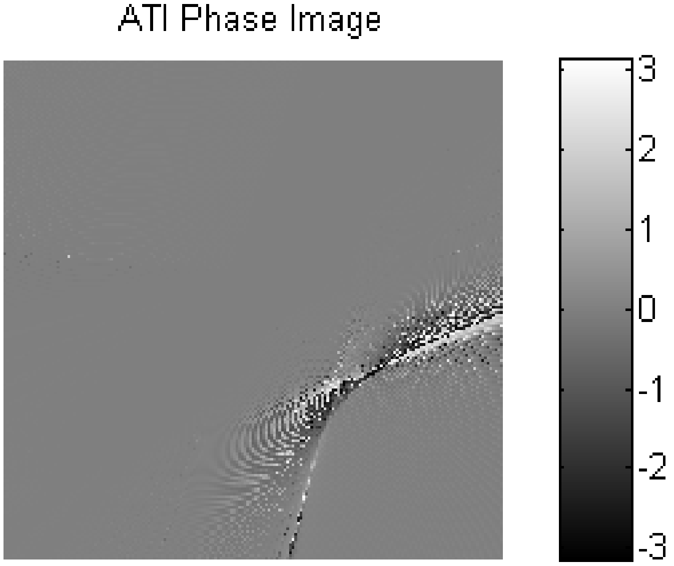

Figure 6.9: ATI image for the second simulation. The extended stationary target response is eliminated in this image as well, and we see the moving target contributions to the phase in the bottom right area of the image.

by each channel, we obtain the DPCA image shown in Figure 6.12. Here, we see that the three moving targets are reconstructed, and all of the stationary components of the scene (the point targets, extended target, and random clutter), are canceled completely. In Figure 6.13, we see the result of the ATI technique. For visual purposes, the image shown is the absolute value of the phase image, so that the zero phase is of zero intensity, and increasing positive or negative phase increases the intensity. Here, the clutter is so high that barely one of the moving targets is distinguishable. When the SCR is increased to 20 dB, however, we do see that the ATI method brings out the moving target responses, as shown in Figure 6.14.

6.6 Conclusion

In this chapter, we analyzed how the DPCA and ATI clutter suppression methods can be applied to Doppler-SAR. Unlike conventional SAR, where the image is formed by using time delay to backproject onto iso-range contours, Doppler-SAR uses the Doppler shift in ultra-narrowband waveforms to backproject onto iso-

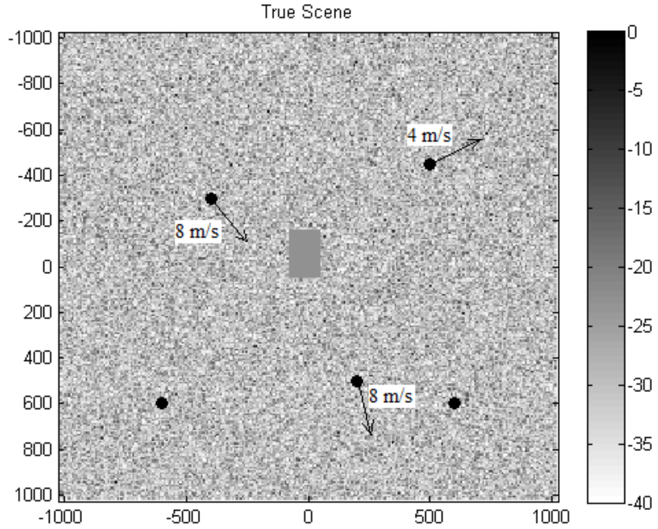

Figure 6.10: Original scenario for the third simulation. In addition to the single moving target and extended stationary target from simulation two, there are two additional moving targets, two stationary targets, and randomly distributed clutter added to each pixel.

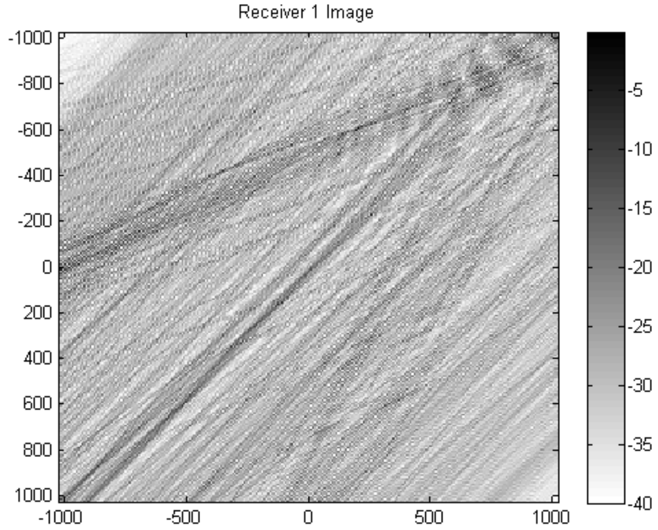

Figure 6.11: Single image reconstruction for the third scenario. The clutter masks all signatures of the moving targets, and we are unable see any targets in the reconstructed image.

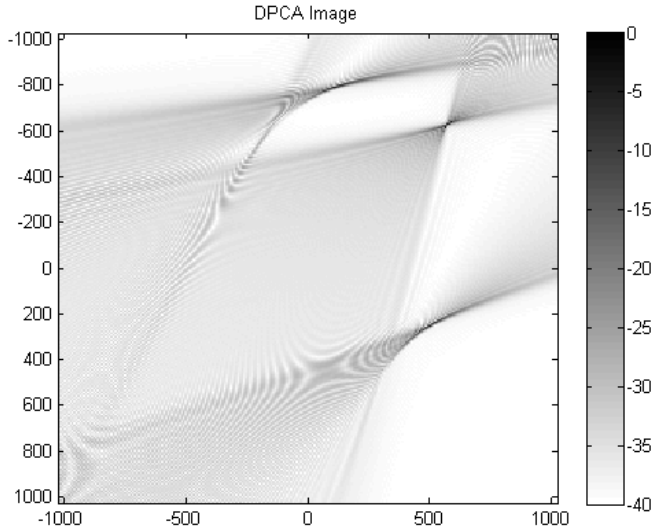

Figure 6.12: DPCA image for the third simulation. The image subtraction process successfully cancels out the extended target, all random clutter, and stationary point scatterers.

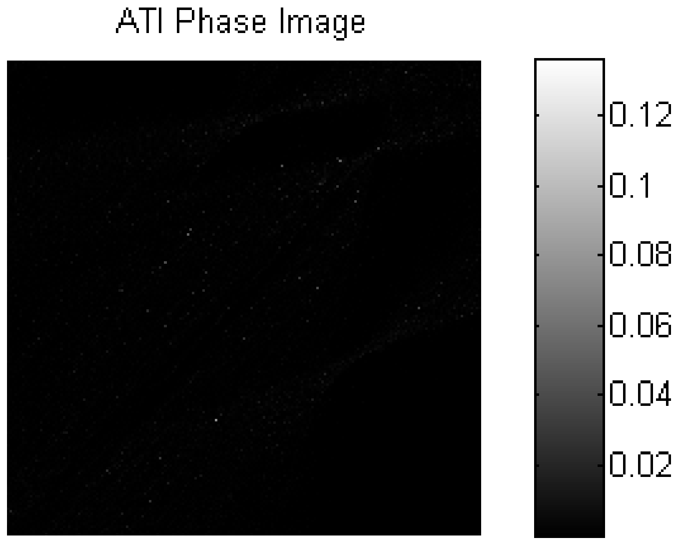

Figure 6.13: ATI image for the third simulation. Here, the clutter is so high that the phase subtraction is unable to bring out the moving targets from the rest of the scene.

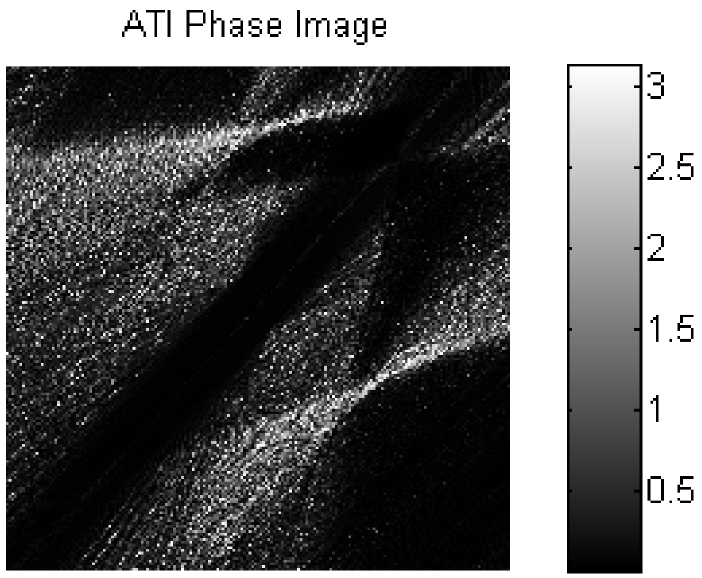

Figure 6.14: ATI image for the third simulation, but with the clutter reduced to a SCR level of 20 dB. Now, the moving target responses can be seen clearly.

Doppler contours. Clutter suppression is an extremely important problem in ground moving target imaging, because moving targets are often embedded in strong, stationary ground clutter. In order to detect moving targets, ground clutter must be suppressed enough to bring out the moving target signatures and estimate their velocities.

Both the DPCA and ATI techniques rely on a pair of antenna phase centers moving in tandem, so that after a time delay, the second antenna passes through the same location as the first antenna with the same velocity. This configuration enables data to be collected from a dynamic scene at different points in time from the same location. In this setup, stationary ground clutter will yield the same scattered signal for each antenna, but the moving targets will produce different responses. The DPCA technique takes advantage of this by subtracting the data collected by the second antenna from the data collected by the first antenna. ATI follows a similar approach, but does the subtraction in the phase by multiplying the image produced by the first channel by the complex conjugate of the image formed by the second channel.

We show that in conventional SAR, the phase difference between the two channels is a range quantity, coming from the range-rate of the moving target multiplied by the time delay between the antenna phase centers. In Doppler-SAR, we show that the phase difference is a Doppler shift quantity, coming from a Doppler-rate term multiplied by the time delay between the antennas. This is an intuitive result, since Doppler-SAR uses ultra-narrowband illuminators to measure temporal Doppler shift instead of range. Finally, we ran numerical simulations to demonstrate the performance of the clutter suppression techniques.

CHAPTER 7
Conclusion

In this work we have studied image reconstruction methods for performing SAR imaging of ground moving targets using passive receivers. Passive radar has important advantages over active radar, particularly in defense and surveillance applications, making it an important problem to study in modern radar. Additionally, typical active SAR image reconstruction methods do not take into account the presence of moving targets. In the reconstructed images, the moving targets appear smeared and mislocated from their true position. Since many targets of interest in applications such as defense and surveillance are moving, it is important to understand and hopefully correct for these motion artifacts.

The first major section of work deals with an image reconstruction method for synthetic aperture hitchhiker imaging of ground moving targets. The method performs image reconstruction and velocity estimation of multiple ground moving targets using only passive receivers, without knowledge of transmitter location or waveform. A network of mobile receivers is flown over a scene of interest, received waveforms are correlated between each pairs of receivers, and images are formed based on this correlated data. Since the image formation method depends on the typical time-delay-based information to obtain high resolution, it is assumed that there are illuminators of opportunity in the environment transmitting waveforms with high enough bandwidth to obtain good range resolution. A stack of images is formed over a range of hypothesized velocities, and image entropy is used to evaluate the degree of focus of each image. The images with the lowest entropy are the focused images for the corresponding moving target.

Next, we performed a detailed study of two aspects of performance for this imaging method. Resolution in both image and velocity is analyzed by studying the phase of the image fidelity operator. Factors such as hitchhiker angle, aperture length, and bandwidth, were identified as being important for the purpose of maximizing resolution. We then studied the nature of positioning errors of moving targets due to an incorrect hypothesized velocity. An analytic representation of these position errors as a function of the error in hypothesized velocity was determined in the component parallel to the antenna look direction and it's orthogonal direction. This work applies to existing backprojection-based SAR algorithms as well, since many inherently assume a zero hypothesized velocity.

Finally, we look at passive SAR imaging using ultra-narrowband sources of opportunity. Since many existing sources of opportunity are in fact ultra-narrowband, they may not provide sufficient range resolution required in the first method. In addition to availability, ultra-narrowband waveforms have inherent advantages over conventional wideband waveforms, such as cheaper transmitters and potential space-based applications. Doppler hitchhiker imaging of ground moving targets takes advantage of the long signal duration and high Doppler resolution nature of ultra-narrowband sources of opportunity by backprojecting to high resolution iso-Doppler contours instead of the iso-range contours. We develop an image reconstruction method analogous to the wideband hitchhiker method in Chapter 3, where the received signals are correlated between pairs of receivers, and focused images are formed by using a hypothesized velocity for backprojection.

In ground moving target imaging, clutter is always an important problem to consider, and in addition, the entropy-based velocity estimation methods presented here need some degree of clutter suppression. We showed how the displaced phase center antenna (DPCA) and along-track interferometry (ATI) clutter suppression methods can be applied to the ultra-narrowband case (Doppler-SAR), and compared the nature of the phase relationship between the two channels in the ultra-narrowband case to the conventional SAR case. We show how in conventional SAR, the phase shift between the two channels is a range-rate multiplied by the time delay, while in the Doppler-SAR case, the phase shift is a Doppler-rate multiplied by a time delay.

Passive radar is an incredibly popular topic with many important applications, and the work presented in this thesis opens up the door to many more potential problems of interest. One interesting problem would be the application of the position error analysis to velocity estimation. The smearing of a moving target is caused by a growing position error over the course of the synthetic aperture. Knowing the nature of these position errors, as we have described in this work, may allow one to estimate target velocities directly from one or more images of different hypothesized velocities. Another area of future work would be analyzing the performance of the image reconstruction methods in other ways. An analysis of the relationship between image entropy and incorrect hypothesized velocity may yield more accurate and more efficient approaches for both image reconstruction and velocity estimation. Additionally, the sensitivity of other parameters, in addition to hypothesized velocity, could be analyzed. Antenna position, ground topography, and waveform synchronization are some examples of these parameters that may cause deterioration in the final image if they are not accounted for. Finally, more complex approaches may be taken to handle some of the more complex problems that arise in realistic scenarios. For example, polarimetry may provide important information about the nature of the moving target as well as handle issues with angular dependence arising from the large network of receivers used in some of these methods.

REFERENCES

[1] C. E. Muehe and M. Labitt, “Displaced-phase-center antenna technique,” *Lincoln Laboratory J.*, vol. 12, no. 2, pp. 281–296, 2000.

[2] R. Klemm, *Principles of Space-Time Adaptive Processing*, London, UK: Inst. Elect. Eng., 2002.

[3] R. W. Deming, “Along-track interferometry for simultaneous SAR and GMTI: application to gotcha challenge data,” in *SPIE Defense, Security, and Sensing*, Orlando, FL, 2011, pp. 80510P–80510P.

[4] V. C. Chen, “Time-frequency analysis of SAR images with ground moving targets,” in *Proc. SPIE*, Orlando, FL, 1998, vol. 3391, p. 295.

[5] M. J. Minardi *et al.*, “Ground moving target detection and tracking based on generalized SAR processing and change detection,” in *Proc. SPIE*, Orlando, FL, 2005, vol. 5808, p. 156.

[6] M. Martorella *et al.*, “Contrast maximisation based technique for 2-D ISAR autofocusing,” *IEE Proc. Radar, Sonar and Navigation*, vol. 152, pp. 253–262, Aug. 2005.

[7] C. V. Jakowatz Jr *et al.*, “Refocus of constant-velocity moving targets in synthetic aperture radar imagery,” in *Proc. SPIE*, Orlando, FL, 1998, vol. 3370, p. 85.

[8] S. Barbarossa, “Detection and imaging of moving objects with synthetic aperture radar. 1. optimal detection and parameter estimation theory,” *IEE Proc. Radar and Signal Process.*, vol. 139, pp. 79–88, Feb. 1992.

[9] M. Kirscht, “Detection and imaging of arbitrarily moving targets with single-channel SAR,” *IEE Proc. Radar, Sonar and Navigation*, vol. 150, pp. 7–11, Oct. 2003.

[10] M. Stuff *et al.*, “Imaging moving objects in 3D from single aperture synthetic aperture radar,” in *IEEE Proc. Radar Conf.*, Philadelphia, PA, 2004, pp. 94–98.

[11] F. Zhou *et al.*, “Approach for single channel SAR ground moving target imaging and motion parameter estimation,” *IET Radar, Sonar & Navigation*, vol. 1, no. 1, pp. 59–66, Feb. 2007.

[12] R. P. Perry *et al.*, “SAR imaging of moving targets,” *IEEE Trans. Aerosp. Electron. Syst.*, vol. 35, no. 1, pp. 188–200, Jan. 1999.

[13] S. Zhu *et al.*, “Ground moving targets imaging algorithm for synthetic aperture radar,” *IEEE Trans. Geosci. Remote Sens.*, vol. 49, no. 1, pp. 462–477, Jan. 2011.

[14] J. K. Jao, “Theory of synthetic aperture radar imaging of a moving target,” *IEEE Trans. Geosci. Remote Sens.*, vol. 39, no. 9, pp. 1984–1992, Sept. 2001.

[15] H. D. Griffiths and C. J. Baker, “Passive coherent location radar systems. part 1: performance prediction,” *IEE Proc. Radar, Sonar and Navigation*, vol. 152, no. 3, pp. 153 – 159, June 2005.

[16] C. J. Baker *et al.*, “Passive coherent location radar systems. part 2: waveform properties,” *IEE Proc. Radar, Sonar and Navigation*, vol. 152, no. 3, pp. 160–168, June 2005.

[17] H. D. Griffiths and C. J. Baker, “Measurement and analysis of ambiguity functions of passive radar transmissions,” in *IEEE Radar Conf.*, Arlington, VA, 2005, pp. 321 – 325.

[18] H. Griffiths and C. Baker, “The signal and interference environment in passive bistatic radar,” in *Inform., Decision and Control*, Adelaide, Qld., 2007, pp. 1–10.

[19] H. D. Griffiths and N. R. W. Long, “Television-based bistatic radar,” *IEE Proc. Communications, Radar and Signal Process.*, vol. 133, no. 7, pp. 649–657, Dec. 1986.

[20] P. E. Howland, "Target tracking using television-based bistatic radar," *IEE Proc. Radar, Sonar and Navigation*, vol. 146, pp. 166–174, June 1999.

[21] S. Herman and P. Moulin, "A particle filtering approach to fm-band passive radar tracking and automatic target recognition," in *IEEE Proc. Aerosp. Conf.*, Big Sky, MT, 2002, vol. 4, pp. 1789–1808.

[22] P. E. Howland *et al.*, "FM radio based bistatic radar," *IEE Proc. Radar, Sonar and Navigation*, vol. 152, no. 3, pp. 107 – 115, June 2005.

[23] L. M. Ehrman and A. D. Lanterman, "Automated target recognition using passive radar and coordinated flight models," in *Proc. SPIE*, Orlando, FL, 2003, vol. 5094, pp. 196–207.

[24] C. J. Coleman *et al.*, "A practical bistatic passive radar system for use with DAB and DRM illuminators," in *IEEE Proc. Radar Conf.*, Rome, Italy, 2008, pp. 1–6.

[25] F. Colone *et al.*, "A multistage processing algorithm for disturbance removal and target detection in passive bistatic radar," *IEEE Trans. Aerosp. Electron. Syst.*, vol. 45, no. 2, pp. 698 –722, Apr. 2009.

[26] B. Dawidowicz *et al.*, "Detection of moving targets with multichannel airborne passive radar," *IEEE Aerosp. Electron. Syst. Mag.*, vol. 27, no. 11, pp. 42–49, Nov. 2012.

[27] P. Krysik and K. Kulpa, "The use of a GSM-based passive radar for sea target detection," in *9th European Radar Conf.*, Amsterdam, Netherlands, 2012, pp. 142–145.

[28] M. M. Chitgarha *et al.*, "Choosing the position of the receiver in a MISO passive radar system," in *9th European Radar Conf.*, Amsterdam, Netherlands, 2012, pp. 318–321.

[29] A. D. Lanterman, "Passive radar imaging and target recognition using illuminators of opportunity," in *RTO SET Symp. Target Identification and Recognition Using RF Syst.*, Oslo, Norway, 2004, pp. 24–1–24–10.

[30] Y. Wu and D. C. Munson Jr., “Multistatic synthetic aperture imaging of aircraft using reflected television signals,” *SPIE Proc. Algorithms for Synthetic Aperture Radar Imagery VIII*, vol. 4382, Aug. 2001.

[31] Y. Wu and D. C. Munson Jr., “Multistatic passive radar imaging using the smoothed pseudo wigner-ville distribution,” in *Proc. Int. Conf. Image Process.*, Thessaloniki, Greece, 2001, vol. 3, pp. 604–607.

[32] A. D. Lanterman and D. C. Munson Jr., “Deconvolution techniques for passive radar imaging,” in *SPIE Proc. Algorithms for Synthetic Aperture Radar Imagery IX*, Orlando, FL, 2002, vol. 4727, pp. 166–177.

[33] M. Çetin and A. D. Lanterman, “Region-enhanced imaging for sparse-aperture passive radar,” in *SPIE Proc. Algorithms for Synthetic Aperture Radar Imagery XI*, Orlando, FL, 2004, vol. 5427, p. 177.

[34] M. Cetin and A. D. Lanterman, “Region-enhanced passive radar imaging,” *IEE Proc. Radar, Sonar and Navigation*, vol. 152, no. 3, pp. 185–194, June 2005.

[35] W. Jun *et al.*, “Passive radar imaging algorithm based on subapertures synthesis of multiple television stations,” in *Int. Conf. Radar*, Shanghai, China, 2006, pp. 1–4.

[36] L. Wang *et al.*, “Passive imaging using distributed apertures in multiple-scattering environments,” *Inverse Problems*, vol. 26, no. 6, pp. 065002, May 2010.

[37] L. Wang and B. Yazici, “Passive imaging of moving targets using sparse distributed apertures,” *SIAM J. Imag. Sci.*, vol. 5, no. 3, pp. 769–808, July 2012.

[38] C. Prati *et al.*, “Passive geosynchronous sar system reusing backscattered digital audio broadcasting signals,” *IEEE Trans. Geosci. Remote Sens.*, vol. 36, no. 6, pp. 1973–1976, Nov. 1998.

[39] J. Brown *et al.*, “Passive bistatic radar experiments from an airborne platform,” *IEEE Aerosp. Electron. Syst. Mag.*, vol. 27, no. 11, pp. 50–55, Nov. 2012.

[40] M. Cherniakov *et al.*, “Space surface bistatic SAR with space-borne non-cooperative transmitters,” in *European Radar Conf.*, Paris, France, 2005, pp. 9–12.

[41] C. E. Yarman and B. Yazıcı, “Synthetic aperture hitchhiker imaging,” *IEEE Trans. Image Process.*, vol. 17(11), pp. 2156–2173, Nov. 2008.

[42] C. E. Yarman *et al.*, “Doppler synthetic aperture hitchhiker imaging,” *Inverse Problems*, vol. 26, no. 6, pp. 065006, June 2010.

[43] L. Wang *et al.*, “Doppler-hitchhiker: A novel passive synthetic aperture radar using ultranarrowband sources of opportunity,” *IEEE Trans. Geosci. Remote Sens.*, vol. 49, pp. 1–17, Oct. 2011.

[44] D. E. Hack and M. A. Saville, “Analysis of SAR moving grid processing for focusing and detection of ground moving targets,” in *SPIE Proc.*, Orlando, FL, 2011, vol. 8051, p. 80510S.

[45] J. E. Palmer and S. J. Searle, “Evaluation of adaptive filter algorithms for clutter cancellation in passive bistatic radar,” in *IEEE Proc. Radar Conf.*, Atlanta, GA, 2012, pp. 0493–0498.

[46] D. K. P. Tan *et al.*, “Passive radar using global system for mobile communication signal: theory, implementation and measurements,” *IEE Proc. Radar, Sonar and Navigation*, vol. 152, no. 3, pp. 116–123, June 2005.

[47] V. Koch and R. Westphal, “New approach to a multistatic passive radar sensor for air/space defense,” *IEEE Aerosp. Electron. Syst. Mag.*, vol. 10, no. 11, pp. 24–32, Nov. 1995.

[48] K. S. Kulpa, “Multi-static entirely passive detection of moving targets and its limitations,” *IEE Proc. Radar, Sonar and Navigation*, vol. 152, no. 3, pp. 169–173, June 2005.

[49] D. Poullin, “Passive detection using digital broadcasters (DAB, DVB) with COFDM modulation,” *IEE Proc. Radar, Sonar and Navigation*, vol. 152, no. 3, pp. 143–152, June 2005.

[50] C. Mikhail *et al.*, “Bistatic synthetic aperture radar with non-cooperative LEOS based transmitter,” in *IEEE Proc. Geosci. Remote Sens. Symp.*, Honolulu, HI, 2000, vol. 2, pp. 861–862.

[51] J. Homer *et al.*, “Passive bistatic radar sensing with LEOS based transmitters,” in *IEEE Proc. Geosci. Remote Sens. Symp.*, Toronto, Canada, 2002, vol. 1, pp. 438–440.

[52] X. He *et al.*, “Signal detectability in SS-BSAR with GNSS non-cooperative transmitter,” *IEE Proc. Radar, Sonar and Navigation*, vol. 152, no. 3, pp. 124–132, June 2005.

[53] J. Garnier *et al.*, “Passive sensor imaging using cross correlations of noisy signals in a scattering medium,” *SIAM J. Imag. Sci.*, vol. 2, pp. 396–437, Apr. 2009.

[54] A. J. Weiss, “Direct geolocation of wideband emitters based on delay and doppler,” *IEEE Trans. Signal Process.*, vol. 59, no. 6, pp. 2513–2521, June 2011.

[55] J. R. Guerci, *Space-time adaptive processing for radar*, Norwood, MA: Artech House, 2003.

[56] J. Ward, “Space-time adaptive processing for airborne radar,” in *IEE Colloq. Space-Time Adaptive Process.*, London, UK, 1998, pp. 2–2(1).

[57] L. Xi *et al.*, “Autofocusing of ISAR images based on entropy minimization,” *IEEE Trans. Aerosp. Electron. Syst.*, vol. 35, no. 4, pp. 1240–1252, Oct. 1999.

[58] D. Atkinson *et al.*, “Automatic correction of motion artifacts in magnetic resonance images using an entropy focus criterion,” *IEEE Trans. Med. Imag.*, vol. 16, no. 6, pp. 903–910, Dec. 1997.

[59] A. F Yegulalp, “Minimum entropy SAR autofocus,” presented at the Adaptive Sensor Array Processing (ASAP) Workshop, Lexington, MA, 1999.

[60] J. R. Fienup, “Synthetic-aperture radar autofocus by maximizing sharpness,” *Optics Lett.*, vol. 25, no. 4, pp. 221–223, Feb. 2000.

[61] J. R. Fienup and J. J. Miller, “Aberration correction by maximizing generalized sharpness metrics,” *JOSA A*, vol. 20, no. 4, pp. 609–620, Apr. 2003.

[62] T. J. Kragh, “Monotonic iterative algorithm for minimum-entropy autofocus,” in *Adaptive Sensor Array Processing (ASAP) Workshop*, MIT Lincoln Laboratory, Lexington, MA, 2006.

[63] L. Demanet *et al.*, “A butterfly algorithm for synthetic aperture radar imaging,” *SIAM J. Imag. Sci.*, vol. 5, no. 1, pp. 203–243, Feb. 2012.

[64] K. Duman and B. Yazici, “Bi-static synthetic aperture radar imaging of moving targets,” *SIAM J. Imag. Sci.*, to be published.

[65] H. H. Barrett *et al.*, *Foundations of Image Science*, vol. 44, Hoboken, NJ: Wiley-Interscience, 2004.

[66] J. F. Treves, *Introduction to Pseudodifferential and Fourier Integral Operators Volume 2: Fourier Integral Operators*, vol. 2, New York, NY: Springer, 1980.

[67] B. Yazici and V. Krishnan (2010, Mar. 15) *Microlocal Analysis in Imaging* [ONLINE]. Available: http://www.ecse.rpi.edu/˜yazici/ICASSPTutorial/microlocal_ICASSP10.html (Date Last Accessed, August 3, 2013).

[68] S. M. Kay, *Fundamentals of Statistical Signal Processing, Volume II: Detection Theory*, vol. 7, Upper Saddle River, NJ: Prentice Hall, 1998.

[69] J. W. McCorkle and M. Rofheart, “Order nˆ2 log(n) backprojector algorithm for focusing wide-angle wide-bandwidth arbitrary-motion synthetic

aperture radar," in *SPIE Aerospace/Defense Sensing and Controls*, Orlando, FL, 1996, pp. 25–36.

[70] L. M. H. Ulander *et al.*, "Synthetic-aperture radar processing using fast factorized back-projection," *IEEE Trans. Aerosp. Electron. Syst.*, vol. 39, no. 3, pp. 760–776, July 2003.

[71] S. Nilsson and L. E. Andersson, "Application of fast back-projection techniques for some inverse problems of synthetic aperture radar," in *SPIE Conf. Series*, Orlando, FL, 1998, vol. 3370, pp. 62–72.

[72] E. Candes *et al.*, "Fast computation of fourier integral operators," *SIAM J. Scientific Comput.*, vol. 29, no. 6, pp. 2464–2493, Oct. 2007.

[73] E. Candes *et al.*, "A fast butterfly algorithm for the computation of fourier integral operators," *Multiscale Modeling & Simulation*, vol. 7, no. 4, pp. 1727–1750, June 2009.

[74] D. A. Shnidman, "Generalized radar clutter model," *IEEE Trans. Aerosp. Electron. Syst.*, vol. 35, no. 3, pp. 857–865, July 1999.

[75] K. Voccola *et al.*, "On the relationship between the generalized likelihood ratio test and backprojection for synthetic aperture radar imaging," in *SPIE Defense, Security, and Sensing*, Orlando, FL, 2009, pp. 73350I–73350I.

[76] B. Yazici *et al.*, "Synthetic-aperture inversion in the presence of noise and clutter," *Inverse Problems*, vol. 22, no. 5, pp. 1705, Aug. 2006.

[77] V. Krishnan *et al.*, "Multistatic synthetic aperture radar image formation," *IEEE Trans. Image Process.*, vol. 19, no. 5, pp. 1290–1306, May 2010.

[78] A. F. Yegulalp, "Analysis of sar image formation equations for stationary and moving targets," MIT Lincoln Laboratory, Lexington, MA, FPR-14, June 2002.

[79] S. Wacks and B. Yazici, "Passive synthetic aperture hitchhiker imaging of ground moving targets - part 1: Image formation and velocity estimation," *IEEE Trans. Image Process.*, to be published.

[80] L. Wang and B. Yazici, "Bistatic synthetic aperture radar imaging using ultranarrowband continuous waveforms," *IEEE Trans. Image Process.*, vol. 21, no. 8, pp. 3673–3686, Aug. 2012.

[81] L. Wang and B. Yazici, "Ground moving target imaging using ultranarrowband continuous wave synthetic aperture radar," *IEEE Trans. Geosci. Remote Sens.*, vol. 51, Sept. 2013.

[82] L. Wang and B. Yazici, "Bistatic synthetic aperture radar imaging of moving targets using ultra-narrowband continuous waveforms," *SIAM J. Imag. Sci.*, to be published.

[83] L. Wang and B. Yazici, "Synthetic aperture radar imaging of moving targets using ultra-narrowband continuous waveforms," in *9th European Conf. Synthetic Aperture Radar*, Nuremberg, Germany, 2012, pp. 324–327.

[84] L. Wang and B. Yazici, "Detection and imaging of multiple ground moving targets using ultra-narrowband continuous-wave SAR," in *SPIE Defense, Security, and Sensing*, Baltimore, MD, 2012, pp. 83940H–83940H.

[85] L. Wang and B. Yazici, "Bistatic synthetic aperture radar imaging using ultranarrow-band continuous waveforms," in *IEEE Radar Conf.*, Kansas City, MO, 2011, pp. 062–067.

[86] L. Wang and B. Yazici, "Ultranarrow-band synthetic aperture radar imaging for arbitrary flight trajectories," in *17th Int. Conf. Digital Signal Process.*, Corfu, Greece, 2011, pp. 1–6.

[87] J. H. Thomson and J. E. B. Ponsonby, "Two-dimensional aperture synthesis in lunar radar astronomy," *Proc. Roy. Soc. London. Series A. Math. and Physical Sci.*, vol. 303, no. 1475, pp. 477–491, Mar. 1968.

[88] M. S. Roulston and D. O. Muhleman, "Synthesizing radar maps of polar regions with a doppler-only method," *Applied Optics*, vol. 36, no. 17, pp. 3912–3919, June 1997.

[89] B. Borden and M. Cheney, "Synthetic-aperture imaging from high-doppler-resolution measurements," *Inverse Problems*, vol. 21, no. 1, pp. 1, Nov. 2004.

[90] L. Wang and B. Yazici, "Passive imaging of moving targets using sparse distributed apertures," *SIAM J. Imag. Sci.*, vol. 5, no. 3, pp. 769–808, July 2012.

[91] L. Wang and B. Yazici, "Passive imaging of moving targets exploiting multiple scattering using sparse distributed apertures," *Inverse Problems*, vol. 28, no. 12, pp. 125009, Nov. 2012.

[92] T. J. Nohara, "Comparison of dpca and stap for space-based radar," in *IEEE Int. Radar Conf.*, Alexandria, VA, 1995, pp. 113–119.

[93] R. W. Deming, "Along-track interferometry for simultaneous SAR and GMTI: application to gotcha challenge data," in *SPIE Defense, Security, and Sensing*, Orlando, FL, 2011, pp. 80510P–80510P.

[94] C. W. Chen, "Performance assessment of along-track interferometry for detecting ground moving targets," in *IEEE Proc. Radar Conf.*, Philadelphia, PA, 2004, pp. 99–104.

[95] V. Pascazio *et al.*, "Moving target detection by along-track interferometry," in *Int. Geosci. Remote Sens. Symp.*, Sydney, NSW, 2001, vol. 7, pp. VII–3024.

[96] J. H. G. Ender, "Space-time processing for multichannel synthetic aperture radar," *Electronics & Communication Engineering J.*, vol. 11, no. 1, pp. 29–38, Feb. 1999.

[97] R. M. Goldstein and H. A. Zebker, "Interferometric radar measurement of ocean surface currents," *Nature*, vol. 328, no. 6132, pp. 707–709, Aug. 1987.

[98] F. Qin *et al.*, "A method of hybrid ati and dpca technique to detect moving target," in *Int. Conf. Radar*, Shanghai, China, 2006, pp. 1–4.

[99] H. Zhou *et al.*, "Moving target detection and velocity estimation using multiple subband DPCA and ATI method for triple-channel UWB SAR," in *9th Int. Conf. Signal Process.*, Beijing, China, 2008, pp. 2653–2656.

[100] D. J. Coe and R. G. White, "Moving target detection in sar imagery: experimental results," in *Int. Radar Conf.*, Alexandria, VA, 1995, pp. 644–649.

[101] T. J. Nohara *et al.*, "SAR-GMTI processing with canada's radarsat 2 satellite," in *Adaptive Systems for Signal Processing, Communications, and Control Symp.*, Lake Louise, Alta, 2000, pp. 379–384.

[102] C. H. Gierull and I. C. Sikaneta, "Raw data based two-aperture SAR ground moving target indication," in *IEEE Proc. Int. Geosci. Remote Sens. Symp.*, Toulouse, France, 2003, vol. 2, pp. 1032–1034.

[103] E. Chapin and C. W. Chen, "Airborne along-track interferometry for GMTI," *IEEE Aerosp. Electron. Syst. Mag.*, vol. 24, no. 5, pp. 13–18, May 2009.

[104] S. Wacks and B. Yazici, "Passive synthetic aperture hitchhiker imaging of ground moving targets - part 2: Performance analysis," *IEEE Trans. Image Process.*, to be published.

[105] S. Wacks and B. Yazici, "Bistatic Doppler-SAR DPCA imaging of ground moving targets," in *IEEE Proc. Radar Conf.*, Cincinnati, OH, 2014.

APPENDIX A
Derivation of the Iso-Doppler Contours

The iso-Doppler contours are represented by the set of points $(\boldsymbol{x}, \boldsymbol{v})$ that statisfy

$$\partial_s R_{ij}(\mathbf{x}, s) + \partial_s B_{ij}(\mathbf{x}, \mathbf{v}, s) = C_D, \tag{A.1}$$

where C_D is a constant.

Differentiating the $R_{ij}(\mathbf{x}, s)$ and $B_{ij}(\mathbf{x}, \mathbf{v}, s)$ terms with respect to s yields

$$\begin{aligned}
&- \dot{\boldsymbol{\gamma}}_i(s) \cdot (\widehat{\mathbf{x} - \boldsymbol{\gamma}_i(s)}) + \dot{\boldsymbol{\gamma}}_j(s) \cdot (\widehat{\mathbf{x} - \boldsymbol{\gamma}_j(s)}) \\
&+ \frac{1}{|\mathbf{x} - \boldsymbol{\gamma}_i(s)|}\big[(\mathbf{x} - \boldsymbol{\gamma}_i(s)) \cdot \mathbf{v} - \dot{\boldsymbol{\gamma}}_i(s) \cdot \mathbf{v}s \\
&- ((\widehat{\mathbf{x} - \boldsymbol{\gamma}_i(s)}) \cdot \mathbf{v}s)(-\dot{\boldsymbol{\gamma}}_i(s) \cdot (\widehat{\mathbf{x} - \boldsymbol{\gamma}_i(s)}))\big] \\
&- \frac{1}{|\mathbf{x} - \boldsymbol{\gamma}_j(s)|}\big[(\mathbf{x} - \boldsymbol{\gamma}_j(s)) \cdot \mathbf{v} - \dot{\boldsymbol{\gamma}}_j(s) \cdot \mathbf{v}s \\
&- ((\widehat{\mathbf{x} - \boldsymbol{\gamma}_j(s)}) \cdot \mathbf{v}s)(-\dot{\boldsymbol{\gamma}}_j(s) \cdot (\widehat{\mathbf{x} - \boldsymbol{\gamma}_j(s)}))\big] \\
= \; & (\widehat{\mathbf{x} - \boldsymbol{\gamma}_i(s)}) \cdot (\mathbf{v} - \dot{\boldsymbol{\gamma}}_i(s)) - (\widehat{\mathbf{x} - \boldsymbol{\gamma}_j(s)}) \cdot (\mathbf{v} - \dot{\boldsymbol{\gamma}}_j(s)) \\
&+ \frac{-\dot{\boldsymbol{\gamma}}_i(s) \cdot \mathbf{v}s - ((\widehat{\mathbf{x} - \boldsymbol{\gamma}_i(s)}) \cdot \mathbf{v}s)(-\dot{\boldsymbol{\gamma}}_i(s) \cdot (\widehat{\mathbf{x} - \boldsymbol{\gamma}_i(s)}))}{|\mathbf{x} - \boldsymbol{\gamma}_i(s)|} \\
&- \frac{-\dot{\boldsymbol{\gamma}}_j(s) \cdot \mathbf{v}s - ((\widehat{\mathbf{x} - \boldsymbol{\gamma}_j(s)}) \cdot \mathbf{v}s)(-\dot{\boldsymbol{\gamma}}_j(s) \cdot (\widehat{\mathbf{x} - \boldsymbol{\gamma}_j(s)}))}{|\mathbf{x} - \boldsymbol{\gamma}_j(s)|} \\
= \; & (\widehat{\mathbf{x} - \boldsymbol{\gamma}_i(s)}) \cdot (\mathbf{v} - \dot{\boldsymbol{\gamma}}_i(s)) - (\widehat{\mathbf{x} - \boldsymbol{\gamma}_j(s)}) \cdot (\mathbf{v} - \dot{\boldsymbol{\gamma}}_j(s)) \\
&- \frac{\dot{\boldsymbol{\gamma}}_i(s)s}{|\mathbf{x} - \boldsymbol{\gamma}_i(s)|} \cdot \big[\mathbf{v} - (\widehat{\mathbf{x} - \boldsymbol{\gamma}_i(s)})((\widehat{\mathbf{x} - \boldsymbol{\gamma}_i(s)}) \cdot \mathbf{v})\big] \\
&+ \frac{\dot{\boldsymbol{\gamma}}_j(s)s}{|\mathbf{x} - \boldsymbol{\gamma}_j(s)|} \cdot \big[\mathbf{v} - (\widehat{\mathbf{x} - \boldsymbol{\gamma}_j(s)})((\widehat{\mathbf{x} - \boldsymbol{\gamma}_j(s)}) \cdot \mathbf{v})\big].
\end{aligned} \tag{A.2}$$

We then define the $\mathbf{v}^\perp$ vectors as

$$\mathbf{v}_i^\perp = \mathbf{v} - (\widehat{\mathbf{x} - \boldsymbol{\gamma}_i(s)})[(\widehat{\mathbf{x} - \boldsymbol{\gamma}_i(s)}) \cdot \mathbf{v}] \tag{A.3}$$

$$\mathbf{v}_j^\perp = \mathbf{v} - (\widehat{\mathbf{x} - \boldsymbol{\gamma}_j(s)})[(\widehat{\mathbf{x} - \boldsymbol{\gamma}_j(s)}) \cdot \mathbf{v}] \tag{A.4}$$

and substitute into the derivative computed in (A.2) to obtain

$$\begin{aligned} C_D = (\widehat{\mathbf{x}-\boldsymbol{\gamma}_i(s)}) \cdot (\mathbf{v}-\dot{\boldsymbol{\gamma}}_i(s)) - (\widehat{\mathbf{x}-\boldsymbol{\gamma}_j(s)}) \cdot (\mathbf{v}-\dot{\boldsymbol{\gamma}}_j(s)) \\ - \frac{\dot{\boldsymbol{\gamma}}_i(s)s}{|\mathbf{x}-\boldsymbol{\gamma}_i(s)|} \cdot \mathbf{v}_i^{\perp} + \frac{\dot{\boldsymbol{\gamma}}_j(s)s}{|\mathbf{x}-\boldsymbol{\gamma}_j(s)|} \cdot \mathbf{v}_j^{\perp}. \end{aligned} \tag{A.5}$$

$\boldsymbol{\Xi}$ filter:

$$\begin{aligned} & - D\psi(\boldsymbol{z}) \cdot [(\widehat{\mathbf{z}-\boldsymbol{\gamma}_i(s)}) - (\widehat{\mathbf{z}-\boldsymbol{\gamma}_j(s)})] \\ & - \frac{D\psi(\boldsymbol{z}) \cdot \big[\mathbf{v} - (\widehat{\mathbf{z}-\boldsymbol{\gamma}_i(s)})[(\widehat{\mathbf{z}-\boldsymbol{\gamma}_i(s)}) \cdot \mathbf{v}]\big] s + \partial_{\boldsymbol{z}}^2 \psi(\boldsymbol{z}) \cdot \boldsymbol{v}(\psi(\boldsymbol{z}) - \boldsymbol{\gamma}_i^3(s))s}{|\mathbf{z}-\boldsymbol{\gamma}_i(s)|} \\ & + \frac{D\psi(\boldsymbol{z}) \cdot \big[\mathbf{v} - (\widehat{\mathbf{z}-\boldsymbol{\gamma}_j(s)})[(\widehat{\mathbf{z}-\boldsymbol{\gamma}_j(s)}) \cdot \mathbf{v}]\big] s + \partial_{\boldsymbol{z}}^2 \psi(\boldsymbol{z}) \cdot \boldsymbol{v}(\psi(\boldsymbol{z}) - \boldsymbol{\gamma}_j^3(s))s}{|\mathbf{z}-\boldsymbol{\gamma}_j(s)|} \end{aligned} \tag{A.6}$$

APPENDIX B

Derivation of the Ξ_{ij} vector

To derive the Ξ_{ij} vector, we let

$$\Xi_{ij}(s, \boldsymbol{x}', \boldsymbol{v}) = \nabla_{\boldsymbol{x}}[-R_{ij}(\mathbf{x}, s) - B_{ij}(\mathbf{x}, \mathbf{v}, s)]|_{\boldsymbol{x}=\boldsymbol{x}'}. \tag{B.1}$$

The gradient of the first term is equivalent to the result in [41] and is found to be

$$\begin{aligned} \nabla_{\boldsymbol{x}} R_{ij}(\mathbf{x}, s) &= \nabla_{\boldsymbol{x}}[|\mathbf{x} - \boldsymbol{\gamma}_i(s)| - |\mathbf{x} - \boldsymbol{\gamma}_j(s)|] \\ &= D\psi(\boldsymbol{x})[(\widehat{\mathbf{x} - \boldsymbol{\gamma}_i(s)}) - (\widehat{\mathbf{x} - \boldsymbol{\gamma}_j(s)})] \end{aligned} \tag{B.2}$$

where

$$D\psi(\boldsymbol{x}) = \begin{bmatrix} 1 & 0 & \partial\psi(\boldsymbol{x})/\partial x_1 \\ 0 & 1 & \partial\psi(\boldsymbol{x})/\partial x_2 \end{bmatrix} \tag{B.3}$$

The gradient of the second term containing the moving target motion is found by computing the gradient of each term:

$$\begin{aligned} \nabla_{\boldsymbol{x}}[(\widehat{\mathbf{x} - \boldsymbol{\gamma}_i(s)}) \cdot \mathbf{v}s] &= \nabla_{\boldsymbol{x}} \left[\frac{(\mathbf{x} - \boldsymbol{\gamma}_i(s)) \cdot \mathbf{v}s}{|\mathbf{x} - \boldsymbol{\gamma}_i(s)|} \right] \\ &= \frac{\nabla_{\boldsymbol{x}}[(\mathbf{x} - \boldsymbol{\gamma}_i(s)) \cdot \mathbf{v}s] - \nabla_{\boldsymbol{x}}|\mathbf{x} - \boldsymbol{\gamma}_i(s)|[(\mathbf{x} - \boldsymbol{\gamma}_i(s)) \cdot \mathbf{v}s]}{|\mathbf{x} - \boldsymbol{\gamma}_i(s)|^2} \\ &= \frac{\nabla_{\boldsymbol{x}}[(\mathbf{x} - \boldsymbol{\gamma}_i(s)) \cdot \mathbf{v}s] - D\psi(\boldsymbol{x})(\widehat{\mathbf{x} - \boldsymbol{\gamma}_i(s)})[(\mathbf{x} - \boldsymbol{\gamma}_i(s)) \cdot \mathbf{v}s]}{|\mathbf{x} - \boldsymbol{\gamma}_i(s)|^2} \end{aligned} \tag{B.4}$$

Note that the velocity vector is of the form

$$\mathbf{v} = [v_1, v_2, \nabla_{\boldsymbol{x}}\psi(\boldsymbol{x}) \cdot \boldsymbol{v}], \tag{B.5}$$

so we can find the gradient of the first term in (B.4) as

$$\begin{aligned}
\nabla_{\boldsymbol{x}}[(\mathbf{x} - \boldsymbol{\gamma}_i(s)) \cdot \mathbf{v}s] &= \nabla_{\boldsymbol{x}}[(x_1 - \boldsymbol{\gamma}_i^1(s))v_1 + (x_2 - \boldsymbol{\gamma}_i^2(s))v_2 \\
&\quad + (x_3 - \boldsymbol{\gamma}_i^3(s))\nabla_{\boldsymbol{x}}\psi(\boldsymbol{x}) \cdot \boldsymbol{v}]s \\
&= \begin{bmatrix} v_1 + \partial_{x_1}\psi(\boldsymbol{x})v_3 s \\ v_2 + \partial_{x_2}\psi(\boldsymbol{x})v_3 s \end{bmatrix} \\
&\quad + \begin{bmatrix} \frac{\partial^2}{\partial^2_{x_1}} & \frac{\partial^2}{\partial_{x_1}\partial_{x_2}} \\ \frac{\partial^2}{\partial_{x_1}\partial_{x_2}} & \frac{\partial^2}{\partial^2_{x_2}} \end{bmatrix} \psi(\boldsymbol{x}) \cdot \begin{bmatrix} v_1 \\ v_2 \end{bmatrix} \cdot (\psi(\boldsymbol{x}) - \gamma_i^3(s))]s \\
&= D\psi(\boldsymbol{x})\mathbf{v}s + \partial^2_{\boldsymbol{x}}\psi(\boldsymbol{x}) \cdot \mathbf{v}(\psi(\boldsymbol{x}) - \gamma_i^3(s))s,
\end{aligned} \tag{B.6}$$

where

$$\partial^2_{\boldsymbol{x}'} = \begin{bmatrix} \partial^2/\partial x'^2_1 & \partial^2/\partial x'_1 x'_2 \\ \partial^2/\partial x'_2 x'_1 & \partial^2/\partial x'^2_2 \end{bmatrix}. \tag{B.7}$$

Plugging this result back into (B.4) we obtain

$$\begin{aligned}
\nabla_{\boldsymbol{x}}[(\widehat{\mathbf{x} - \boldsymbol{\gamma}_i(s)}) \cdot \mathbf{v}s] &= \frac{\nabla_{\boldsymbol{x}}[(\mathbf{x} - \boldsymbol{\gamma}_i(s)) \cdot \mathbf{v}s] - D\psi(\boldsymbol{x})(\widehat{\mathbf{x} - \boldsymbol{\gamma}_i(s)})[(\mathbf{x} - \boldsymbol{\gamma}_i(s)) \cdot \mathbf{v}s]}{|\mathbf{x} - \boldsymbol{\gamma}_i(s)|^2} \\
&= \frac{D\psi(\boldsymbol{x})\mathbf{v}s + \partial^2_{\boldsymbol{x}}\psi(\boldsymbol{x}) \cdot \mathbf{v}(\psi(\boldsymbol{x}) - \gamma_i^3(s))s}{|\mathbf{x} - \boldsymbol{\gamma}_i(s)|^2} \\
&\quad - \frac{D\psi(\boldsymbol{x})(\widehat{\mathbf{x} - \boldsymbol{\gamma}_i(s)})[(\mathbf{x} - \boldsymbol{\gamma}_i(s)) \cdot \mathbf{v}s]}{|\mathbf{x} - \boldsymbol{\gamma}_i(s)|^2}.
\end{aligned} \tag{B.8}$$

We obtain the final form of the $\boldsymbol{\Xi}_{ij}$ vector after normalizing with the range, substituting in the $\mathbf{v}_i^{\perp}$, repeating the steps with the j receiver, and finally substituting $\mathbf{x}'$ for $\mathbf{x}$:

$$\begin{aligned}
\boldsymbol{\Xi}_{ij}(s, \boldsymbol{x}', \boldsymbol{v}) &= - D\psi(\boldsymbol{x}') \cdot [(\widehat{\mathbf{x}' - \boldsymbol{\gamma}_i(s)}) - (\widehat{\mathbf{x}' - \boldsymbol{\gamma}_j(s)})] \\
&\quad - \frac{D\psi(\boldsymbol{x}') \cdot \mathbf{v}_i^{\perp} s + \partial^2_{\boldsymbol{x}'}\psi(\boldsymbol{x}') \cdot \boldsymbol{v}(\psi(\boldsymbol{x}') - \boldsymbol{\gamma}_i^3(s))s}{|\mathbf{x}' - \boldsymbol{\gamma}_i(s)|} \\
&\quad + \frac{D\psi(\boldsymbol{x}') \cdot \mathbf{v}_j^{\perp} s + \partial^2_{\boldsymbol{x}'}\psi(\boldsymbol{x}') \cdot \boldsymbol{v}(\psi(\boldsymbol{x}') - \boldsymbol{\gamma}_j^3(s))s}{|\mathbf{x}' - \boldsymbol{\gamma}_j(s)|}
\end{aligned} \tag{B.9}$$

APPENDIX C
Derivation of the Position Error

We now make the following Taylor series approximations about $\epsilon = 0$ and write

$$\begin{aligned}\varphi_{ij}(\mathbf{x}' + \Delta\mathbf{x}', \mathbf{v} + \epsilon\Delta\mathbf{v}, s) \approx{}& \varphi_{ij}(\mathbf{x}', \mathbf{v}, s) \\ &+ \epsilon\partial_\epsilon\varphi_{ij}(\mathbf{x}', \mathbf{v} + \epsilon\Delta\mathbf{v}, s)|_{\epsilon=0} + \Delta\mathbf{x}' \cdot \nabla_{\boldsymbol{x}'}\varphi_{ij}(\mathbf{x}', \mathbf{v}, s),\end{aligned} \tag{C.1}$$

$$\begin{aligned}\dot\varphi_{ij}(\mathbf{x}' + \Delta\mathbf{x}', \mathbf{v} + \epsilon\Delta\mathbf{v}, s) \approx{}& \dot\varphi_{ij}(\mathbf{x}', \mathbf{v}, s) \\ &+ \epsilon\partial_\epsilon\dot\varphi_{ij}(\mathbf{x}', \mathbf{v} + \epsilon\Delta\mathbf{v}, s)|_{\epsilon=0} + \Delta\mathbf{x}' \cdot \nabla_{\boldsymbol{x}'}\dot\varphi_{ij}(\mathbf{x}', \mathbf{v}, s).\end{aligned} \tag{C.2}$$

Using equations (4.32), (4.33), (4.35), and (4.36) in (C.1) and (C.2) we have:

$$\epsilon\partial_\epsilon\varphi_{ij}(\mathbf{x}', \mathbf{v} + \epsilon\Delta\mathbf{v}, s)|_{\epsilon=0} + \Delta\mathbf{x}' \cdot \nabla_{\boldsymbol{x}'}\varphi_{ij}(\mathbf{x}', \mathbf{v}, s) = 0, \tag{C.3}$$

$$\epsilon\partial_\epsilon\dot\varphi_{ij}(\mathbf{x}', \mathbf{v} + \epsilon\Delta\mathbf{v}, s)|_{\epsilon=0} + \Delta\mathbf{x}' \cdot \nabla_{\boldsymbol{x}'}\dot\varphi_{ij}(\mathbf{x}', \mathbf{v}, s) = 0. \tag{C.4}$$

We now derive the relationship for the position and velocity errors for (C.3). The derivative with respect to ϵ can be found as

$$\begin{aligned}\partial_\epsilon\varphi_{ij}(\mathbf{x}', \mathbf{v} + \epsilon\Delta\mathbf{v}, s)|_{\epsilon=0} &= \partial_\epsilon[R_{ij}(\mathbf{x}', s) + \mathbf{L}_{ij}(\mathbf{x}', s) \cdot (\mathbf{v} + \epsilon\Delta\mathbf{v})s]|_{\epsilon=0} \\ &= \mathbf{L}_{ij}(\mathbf{x}', s) \cdot \Delta\mathbf{v}s\end{aligned} \tag{C.5}$$

where $\mathbf{L}_{ij}(\mathbf{x}', s)$ is the hitchhiker look direction component in $B_{ij}(\mathbf{x}', s)$:

$$\mathbf{L}_{ij}(\mathbf{x}', s) = [(\widehat{\mathbf{x}' - \boldsymbol{\gamma}_i(s)}) - (\widehat{\mathbf{x}' - \boldsymbol{\gamma}_j(s)})]. \tag{C.6}$$

The gradient with respect to $\boldsymbol{x}'$ is $\boldsymbol{\Xi}_{ij}(\mathbf{x}', \mathbf{v}, s)$, found in (4.16). Plugging these relationships back into (C.3), we obtain

$$\mathbf{L}_{ij}(\mathbf{x}', s) \cdot \Delta\mathbf{v}s\epsilon = -\boldsymbol{\Xi}_{ij}(\mathbf{x}', \mathbf{v}, s) \cdot \Delta\mathbf{x}'. \tag{C.7}$$

This equation describes one of the two sets of solutions for the position error. To fully understand the nature of this error, we must also solve the equation deriving the second set of conditions for the critical set of the phase, shown in (4.33).

We now derive the error relationship for (C.4). The first step is to start with the slow-time derivative of the phase $\dot{\varphi}_{ij}(\mathbf{x}', \mathbf{v}, s)$ as

$$\begin{aligned}
\dot{\varphi}_{ij}(\mathbf{x}', \mathbf{v}, s) &= \partial_s R_{ij}(\mathbf{x}', s) + \partial_s B_{ij}(\mathbf{x}', \mathbf{v}, s) \\
&= -\dot{\boldsymbol{\gamma}}_i(s) \cdot (\widehat{\mathbf{x}' - \boldsymbol{\gamma}_i(s)}) + \dot{\boldsymbol{\gamma}}_j(s) \cdot (\widehat{\mathbf{x}' - \boldsymbol{\gamma}_j(s)}) \\
&\quad + \frac{1}{|\mathbf{x}' - \boldsymbol{\gamma}_i(s)|}\big[(\mathbf{x}' - \boldsymbol{\gamma}_i(s)) \cdot \mathbf{v} - \dot{\boldsymbol{\gamma}}_i(s) \cdot \mathbf{v}s \\
&\quad - ((\widehat{\mathbf{x}' - \boldsymbol{\gamma}_i(s)}) \cdot \mathbf{v}s)(-\dot{\boldsymbol{\gamma}}_i(s) \cdot (\widehat{\mathbf{x}' - \boldsymbol{\gamma}_i(s)}))\big] \\
&\quad - \frac{1}{|\mathbf{x}' - \boldsymbol{\gamma}_j(s)|}\big[(\mathbf{x}' - \boldsymbol{\gamma}_j(s)) \cdot \mathbf{v} - \dot{\boldsymbol{\gamma}}_j(s) \cdot \mathbf{v}s \\
&\quad - ((\widehat{\mathbf{x}' - \boldsymbol{\gamma}_j(s)}) \cdot \mathbf{v}s)(-\dot{\boldsymbol{\gamma}}_j(s) \cdot (\widehat{\mathbf{x}' - \boldsymbol{\gamma}_j(s)}))\big] \\
&= (\widehat{\mathbf{x}' - \boldsymbol{\gamma}_i(s)}) \cdot (\mathbf{v} - \dot{\boldsymbol{\gamma}}_i(s)) - (\widehat{\mathbf{x}' - \boldsymbol{\gamma}_j(s)}) \cdot (\mathbf{v} - \dot{\boldsymbol{\gamma}}_j(s)) \\
&\quad + \frac{-\dot{\boldsymbol{\gamma}}_i(s) \cdot \mathbf{v}s - ((\widehat{\mathbf{x}' - \boldsymbol{\gamma}_i(s)}) \cdot \mathbf{v}s)(-\dot{\boldsymbol{\gamma}}_i(s) \cdot (\widehat{\mathbf{x}' - \boldsymbol{\gamma}_i(s)}))}{|\mathbf{x}' - \boldsymbol{\gamma}_i(s)|} \\
&\quad - \frac{-\dot{\boldsymbol{\gamma}}_j(s) \cdot \mathbf{v}s - ((\widehat{\mathbf{x}' - \boldsymbol{\gamma}_j(s)}) \cdot \mathbf{v}s)(-\dot{\boldsymbol{\gamma}}_j(s) \cdot (\widehat{\mathbf{x}' - \boldsymbol{\gamma}_j(s)}))}{|\mathbf{x}' - \boldsymbol{\gamma}_j(s)|}
\end{aligned} \tag{C.8}$$

The next step is to find the derivative with respect to ϵ, $\partial_\epsilon \dot{\varphi}_{ij}(\mathbf{x}', \mathbf{v} + \epsilon\Delta\mathbf{v}, s)$:

$$\begin{aligned}
\partial_\epsilon \dot{\varphi}_{ij}(\mathbf{x}', \mathbf{v} + \epsilon\Delta\mathbf{v}, s) &= (\widehat{\mathbf{x}' - \boldsymbol{\gamma}_i(s)}) \cdot \Delta\mathbf{v} - (\widehat{\mathbf{x}' - \boldsymbol{\gamma}_j(s)}) \cdot \Delta\mathbf{v} \\
&\quad + \frac{-\dot{\boldsymbol{\gamma}}_i(s) \cdot \Delta\mathbf{v}s - ((\widehat{\mathbf{x}' - \boldsymbol{\gamma}_i(s)}) \cdot \Delta\mathbf{v}s)(-\dot{\boldsymbol{\gamma}}_i(s) \cdot (\widehat{\mathbf{x}' - \boldsymbol{\gamma}_i(s)}))}{|\mathbf{x}' - \boldsymbol{\gamma}_i(s)|} \\
&\quad - \frac{-\dot{\boldsymbol{\gamma}}_j(s) \cdot \Delta\mathbf{v}s - ((\widehat{\mathbf{x}' - \boldsymbol{\gamma}_j(s)}) \cdot \Delta\mathbf{v}s)(-\dot{\boldsymbol{\gamma}}_j(s) \cdot (\widehat{\mathbf{x}' - \boldsymbol{\gamma}_j(s)}))}{|\mathbf{x}' - \boldsymbol{\gamma}_j(s)|}
\end{aligned} \tag{C.9}$$

and the gradient with respect to $\boldsymbol{x}'$, $\nabla_{\boldsymbol{x}'} \dot{\varphi}_{ij}(\mathbf{x}', \mathbf{v}, s)$:

$$\begin{aligned}
\nabla_{\boldsymbol{x}'} \dot{\varphi}_{ij}(\mathbf{x}', \mathbf{v}, s) &= \nabla_{\boldsymbol{x}'} \partial_s \varphi_{ij}(\mathbf{x}', \mathbf{v}, s) \\
&= \dot{\boldsymbol{\Xi}}_{ij}(\mathbf{x}', \mathbf{v}, s).
\end{aligned} \tag{C.10}$$

The relationship can now be written as

$$\epsilon\partial_{\epsilon}\dot{\varphi}_{ij}(\mathbf{x}',\mathbf{v}+\epsilon\Delta\mathbf{v},s) = -\nabla_{\boldsymbol{x}'}\dot{\varphi}_{ij}(\mathbf{x}',\mathbf{v},s)\cdot\Delta\mathbf{x}' \tag{C.11}$$

$$\begin{aligned}
-\dot{\boldsymbol{\Xi}}_{ij}(\mathbf{x}',\mathbf{v},s)\cdot\Delta\mathbf{x}' &= \mathbf{L}_{ij}(\mathbf{x}',s)\cdot\Delta\mathbf{v}\epsilon \\
&\quad + \frac{-\dot{\boldsymbol{\gamma}}_i(s)\cdot\Delta\mathbf{v}s\epsilon - ((\widehat{\mathbf{x}'-\boldsymbol{\gamma}_i(s)})\cdot\Delta\mathbf{v}s\epsilon)(-\dot{\boldsymbol{\gamma}}_i(s)\cdot(\widehat{\mathbf{x}'-\boldsymbol{\gamma}_i(s)}))}{|\mathbf{x}'-\boldsymbol{\gamma}_i(s)|} \\
&\quad - \frac{-\dot{\boldsymbol{\gamma}}_j(s)\cdot\Delta\mathbf{v}s\epsilon - ((\widehat{\mathbf{x}'-\boldsymbol{\gamma}_j(s)})\cdot\Delta\mathbf{v}s\epsilon)(-\dot{\boldsymbol{\gamma}}_j(s)\cdot(\widehat{\mathbf{x}'-\boldsymbol{\gamma}_j(s)}))}{|\mathbf{x}'-\boldsymbol{\gamma}_j(s)|} \\
&= \mathbf{L}_{ij}(\mathbf{x}',s)\cdot\Delta\mathbf{v}\epsilon - \left[\frac{\dot{\boldsymbol{\gamma}}_i^{\perp}(s)}{|\mathbf{x}'-\boldsymbol{\gamma}_i(s)|} - \frac{\dot{\boldsymbol{\gamma}}_j^{\perp}(s)}{|\mathbf{x}'-\boldsymbol{\gamma}_j(s)|}\right]\cdot\Delta\mathbf{v}s\epsilon \\
&= \mathbf{L}_{ij}(\mathbf{x}',s)\cdot\Delta\mathbf{v}\epsilon - \dot{\mathbf{L}}_{ij}(\mathbf{x}',s)\cdot\Delta\mathbf{v}s\epsilon
\end{aligned} \tag{C.12}$$

where $\mathbf{L}_{ij}(\mathbf{x}',s)$ is the hitchhiker look direction component in $B_{ij}(\mathbf{x}',s)$:

$$\mathbf{L}_{ij}(\mathbf{x}',s) = [(\widehat{\mathbf{x}'-\boldsymbol{\gamma}_i(s)}) - (\widehat{\mathbf{x}'-\boldsymbol{\gamma}_j(s)})] \tag{C.13}$$

and

$$\dot{\boldsymbol{\gamma}}_i^{\perp}(s) = \dot{\boldsymbol{\gamma}}_i(s) - (\widehat{\mathbf{x}'-\boldsymbol{\gamma}_i(s)})[\dot{\boldsymbol{\gamma}}_i(s)\cdot(\widehat{\mathbf{x}'-\boldsymbol{\gamma}_i(s)})] \tag{C.14}$$

$$\dot{\boldsymbol{\gamma}}_j^{\perp}(s) = \dot{\boldsymbol{\gamma}}_j(s) - (\widehat{\mathbf{x}'-\boldsymbol{\gamma}_j(s)})[\dot{\boldsymbol{\gamma}}_j(s)\cdot(\widehat{\mathbf{x}'-\boldsymbol{\gamma}_j(s)})]. \tag{C.15}$$